

UNIVERSIDADE FEDERAL DE ALAGOAS
CENTRO DE TECNOLOGIA
PROGRAMA DE PÓS-GRADUAÇÃO EM ENGENHARIA CIVIL

MARCELO VITOR OLIVEIRA ARAUJO

**ENERGY ANALYSIS OF THE GENERALIZED FINITE-VOLUME THEORY AND
APPLICATION TO TOPOLOGY OPTIMIZATION WITH COMPLIANCE
MINIMIZATION**

MACEIÓ

2022

MARCELO VITOR OLIVEIRA ARAUJO

**ENERGY ANALYSIS OF THE GENERALIZED FINITE-VOLUME THEORY AND
APPLICATION TO TOPOLOGY OPTIMIZATION WITH COMPLIANCE
MINIMIZATION**

Tese de Doutorado apresentada ao Programa de Pós-Graduação em Engenharia Civil da Universidade Federal de Alagoas, como requisito parcial para obtenção do título de Doutor em Engenharia Civil.

Área de concentração: *Estruturas e Materiais*.

Orientador: Prof. Dr. Márcio André Araújo
Cavalcante

Coorientador: Prof. Dr. Eduardo Nobre Lages

MACEIÓ

2022

Catálogo na fonte
Universidade Federal de Alagoas
Biblioteca Central
Divisão de Tratamento Técnico

Bibliotecária: Taciana Sousa dos Santos – CRB-4 – 2062

- A663e Araujo, Marcelo Vítor Oliveira.
Energy analysis of the generalized finite-volume theory and application to topology optimization with compliance minimization / Marcelo Vítor Oliveira Araujo. – 2022.
124 f. : il. color.
- Orientador: Márcio André Araújo Cavalcante.
Coorientador: Eduardo Nobre Lages.
Tese (Doutorado em Engenharia Civil) – Universidade Federal de Alagoas. Centro de Tecnologia. Programa de Pós-Graduação em Engenharia Civil. Maceió, 2022.
- Bibliografia: f. 115-121.
Apêndices: f. 122-124.
1. Teoria de volumes finitos. 2. Análise energética. 3. Otimização topológica. I. Título.

CDU: 624

A Deus, que foi meu grande conselheiro e amigo durante a caminhada do curso. Ele nunca me abandonou mesmo nos momentos mais difíceis.

ACKNOWLEDGMENTS

Firstly, my thanks to God, who helped me in all moments during my journey as a PhD student, He always proved to be my best adviser and friend. I'm also extremely grateful to my advisor and chair of my committee, professor Márcio, for his invaluable patience and feedback, we've come a long and hard way. I also could not have undertaken this journey without my co-advisor, professor Eduardo Nobre, who generously provided knowledge and expertise.

Thanks should also go to my PPGEC/UFAL professors for all shared knowledge during these years. I would like to extend my sincere thanks to the Federal University of Alagoas for the opportunity of taking this course and improving my personal and professional skills. I'm also thankful to CAPES and CNPq for the provided financial support.

Lastly, I would be remiss in not mentioning my family, especially my parents, Tereza and Agnaldo, for their belief in me and encouragement throughout this journey, and my sweet spouse, Monique, for all the dedicated love and emotional support. And for those who helped me directly or indirectly during this journey.

RESUMO

A teoria de volumes finitos é uma técnica numérica baseada no equilíbrio e tem apresentado sucesso em análises na mecânica dos sólidos devido a satisfação local das equações de equilíbrio e a imposição das condições de continuidade em termos médios nas faces dos subvolumes. Investigações prévias incluem a análise de convergência dos campos de deslocamentos e tensões e custo computacional, mostrando a eficiência das abordagens, especialmente no contexto de materiais heterogêneos e estruturas. Porém, essas investigações não incluíram uma análise energética, a qual é especialmente importante em problemas de minimização da flexibilidade estrutural. Como método dos elementos finitos, as técnicas numéricas baseadas em métodos de energia garantem a satisfação do balanço energético, garantindo também uma convergência monotônica para as estimativas de energia mecânica. A primeira contribuição desta tese é endereçar uma investigação numérica sobre os principais aspectos energéticos, envolvendo a teoria generalizada de volumes finitos para estruturas elásticas contínuas em análises quase estáticas para malhas estruturadas formadas por subvolumes retangulares. Os resultados obtidos são verificados por soluções analíticas e análises baseadas no método dos elementos finitos, mostrando uma convergência monotônica para as estimativas de energia com base na teoria de volumes finitos, além da satisfação do balanço energético para as versões de alta ordem da teoria quando uma malha suficientemente refinada é empregada. A otimização topológica é um método bem estabelecido para definição da melhor distribuição de material dentro de um domínio de análise. É comum se observar algumas instabilidades numéricas nas versões baseadas no método do gradiente, tais como o efeito do padrão xadrez, a dependência de malha e os mínimos locais. A formação das regiões com padrão xadrez está diretamente associada com domínios discretizados conectados por nós, usualmente observados em técnicas de otimização topológica baseadas no método dos elementos finitos. Por outro lado, a teoria de volumes finitos satisfaz as condições de continuidade entre faces comuns de subvolumes adjacentes, a qual é mais compatível do ponto de vista da mecânica do contínuo. Esta pesquisa apresenta a propriedade da teoria de volumes finitos de produzir topologias ótimas livres do efeito do padrão xadrez, a partir da performance de algoritmos de otimização topológica sem nenhuma técnica de filtragem, e empregando formulações elásticas e elastoplásticas para malhas estruturadas compostas por subvolumes retangulares. Uma formulação elastoplástica incremental da teoria padrão de volumes é empregada com o intuito de verificar como a deformação plástica pode interferir nas topologias ótimas e reduzir a concentração de tensões em determinadas regiões. Os algoritmos de otimização topológica baseados na teoria de volumes finitos são também executados utilizando um filtro para independência de malha, o qual regulariza as sensibilidades dos subvolumes, obtendo topologias ótimas que evitam a dependência de malha e problemas de tamanho de escala. A abordagem de material sólido isotrópico com penalização (SIMP – *Solid Isotropic Material with Penalization*) é empregada para evitar problemas de otimização discreta. O problema de otimização topológica proposto se mostrou eficiente, evitando instabilidades numéricas, tais como o efeito do padrão xadrez, a dependência de malha e o problema de tamanho de escala.

Palavras-chaves: otimização topológica; topologias ótimas livres do padrão xadrez; análise energética; teoria de volumes finitos; minimização da flexibilidade estrutural.

ABSTRACT

The finite-volume theory is an equilibrium-based approach and has been successfully employed in solid mechanics analysis due to the equilibrium equations' local satisfaction and the imposition of continuity conditions in a surface-averaged sense through the subvolume interfaces. Previous investigations include stress and displacement fields convergence and computational cost, showing the approach's efficiency, especially in heterogeneous materials and structures. However, those investigations did not include an energy analysis, which is especially important in compliance minimization problems. As the finite element method, energy-based approaches impose energy balance, which guarantees a monotonic energy convergence. The first idea of this contribution is to address a numerical investigation about the main mechanical energy aspects involving the generalized finite-volume theory for continuum elastic structures in quasi-static analyzes for structured meshes formed by rectangular subvolumes. The obtained results are verified with analytical and finite element-based analyzes, showing a monotonic energy convergence for the finite-volume theory and the energy balance's satisfaction for the higher-order versions when a sufficiently refined mesh is employed. Topology optimization is a well-suited method to establish the best material distribution inside an analysis domain. It is common to observe some numerical instabilities in its gradient-based version, such as the checkerboard pattern, mesh dependence, and local minima. The formation of checkerboard regions is directly associated with discretized domains connected by nodes, usually observed in topology optimization techniques based on the finite element method. On the other hand, the finite-volume theory satisfies the continuity conditions between common faces of adjacent subvolumes, which is more likely from the continuum mechanics point of view. This research demonstrates the finite-volume theory's checkerboard-free property by performing topology optimization algorithms without filtering techniques and employing elastic and elastoplastic formulations for structured meshes composed by rectangular subvolumes. An incremental elastoplastic formulation of the standard finite-volume theory is performed to verify how the plastic strain could interfere with the optimized topologies and reduce their stress concentration. The topology optimization algorithms based on the finite-volume theory are also performed using a mesh independent filter that regularizes the subvolume sensitivities, providing optimized topologies that avoid the mesh dependence and length scale issues. The solid isotropic material with penalization (SIMP) approach is employed to avoid discrete optimization problems. The proposed optimization problem has shown to be efficient, avoiding numerical instabilities, such as checkerboard pattern, mesh dependence, and length scale issues.

Keywords: topology optimization; checkerboard-free designs; energy analysis; finite-volume theory; compliance minimization.

FIGURE LIST

Figure 01 – Categories of structural optimization.....	21
Figure 02 – Checkerboard pattern effect.....	23
Figure 03 – Discretized analysis domain and local coordinate system of a generic subvolume q.....	33
Figure 04 – Surface-averaged quantities: (a) surface-averaged kinematic quantities and (b) surface-averaged static quantities.....	33
Figure 05 – Surface-averaged kinematic and static quantities for a generic subvolume q: (a) surface-averaged incremental displacements and (b) surface-averaged incremental tractions.....	40
Figure 06 – Uniaxial elastoplastic material models.....	43
Figure 07 – Geometric representation of the von Mises yield criterion.....	44
Figure 08 – Topology optimization problem domains.....	47
Figure 09 – Elements or subvolumes participating in filtering for one element or subvolume.....	50
Figure 10 – Legendre polynomials representation employed for the estimative of horizontal displacement in the subvolume vertical faces.....	56
Figure 11 – Legendre polynomials representation employed for estimative of normal tractions in the subvolume vertical faces.....	57
Figure 12 – Interpretation of the compliance minimization problem considering the linear elastic and elastoplastic behavior.....	63
Figure 13 – Flowchart of the topology optimization algorithm based on the finite-volume theory implemented in MatLab language.....	66
Figure 14 – Flowchart of the mechanical energy computation algorithm based on the finite-volume theory implemented in MatLab language.....	68
Figure 15 – Cantilever beam.....	70
Figure 16 – Convergence analysis for the cantilever beam.....	72
Figure 17 – Convergence rate analysis for the cantilever beam.....	73
Figure 18 – Rectangular beam under concentrated and uniform normal tractions.....	74
Figure 19 – Convergence analysis for the rectangular beam under concentrated loads.....	76

Figure 20 – Convergence rate analysis for the rectangular beam under concentrated loads.....	77
Figure 21 – Cantilever beam.....	78
Figure 22 – Optimized topologies for the cantilever beam analysis evaluating the compliance using the strain energy (No filtering).....	79
Figure 23 – Optimized topologies for the cantilever beam analysis with a mesh size of 202x101 (No filtering).....	80
Figure 24 – Objective function history along the optimization process for the Q4 finite-element (No filtering).....	81
Figure 25 – Objective function history along the optimization process for the Q8 finite-element (No filtering).....	82
Figure 26 – Objective function history along the optimization process for the zeroth-order finite-volume theory (No filtering).....	82
Figure 27 – Objective function history along the optimization process for the first-order finite-volume theory and compliance defined from the total strain energy (No filtering).....	83
Figure 28 – Objective function history along the optimization process for the second-order finite-volume theory and compliance defined from the total strain energy (No filtering).....	83
Figure 29 – Optimized topologies for the cantilever beam analysis evaluating the compliance using the work done by external loading (No filtering).....	85
Figure 30 – Objective function history along the optimization process for the first-order finite-volume theory and compliance defined as twice the external work (No filtering).....	85
Figure 31 – Objective function history along the optimization process for the second-order finite-volume theory and compliance defined as twice the external work (No filtering).....	86
Figure 32 – Optimized topologies for the cantilever beam analysis evaluating the compliance using the strain energy (filtering).....	87
Figure 33 – Objective function history along the optimization process for the Q4 finite-element (filtering).....	88
Figure 34 – Objective function history along the optimization process for the Q8 finite-element (filtering).....	89

Figure 35 – Objective function history along the optimization process for the zeroth-order finite-volume theory (filtering).....	89
Figure 36 – Objective function history along the optimization process for the first-order finite-volume theory (filtering).....	90
Figure 37 – Objective function history along the optimization process for the second-order finite-volume theory (filtering).....	90
Figure 38 – <i>Messerschmitt-Bölkow-Blom</i> (MBB) beam.....	92
Figure 39 – Optimized topologies for the MBB beam analysis evaluating the compliance using the strain energy (No filtering).....	92
Figure 40 – Optimized topologies for the MBB beam analysis and a mesh of 480x80 (No filtering).....	93
Figure 41 – Objective function history along the optimization process for the Q4 finite-element (No filtering).....	94
Figure 42 – Objective function history along the optimization process for the Q8 finite-element (No filtering).....	94
Figure 43 – Objective function history along the optimization process for the zeroth-order finite-volume theory (No filtering).....	95
Figure 44 – Objective function history along the optimization process for the first-order finite-volume theory and compliance defined from the total strain energy (No filtering).....	95
Figure 45 – Objective function history along the optimization process for the second-order finite-volume theory and compliance defined from the total strain energy (No filtering).....	95
Figure 46 – Optimized topologies for the MBB beam analysis evaluating the compliance using the work done by external loading (No filtering).....	97
Figure 47 – Objective function history along the optimization process for the first-order finite-volume theory and compliance defined as twice the external work (No filtering).....	98
Figure 48 – Objective function history along the optimization process for the second-order finite-volume theory and compliance defined as twice the external work (No filtering).....	98
Figure 49 – Optimized topologies for the MBB beam analysis by evaluating the compliance using the strain energy (filtering).....	99

Figure 50 – Optimized topologies for the MBB beam analysis and a mesh of 480x80 (filtering).....	99
Figure 51 – Objective function history along the optimization process for the Q4 finite-element (filtering).....	100
Figure 52 – Objective function history along the optimization process for the Q8 finite-element (filtering).....	100
Figure 53 – Objective function history along the optimization process for the zeroth-order finite-volume theory (filtering).....	101
Figure 54 – Objective function history along the optimization process for the first-order finite-volume theory (filtering).....	101
Figure 55 – Objective function history along the optimization process for the second-order finite-volume theory (filtering).....	101
Figure 56 – Penalization effect at the equivalent uniaxial stress-strain diagram...	103
Figure 57 – Sensitivity verification along the optimization process for the elastoplastic approach (No filtering).....	104
Figure 58 – Optimized topologies and relative density histograms (No filtering)..	105
Figure 59 – Objective function history along the optimization process (No filtering).....	105
Figure 60 – Von Mises stress (MPa) field for the optimized topologies (No filtering).....	106
Figure 61 – Effective plastic strain for the optimized topologies (No filtering).....	107
Figure 62 – Optimized topologies and relative density histograms (Filtering).....	107
Figure 63 – Objective function history along the optimization process (Filtering).....	108
Figure 64 – Effective plastic strain for the optimized topologies (Filtering).....	109
Figure 65 – Von Mises stress field (MPa) for the optimized topologies (Filtering).....	109
Figure 66 – Force versus displacement curves for the optimized topologies.....	110

TABLE LIST

Table 01 – Mechanical energy analysis for the cantilever beam.....	71
Table 02 – Mechanical energy analysis for the rectangular beam under concentrated loads.....	75
Table 03 – Convergence analysis for the cantilever beam evaluating the compliance using the strain energy (No filtering).....	84
Table 04 – Convergence analysis for the cantilever beam evaluating the compliance using the work done by external loading (No filtering).....	86
Table 05 – Convergence analysis for the cantilever beam evaluating the compliance using the strain energy (filtering).....	91
Table 06 – Convergence analysis for the MBB beam evaluating the compliance using the strain energy (No filtering).....	96
Table 07 – Convergence analysis for the MBB beam evaluating the compliance using the work done by external loading (No filtering).....	97
Table 08 – Convergence analysis for the MBB beam by evaluating the compliance using the strain energy (filtering).....	102
Table 09 – Performance analysis for the cantilever beam (No filtering).....	106
Table 10 – Performance analysis for the cantilever beam (Filtering).....	110

LIST OF ABBREVIATIONS

FVDAM	<i>Finite-Volume Direct Averaging Micromechanics</i>
HFGMC	<i>High-Fidelity Generalized Method of Cells</i>
DEM	<i>Discrete Element Method</i>
KKT	<i>Karush-Kuhn-Tucker</i>
MBB	Messerschmitt-Bölkow-Blom
FEM	<i>Finite Element Method</i>
MMA	<i>Method of Moving Asymptotes</i>
NDOF	Number of Degrees of Freedom
OC	<i>Optimality Criteria</i>
SIMP	<i>Solid Isotropic Material with Penalization</i>
ESO	<i>Evolutionary Structural Optimization</i>
BESO	<i>Bi-directional Evolutionary Structural Optimization</i>
VOF	<i>Volume Of Fluid</i>
FVT	<i>Finite-Volume Theory</i>
FVT ^{0th}	<i>Zeroth-Order Finite-Volume Theory</i>
FVT ^{1st}	<i>First-Order Version of the Generalized Finite-Volume Theory</i>
FVT ^{2nd}	<i>Second-Order Version of the Generalized Finite-Volume Theory</i>

SYMBOLS LIST

CHAPTER 2

β	Horizontal position of a generic subvolume
γ	Vertical position of a generic subvolume
N_β	Number of horizontal subvolumes
N_γ	Number of vertical subvolumes
L	Horizontal dimension of the discretized structure
H	Vertical dimension of the discretized structure
l_q	Subvolume horizontal dimension
h_q	Subvolume vertical dimension
q	Subvolume index
N_q	Total number of subvolumes
$W_{i(mn)}^{(q)}$	Unknown coefficients of the displacement field
$x_i^{(q)}$	Local components of the position vector
x_i	Global components of the position vector
$u_i^{(q)}$	Components of the displacement field
$\bar{u}_i^{(p)}$	Surface-averaged displacements components in the face p
$\theta_{ij}^{(p)}$	Surface-averaged rotations components in the face p
$\kappa_{ij}^{(p)}$	Surface-averaged curvature components in the face p
$\bar{\mathbf{u}}^{(q)}$	Local surface-averaged displacement vector
$\bar{\boldsymbol{\theta}}^{(q)}$	Local surface-averaged rotation vector
$\bar{\boldsymbol{\kappa}}^{(q)}$	Local surface-averaged curvature vector
$\mathbf{W}^{(q)}$	Vector containing the unknown coefficients related to the zeroth-order finite-volume theory
$\mathbf{W}_{\nabla}^{(q)}$	Vector containing the unknown coefficients related to the first-order finite-volume theory
$\mathbf{W}_{\nabla^2}^{(q)}$	Vector containing the unknown coefficients related exclusively to the second-order finite-volume theory
$\mathbf{W}_{(00)}^{(q)}$	Vector containing the zeroth-order unknown coefficients
$\bar{t}_i^{(p)}$	Surface-averaged traction components acting in the face p

$\bar{t}_{i/j}^{(p)}$	Surface-averaged first derivative components of normal tractions acting in the face p
$\bar{t}_{i/jj}^{(p)}$	Surface-averaged second derivative components of normal tractions acting in the face p
$\bar{\mathbf{t}}^{(q)}$	Local surface-averaged traction vector
$\bar{\mathbf{t}}_{\nabla}^{(q)}$	Local surface-averaged normal traction first derivative vector
$\bar{\mathbf{t}}_{\nabla^2}^{(q)}$	Local surface-averaged normal traction second derivative vector
$L_p^{(q)}$	Subvolume edges lengths
$\mathbf{K}_{(16 \times 16)}^{(q)}$	Local stiffness matrix
$ndof$	Number of degrees of freedom
$\mathbf{U}_{(ndof \times 1)}$	Global surface-averaged kinematic vector
$\mathbf{T}_{(ndof \times 1)}$	Global surface-averaged static vector
$\mathbf{L}_{(16 \times ndof)}^{(q)}$	Kinematic and static incidence matrix
$\mathbf{K}_{(ndof \times ndof)}$	Global stiffness matrix
$\Delta \mathbf{u}_i^{(q)}$	Incomplete quadratic incremental displacement field components
$\Delta \bar{\mathbf{u}}_i^{(q,p)}$	Surface-averaged incremental displacement components
$\Delta \bar{\mathbf{u}}^{(q)}$	Surface-averaged incremental displacement vector
$\Delta \mathbf{W}^{(q)}$	Vector containing the first and second-order unknown coefficients for the elastoplastic formulation
$\Delta \mathbf{W}_{(00)}^{(q)}$	Vector containing the zeroth-order unknown coefficients for the elastoplastic formulation
$\Delta \bar{\mathbf{t}}_i^{(q,p)}$	Components of surface-averaged incremental traction vector
$\Delta \bar{\mathbf{t}}^{(q)}$	Surface-averaged incremental traction vector
$\Delta \mathbf{T}_{(ndof \times 1)}$	Incremental surface-averaged global traction vector
$\Delta \mathbf{U}_{(ndof \times 1)}$	Incremental surface-averaged global displacement vector
$\sigma_y(\varepsilon_p)$	Yield stress
σ_{y0}	Initial yield stress
H	Hardening coefficient of the material
$\sigma_1, \sigma_2, \sigma_3$	Principal stresses
$f(\sigma_1, \sigma_2, \sigma_3, \varepsilon_p)$	Multi-axial von Mises yield function

$\sigma_{vm}(\sigma_1, \sigma_2, \sigma_3)$	Equivalent von Mises stress
$\mathbf{C}^{(q)}$	Exact tangent material stiffness matrix
\mathbf{I}	Identity matrix
$\mathbf{C}_{el}^{(q)}$	Elastic stiffness matrix
$\Delta\boldsymbol{\sigma}^{(q)}$	Stress increment vector
$\Delta\boldsymbol{\varepsilon}^{(q)}$	Strain increment vector
$\Delta\boldsymbol{\varepsilon}_{el}^{(q)}$	Elastic strain increment vector
$\Delta\boldsymbol{\varepsilon}_p^{(q)}$	Plastic strain increment vector

CHAPTER 3

ρ	Relative density function
Ω_d	Optimized structure subdomain
Ω	Reference domain
\bar{V}	Limit volume for the optimized structure
$E(\rho)$	Young modulus at density ρ
E_0	Young modulus of the solid material
p	Penalty factor
N	Total number of elements of the discretized structure
V	Material volume
ρ_e	Element relative density
\mathbf{d}_e	Local displacement vector
\mathbf{K}_e^0	Local stiffness matrix for a unitary relative density
$\boldsymbol{\rho}$	Relative density vector
f	Prescribed volume fraction
ρ_{min}	Minimum relative density
η_c	Weight material function
V	Volume structure
V_e	Subvolume volume
c_q	Volume fraction of subvolume q
B_e	Auxiliar variable
η	Damping factor
k	Iteration

m	Move-limit
$\frac{\partial c}{\partial \rho_q}$	Objective function sensitivity for the compliance minimization topology optimization problem
λ	Lagrangian multiplier
\hat{H}_f	Convolution operator
R	Filter radius

CHAPTER 4

U	Total strain energy
\bar{U}	Specific strain energy
σ_{ij}	Stress tensor components
ε_{ij}	Strain tensor components
C_{ijkl}	Stiffness tensor components
W	External work
S_u	External surface with predicted displacements
S_σ	External surface subjected to external loading
ω_{ij}	Asymmetric rotation tensor
σ	Stress tensor
ε	Strain tensor
C	Stiffness tensor
d	Global nodal displacement vector
K	Global stiffness matrix
F	Global nodal force vector
B	Strain displacement matrix
u	Displacement vector
t	Surface stress vector
N	Shape functions matrix
$\varepsilon^{(q)}$	Local strain tensor
$E_m^{(q)}$	Kinematic matrices
$U^{(q)}$	Local strain energy
$u_1^{(q)}$	Horizontal displacement in a vertical subvolume face
$\theta_{12}^{(q)}$	Counterclockwise rotation in a vertical subvolume face

$\kappa_{12}^{(q)}$	Counterclockwise curvature in a vertical subvolume face
$\mu_{1(m)}^{(q)}$	Unknown coefficients of the horizontal displacement on a vertical face
$t_1^{(q)}$	Normal traction acting on a vertical subvolume face
$t_{1/2}^{(q)}$	First normal traction derivative
$t_{1/22}^{(q)}$	Second normal traction derivative
$\tau_{1(m)}^{(q)}$	Unknown coefficients associated with the normal tractions acting on the subvolume vertical face
$R_i^{(q)}$	Resultant force along the x_i direction acting on a subvolume vertical face
$M_R^{(q)}$	Resultant bending moment acting on a subvolume vertical face
$S_R^{(q)}$	Second-order bending moment acting on a subvolume vertical face
$\tilde{W}^{(q)}$	Work done in a subvolume vertical face
$\mathbf{R}^{(q)}$	Local resultant force vector
$\mathbf{M}_R^{(q)}$	Local resultant bending moment vector
$\mathbf{S}_R^{(q)}$	local resultant second-order bending moment vector
$W^{(q)}$	Work done in a subvolume q
$\hat{\mathbf{K}}^{(q)}$	Modified local stiffness matrix
\mathbf{R}	Global resultant force vector
\mathbf{M}_R	Global resultant bending moment vector
\mathbf{S}_R	Global resultant second-order bending moment vector
$\hat{\mathbf{K}}$	Modified global stiffness matrix
$C(\boldsymbol{\rho})$	Compliance function
$\frac{\partial C(\boldsymbol{\rho})}{\partial \rho_r}$	Compliance function gradient
$\hat{\mathbf{K}}^{(r)}(1)$	Modified local stiffness matrix considering a unitary relative density
p	Penalty factor
$W^{(r)}$	External work done in the subvolume r
$U^{(r)}$	Strain energy in the subvolume r
H_p	Hardening parameter
θ_2	Mean slope of the plastic region
$\hat{\mathbf{K}}_k^{(q)}$	Modified local tangent stiffness matrix

$\widehat{\mathbf{K}}_k$	Modified global tangent stiffness matrix
$\Delta \mathbf{R}_k^{(q)}$	Incremental local resultant force vector
$\Delta \mathbf{R}_k$	Incremental global resultant force vector

CHAPTER 6

h	Beam height
l	Beam length
P	Applied load intensity
E	Young modulus
ν	Poisson's ratio
Error	Relative error estimative
$U W_{numerical}$	Total strain energy or external work done for the numerical analysis
$U_{analytical}$	Total strain energy obtained for the analytical solution
Δp	Penalty factor increments for the employed continued penalization scheme
σ_y	Yield stress

SUMMARY

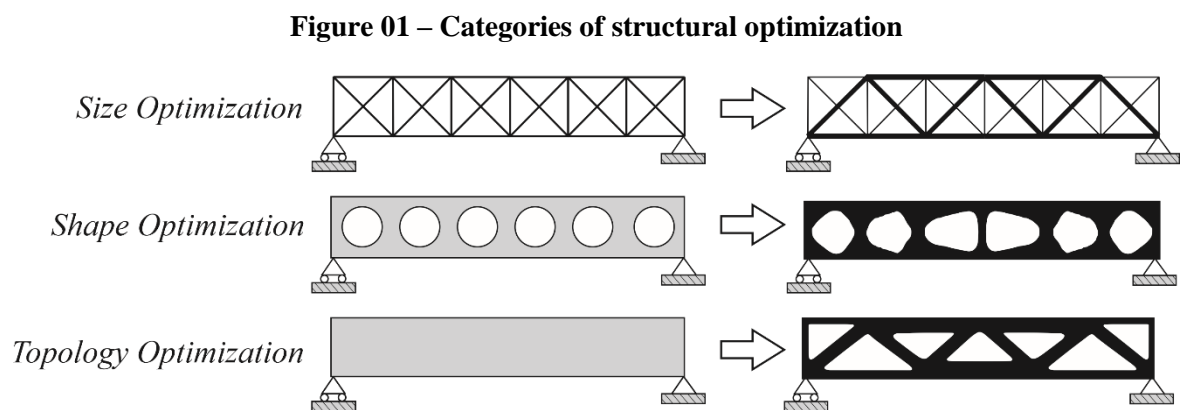
1 INTRODUCTION.....	21
1.1 Motivation.....	25
1.2 Objectives.....	28
<i>1.2.1 General objective.....</i>	<i>28</i>
<i>1.2.2 Specific objectives.....</i>	<i>28</i>
1.3 Dissertation Structure.....	28
2 GENERALIZED FINITE-VOLUME THEORY.....	30
2.1 Theoretical Framework.....	32
2.2 Finite-Volume Theory for Elastoplastic Analysis.....	38
<i>2.2.1 Incremental formulation of the finite-volume theory for elastoplastic analysis.....</i>	<i>39</i>
<i>2.2.2 Local tangent stiffness matrix.....</i>	<i>39</i>
<i>2.2.3 Global tangent stiffness matrix assemblage.....</i>	<i>42</i>
<i>2.2.4 Tangent material stiffness matrix.....</i>	<i>42</i>
3 TOPOLOGY OPTIMIZATION PROBLEMS.....	47
3.1 Material Model.....	47
3.2 Compliance Minimization Problem.....	48
3.3 OC Method.....	49
3.4 Mesh-Independency Filter.....	50
4 COMPLIANCE ESTIMATION FOR THE GENERALIZED FINITE-VOLUME THEORY.....	52
4.1 Strain Energy Evaluation by the Generalized Finite-Volume Theory.....	54
4.2 External Work Evaluation by the Generalized Finite-Volume Theory.....	55
4.3 Sensitivity Analysis for the Compliance Function by the Generalized Finite-Volume Theory.....	59
4.4 Compliance Function and Sensitivity for Elastoplastic Analysis based on the Standard Finite-Volume Theory.....	62
5 NUMERICAL IMPLEMENTATIONS.....	65
5.1 Topology Optimization Algorithm.....	65
5.2 Energy Computation Algorithm for the Finite-Volume Theory.....	67
6 RESULTS AND DISCUSSIONS.....	69
6.1 Energy Evaluation for the Generalized Finite-Volume Theory.....	69

6.1.1 Example 1: Cantilever beam.....	69
6.1.2 Example 2: Rectangular beam subjected to concentrated loads.....	73
6.2 Compliance Minimization Problem based on the Generalized Finite-Volume Theory for Elastic Analysis.....	77
6.2.1 Example 1: Cantilever beam.....	78
6.2.2 Example 2: Messerschmitt-Bölkow-Blom (MBB) beam.....	91
6.3 Compliance Minimization Problem based on the Standard Finite-Volume Theory for Elastoplastic Analysis.....	102
CONCLUSIONS.....	111
Further Works.....	113
REFERENCES.....	115
APPENDIX A.....	122
APPENDIX B.....	123

1 INTRODUCTION

In structural design, engineers want to find the best project that attends all the design restrictions and optimizes structural performance. Traditionally, the best project is accomplished based on the engineer experience, causing dependence on their work. Therefore, structural optimization techniques have been developed to help engineers find the optimal configuration for structural designs, without the need to base their designs on past experiences. In general, structural optimization problems can be divided into two main categories: material optimization and material distribution optimization. The first category intends to establish the best material properties to a design, while the second look up to find the best material distribution inside an analysis domain.

The material distribution-based optimization problems include sizing optimization, which quests to find the optimal size in terms of length, thickness, and highness (LARSSON, 2016); shape optimization, which introduces shape changes on the design to find the optimal solution (JOHNSEN, 2013); and topology optimization, which seeks to find the best material distribution inside the analysis domain for the given objective function and constraints (ELELWI et al., 2021). The structural topology optimization is one of the most important structural optimization problems, becoming one of the fastest-growing research fields in the structural analysis due to its applications in different areas, such as solid mechanics, physics, multi-material modeling, and computer sciences. Figure 1 illustrates optimized structures obtained by each structural optimization approach.



Font: Adapted from Bendsøe and Sigmund (2003).

The topology optimization problem was proposed initially by Michell (1904), who derived the Optimality Criteria (OC) method for the least weight layout of trusses. This method is typically used for compliance minimization or stiffness maximization problems,

usually combined with the so-called SIMP (*Solid Isotropic Material with Penalization*) approach (COLLET et al., 2017). In this case, the material properties are taken as constants inside each element of the discretized analysis domain, and the design variables are the element relative densities.

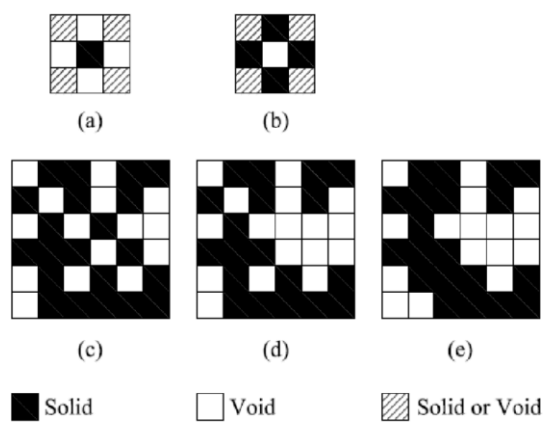
In a topology optimization problem, the interest is in defining which points of the analysis domain should be material or void, generating a “black and white” design. Therefore, the structural material distribution is obtained by a binary “0-1”, where 0 indicates void and 1 indicates the presence of material (BENDSØE; SIGMUND, 2003). This kind of topology optimization leads to an integer programming problem, which has shown to be an unfeasible approach. However, the material distribution can be also defined in terms of a continuum function, which defines the material relative density and can assume any real value between approximately 0, indicating void, and 1, indicating solid. In this case, the intermediate values of relative density must be avoided by penalization techniques (PARÍS et al., 2009).

An alternative and popular technique to solve this problem is the “power-law approach” or SIMP approach, which penalizes the intermediate values of relative densities to obtain a “black and white” project. In this approach, the interest is in determining the best solid isotropic material distribution on the analysis domain (BENDSØE; SIGMUND, 2003). Therefore, the material properties are modeled by the relative material density raised to a given power to penalize the intermediate values. In topology optimization, the SIMP method has been extensively used due to its versatility, convergence, and ease implementation (ROZVANY, 2009). Other possible topology optimization methods include the ESO (*Evolutionary Structural Optimization*) method, where the optimized structure is sought by removing the inefficient elements on the design domain in every iteration step; BESO (*Bi-directional Evolutionary Structural Optimization*) method, where the material is added in the vicinity of overstressed elements, and material is removed in inefficient areas; and level set methods, which consider level set functions to parameterize the design domain indicating solid for values greater than a specific constant and void for values below this constant (YÜKSEL, 2019).

Topology optimization has raised as a powerful technique for structural design, although there are some problems related to numerical issues. The different types of numerical instabilities are well summarized by Sigmund and Petersson (1998) and can be divided into three main categories: checkerboard pattern effect, which refers to the formation of regions alternating solid and void elements in a checkerboard shape; mesh dependence,

which refers to the problem of not having qualitatively the same solution for different discretizations; and local minima, which refers to the problem of having different solutions for the same discretizations when different input parameters are employed. Unless the analysis desires to recover the Michell-type structure, it is undesirable to have any of these instabilities in the optimal solution, especially the mesh-dependence issue, once the analytical solution for topology optimization problems initially proposed by Michell (1904) have infinite bars, being characterized as a mesh-dependent solution.

Figure 02 – Checkerboard pattern effect



Font: Rouhi and Rohani (2008).

According to Díaz and Sigmund (1995), the appearance of checkerboard regions in optimized topologies occurs due to the numerical assumptions from the finite element method, leading the optimized structure to present some sort of artificial stiffness. The checkerboard pattern problem is characterized by the emergence of a set of regions connected by pins or corner nodes, as illustrated in Figure 2(a, b, c, d), directly related to the physical modeling promoted by the topology design technique. According to Jog and Haber (1996), these regions appear when unstable finite elements are employed in the topology optimization analysis, where this instability is caused by the combination of the density and displacement fields. Thus, Jog et al. (1994) and Jog and Haber (1996) have discussed that certain combinations of density and displacement interpolation functions generate checkerboard-free designs, where these combinations promote finite-element strategies that are stable and more indicated for topology design problems. A desirable solution would be to change the finite-element unstable strategies by numerical techniques that guarantee that the regions are connected by edges instead of nodes, as the finite-volume theory initially proposed by Bansal and Pindera (2003).

Possible solutions for the checkerboard-problem include the adoption of higher-order finite elements (DÍAZ; SIGMUND, 1995; JOG; HABER, 1996), filtering techniques based on image processing (SIGMUND; PETERSSON, 1998; SWAN; KOSAKA, 1997; SIGMUND, 2007), additional constraints based on perimeter or gravity control (HABER et al., 1996; FUJII; KIKUCHI, 2000), and the employment of modified or polygonal finite elements (RAHMATALLA; SWAN, 2004; BALOGH; LÓGÓ, 2017; PAULINO; LE, 2009; TALISCHI et al., 2010 and 2012; ROZVANY et al., 2003). Other possible solutions would be the employment of corner contact function (POMEZANSKI et al., 2005), hierarchical neighboring search scheme (SVANBERG; WERME, 2005), additional constraint to prevent corner contacts (POULSEN, 2002), design variables defined by description or VOF (*volume of fluid*) functions (RUITER; KEULEN, 2004; ABE; KORO, 2006), nodal design variables and projection schemes (GUEST et al., 2004), or diffusion techniques and phase-field methods (WANG et al., 2004).

In this case, to circumvent problems related to mesh dependence and local minima, more specifically, a sensitivity filter and continued penalization scheme can be respectively employed. In the image filter, elements sensitivities depend on the weight average of their neighboring elements. This procedure can also help to solve the mesh dependence problem, as suggested by Sigmund and Petersson (1998). The mesh dependence problem is also related to the local minima issue since the change in the mesh size (an initialization parameter) produces qualitatively different responses to the same optimization problem.

Since the pioneering work of Bendsøe and Kikuchi (1988) in the homogenization method, the finite element-based strategy for structural topology optimization has received full attention and experienced considerable progress (WANG; WANG, 2006). Therefore, the advantages and disadvantages are well-known. An alternative technique to the finite element method is the finite-volume theory, which employs the volume-average of the different fields that define the material behavior and imposes the boundary and continuity conditions in an averaged sense. This technique has shown to be a well suitable method for elastic stress analysis in solid mechanics, investigations of its numerical efficiency can be found in Cavalcante et al. (2007a, b and 2008) and Cavalcante and Pindera (2012a, b). The satisfaction of equilibrium equations at the subvolume level, concomitant to kinematic and static continuities established in a surface-averaged sense between common faces of adjacent subvolumes, are features that distinguish the finite-volume theory from the finite element method.

The checkerboard instability mentioned later is related to the finite element method's assumptions, such as the satisfaction of equilibrium and continuity conditions at the element nodes. Also, the equilibrium equations are not satisfied at the element level, only when a sufficiently refined mesh is employed. Differently, the finite-volume theory satisfies the equilibrium equations at the subvolume level, and the compatibility conditions are established through the subvolume interfaces. Thus, in the finite-volume theory, the connections between adjacent subvolumes occur through subvolumes' faces, which is more likely from the continuum mechanics point of view. In the finite element method, the connections between neighboring elements occur through the nodes, leading to optimized topologies with checkerboard regions in the absence of regularization techniques for triangular or quadrilateral elements.

This contribution addresses different topology optimization approaches of continuum elastic and elastoplastic structures based on the finite-volume theory for structured meshes formed by rectangular subvolumes, showing that the checkerboard pattern is a problem related to the conventional finite element analysis once these undesirable topologies emerge from the physical modeling proposed by a finite-element based strategy, which is characterized by the formation of sets of regions connected by nodes. Thus, this numerical instability tends to disappear when this method is substituted by a numerical technique that promotes connections by faces. The compliance minimization problem subjected to a volume constraint is evaluated in this research. For this problem, two different ways to evaluate the objective function in the context of the higher-order versions of the finite-volume theory are investigated as an essential guidance for this technique's employment. Comparison results between the different approaches are provided, demonstrating the new topology optimization techniques' efficiency based on the finite-volume theory, with competitive processing time, even when the higher-order versions of the theory are employed. The compliance function and its sensitivity formulation are also presented for the performed elastoplastic approach, providing topology optimization algorithms that increase the computational cost and decrease the level of stress concentration in the obtained optimized topology.

1.1 Motivation

In the last three decades, the finite element method has been widely employed for structural analysis in topology optimization problems. However, this numerical technique when employed in topology optimization problems provides optimized topologies with

inconsistencies, related to some numerical issues, more likely the checkerboard pattern. Since the finite-element method is a variational technique that satisfies the equilibrium and continuity conditions at the nodes, it is commonly observed the generation of checkerboard regions in the optimized topologies when this technique is employed. Here, it is suggested the employment of a numerical technique that establishes connections through edges between neighboring elements, as the finite-volume methods. This feature was also explored by other approaches in the literature to solve checkerboard pattern problem, as seen in Paulino and Le (2009), Talischi et al. (2009), Talischi et al. (2010 e 2012), Londoño and Paulino (2021), and Rahmatalla and Swan (2004).

As the compliance minimization problem plays a big role in topology optimization, in this contribution, the compliance problem is implemented based on the finite-volume theory. According to the conservative work-energy principle, the work done by external loads is equal to the total strain energy. The term total strain energy is referenced to the strain energy evaluated in the entire domain of analysis. This principle is observed mainly in energy-based numerical approaches, like the finite element method. However, when an equilibrium-based approach is employed, a residual difference between work done by external loading and total strain energy can be observed for not sufficiently refined meshes. Therefore, an energetic evaluation of the finite-volume theory is performed to verify for what versions of the finite-volume theory the equivalence between work done and strain energy is required.

This contribution also addresses numerical approaches to compute the total strain energy and the work done by external loading of continuum elastic structures based on the generalized finite-volume theory. Comparing results with a traditional energy-based numerical technique (finite element method) is performed to investigate the proposed approaches' efficiency. The obtained results are also compared with analytical solutions, showing a monotonic energy convergence with mesh refinement for the three versions of the finite-volume theory and the energy balance satisfaction for the higher-order versions when a sufficiently refined mesh is employed. Additionally, these obtained energy functions are explored in obtaining optimized topologies employing the finite-volume theory strategy for compliance minimization. Based on these investigations, it is proposed a topology optimization technique applying the finite-volume theory for compliance minimization problems based on the elastic and elastoplastic formulations.

Araujo (2018) has obtained preliminary results for optimized topologies based on the generalized finite-volume theory for compliance minimization problems, where the

compliance function is defined as twice the work done by external loads in the absence of filtering techniques. However, it has not performed any sensitivity analysis considering the different assumptions of the finite-volume theory. In addition, the results were obtained for coarse meshes considering a continued penalization scheme, where the penalty factor has assumed the values of 1, 2, and 3 along the topology optimization process. This contribution evaluates compliance by considering the different mechanical energy aspects of the generalized finite-volume theory, including the total strain energy estimations. A difference between work done by external loads and total strain energy is observed for the first and second-order versions of the finite-volume theory when not sufficiently fine mesh is employed. In addition, before this contribution, an energy analysis based on a study of the energy balance was never performed for the generalized finite-volume theory.

In this contribution, the continued penalization scheme is adjusted using increments of 0.5 and increasing gradually from 1 to 4 to minimize possible local minimum issues for the performed elastic analysis. In contrast, increments of 0.25 are employed for the elastoplastic approaches. Additionally, this contribution implements and verifies sensitivity analyses of the adopted objective functions taking advantage of finite-volume theory assumptions. The employed meshes have been refined compared to Araujo (2018), and the damping factor is adjusted to avoid divergence during the optimization process. Also, this is the first contribution to present results employing a mesh-independent filter in topology optimization using the finite-volume theory, which regularizes the oscillation in the displacement field that occurs in the low-density regions and provides mesh-independent optimized topologies.

An energy analysis of continuum elastic structures is performed based on the generalized finite-volume theory by presenting the different aspects that involve the mechanical energy estimation in the context of rectangular subvolumes. Cavalcante and Pindera (2012a,b) have performed different analyzes for the generalized finite-volume theory based on the quality of the displacement and stress fields, kinematic and static compatibilities, and convergence to analytical solutions. However, an analysis of convergence based on mechanical energy aspects, checking the equivalence between total strain energy and external work done in a structure, was never performed, which is also a contribution of this dissertation. These formulations could also be employed to obtain checkerboard-free and mesh-independent optimized topologies; additionally, they can reduce the structure perimeter compared to the same approaches based on the finite element method, which is a desired feature for printing or manufacturing purposes.

1.2 Objectives

1.2.1 General objective

To propose topology optimization approaches for compliance minimization problems based on the generalized finite-volume theory employing elastic and elastoplastic formulations.

1.2.2 Specific objectives

- To define a compliance function for the generalized finite-volume theory, considering the work done by external loading.
- To define a compliance function for the generalized finite-volume theory, considering the total strain energy.
- To verify the equivalence between external work and strain energy in the generalized finite-volume theory.
- To implement topology optimization algorithms based on the generalized finite-volume theory.
- To implement topology optimization algorithms based on an incremental elastoplastic formulation for the standard finite-volume theory.
- To obtain optimized topologies based on the different versions of the generalized finite-volume theory.
- To obtain optimized topologies based on the elastoplastic formulation of the standard finite-volume theory.
- To defined what strategy should be used for the estimation of the structural compliance.
- To obtain optimized topologies by employing a mesh-independency filter.

1.3 Dissertation Structure

This dissertation is composed by six chapters, where this one is dedicated for introduction, motivation, objectives, and dissertation structure. In chapter 2, it is presented the general concepts about the generalized finite-volume theory, including the elastoplastic formulation for the standard finite-volume theory. In chapter 3, it is presented the employed topology optimization problem, including the OC method and the mesh-independent filter. In chapter 4, it is defined two different ways to estimate the compliance function for the

generalized finite-volume theory and for the elastoplastic formulation of the standard finite-volume theory. In chapter 5, it is presented the numerical implementations using the MatLab language for mechanical energy computation and topology optimization for compliance minimization based on the generalized finite-volume theory. In chapter 6, the obtained results are presented, considering the energetic balance of the different versions of the generalized finite-volume theory, and the topology optimization algorithms for the new approaches.

2 GENERALIZED FINITE-VOLUME THEORY

In fluid mechanics analysis, the finite-volume method is a well-established technique for boundary-value problems governed by parabolic and hyperbolic equations (VERSTEEG; MALALASEKERA, 2007). The finite-volume method's simplicity and stability have motivated its implementation in solid mechanics' problems as an alternative approach to the finite element method. The formulation of this method in solid mechanics is characterized by differences in the subvolume displacement representation and domain discretization, in addition to the local satisfaction of differential equilibrium equations (CAVALCANTE; PINDERA, 2012a, b). Starting with the work of Demirdžić et al. (1988), Fryer et al. (1991), Demirdžić and Martinović (1993), Demirdžić and Muzaferija (1994), Bailey and Cross (1995), Taylor et al. (1995), and Wheel (1996), the applications to solid mechanics problems and further development of this technique continue. Cardiff and Demirdžić (2021) have recently presented the most relevant contributions to the finite-volume method in solid mechanics in the last three decades.

Unlike the former versions of the finite-volume method, the finite-volume theory has its origins in the so-called higher-order theory for functionally graded materials, developed in a sequence of papers in the 1990s, and summarized in Aboudi et al. (1999). Bansal and Pindera (2003 and 2005) and Zhong et al. (2004) firstly suggested a reconstruction of this theory. They have simplified the design domain discretization and implemented an efficient local/global stiffness matrix approach. Therefore, this reconstruction has revealed the new higher-order approach as, in fact, a finite-volume method, motivating the nomenclature changing to reflect the aspects of the reconstructed theory fundamentally. After that, Cavalcante et al. (2007a, b) introduced a parametric mapping in the elasticity-based version of the finite-volume theory, enabling the modeling of curved structures. Following Cavalcante et al. (2007a, b), Gattu et al. (2008) and Khatam and Pindera (2009 and 2010) suggested a parametric mapping of the homogenized version of the finite-volume theory, known as FVDAM (Finite-Volume Direct Averaging Micromechanics).

Haj-Ali and Aboudi (2012) advocate preserving the original name of the High-Fidelity Generalized Method of Cells (HFGMC), claiming to exist only computational implementation differences in the Finite-Volume Direct Averaging Micromechanics (FVDAM) theory for solving the governing equations for both orthogonal and parametric geometries of the subvolumes of the discretized domain of analysis. Cavalcante et al. (2012) critically compare the Parametric Finite-Volume Micromechanics with the High-Fidelity Generalized Method of

Cells with arbitrary cell geometry proposed by Haj-Ali and Aboudi (2010), showing that the extension proposed by Haj-Ali and Aboudi (2010) follows the framework of the parametric FVDAM theory, and not the original HFGMC model as claimed. Also, Cavalcante et al. (2012) demonstrate that the HFGMC with arbitrary cell geometry violates accepted principles that every mechanics theory must satisfy, namely correct reducibility and coordinate frame indifference. Direct comparison of predictions generated by the parametric FVDAM theory, the HFGMC with arbitrary cell geometry, and finite-element method demonstrates no need for the extension carried out in the specific manner proposed by Haj-Ali and Aboudi (2010), which produces inferior results (CAVALCANTE et al., 2012).

The second-order displacement field representation inside the subvolumes and the enforcement of tractions and displacements in a surface-averaged sense leads to interpenetrations between common faces of adjacent subvolumes (CAVALCANTE; PINDER, 2012a). As a result, Cavalcante and Pinder (2012a) suggested a generalization of the finite-volume theory, based on a higher-order displacement field representation. They have introduced new surface-averaged kinematic and static variables, inspired on the linear elasticity theory assumptions, preserving the finite-volume framework, as the local satisfaction of equilibrium equations and the establishment of continuity conditions in a surface-averaged sense. Thus, the additional coefficients of the displacement field can be expressed in terms of the new surface-averaged kinematic variables, which enforces continuity across adjacent subvolumes, avoiding undesirable interfacial interpenetrations.

The generalization proposed by Cavalcante and Pinder (2012a, b) is applicable for rectangular analysis domains discretized in rectangular subvolumes. This generalization is accomplished by adding systematically different orders to the zeroth-order (standard) finite-volume theory, which corresponds to the original version presented by Bansal and Pinder (2003). Each order corresponds to an increase in the displacement field complexity, followed by the addition of kinematic quantities evaluated in an average sense at the subvolume faces. Thus, the first order finite-volume theory incorporates rotations to the original version, while the second-order finite-volume theory includes rotations and curvatures. Cavalcante and Pinder (2014a, b) proposed a generalization of the homogenized version of the finite-volume theory for periodic materials under finite deformations.

Recently, Chen et al. (2018) proposed a three-dimensional parametric formulation of the FVDAM theory for multiphase heterogeneous materials with periodic microstructure. Similarly, Vieira and Marques (2019) have proposed a parametric three-dimensional

extension of the finite-volume theory to evaluate the thermal conductivity of periodic multiphase composites. Summarily, the finite-volume theory is quite a new numerical approach, mainly employed for heterogeneous materials with periodic microstructures, which is an excellent solution for the checkerboard pattern issue usually presented in topology optimization for compliance minimization based on the finite element method.

Different versions of the finite-volume method can be found in the literature, as the cell-centered and vertex-centered approaches (CAVALCANTE; PINDERA, 2012a). They can share similar features with the finite-volume theory, as the satisfaction of the equilibrium equations locally, and the continuity conditions imposed through the faces, as expected from a continuum mechanics point of view. These features can also be found in the Discrete Element Method (DEM) for continuous medium. See, for example, one of the most recent applications of the DEM approach to the multi-scale modeling of heterogeneous materials with periodic microstructure presented by Ferretti (2020). These approaches can also be explored to solve the checkerboard pattern of topology optimization.

2.1 Theoretical Framework

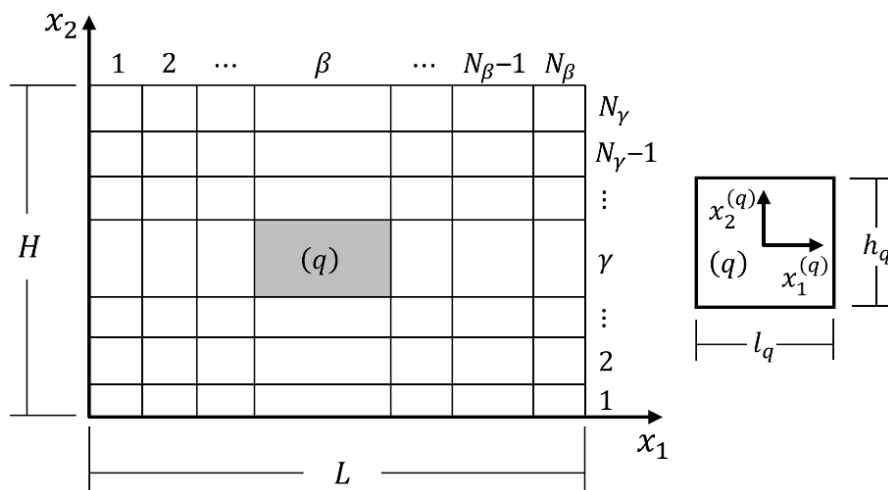
The presented formulation has its roots in the second-order version of the generalized finite-volume theory presented in Cavalcante and Pindera (2012a) for structured meshes composed by rectangular subvolumes. This technique approximates the displacement field by second-order Legendre polynomials expressed as a function of the local coordinates inside each subvolume (CAVALCANTE et al., 2007a). Besides, the boundary and continuity conditions are imposed in a surface-averaged sense, and the equilibrium equations are satisfied at the subvolume level.

Figure 3 shows a rectangular structure subdivided in $N_q = N_\beta N_\gamma$ rectangular subdomains called subvolumes. N_β and N_γ indicate the number of subdivisions corresponding to the intervals $0 \leq x_1 \leq L$ and $0 \leq x_2 \leq H$, respectively. Each subvolume can be denoted by a single index q ($1 \leq q \leq N_q$) or by a pair of indexes $\beta = 1, \dots, N_\beta$ and $\gamma = 1, \dots, N_\gamma$, where q can be evaluated from β and γ . The subvolume (β, γ) occupies the position β in the horizontal direction and the position γ in the vertical direction, or $q = \gamma + (\beta - 1)N_\gamma$ for the discretized structure. In this formulation of the generalized finite-volume theory, the components of the displacement field in the subvolumes can be approximated by the Legendre polynomial expansion in the local coordinate system, shown in Figure 3 (CAVALCANTE; PINDERA, 2012a):

$$\begin{aligned}
u_i^{(q)} = & W_{i(00)}^{(q)} + x_1^{(q)} W_{i(10)}^{(q)} + x_2^{(q)} W_{i(01)}^{(q)} + x_1^{(q)} x_2^{(q)} W_{i(11)}^{(q)} + \frac{1}{2} \left(3x_1^{(q)2} - \right. \\
& \left. \frac{l_q^2}{4} \right) W_{i(20)}^{(q)} + \frac{1}{2} \left(3x_2^{(q)2} - \frac{h_q^2}{4} \right) W_{i(02)}^{(q)} + \frac{1}{2} \left(3x_1^{(q)2} - \frac{l_q^2}{4} \right) x_2^{(q)} W_{i(21)}^{(q)} + \frac{1}{2} \left(3x_2^{(q)2} - \right. \\
& \left. \frac{h_q^2}{4} \right) x_1^{(q)} W_{i(12)}^{(q)} + \frac{1}{4} \left(3x_1^{(q)2} - \frac{l_q^2}{4} \right) \left(3x_2^{(q)2} - \frac{h_q^2}{4} \right) W_{i(22)}^{(q)},
\end{aligned} \tag{2.1}$$

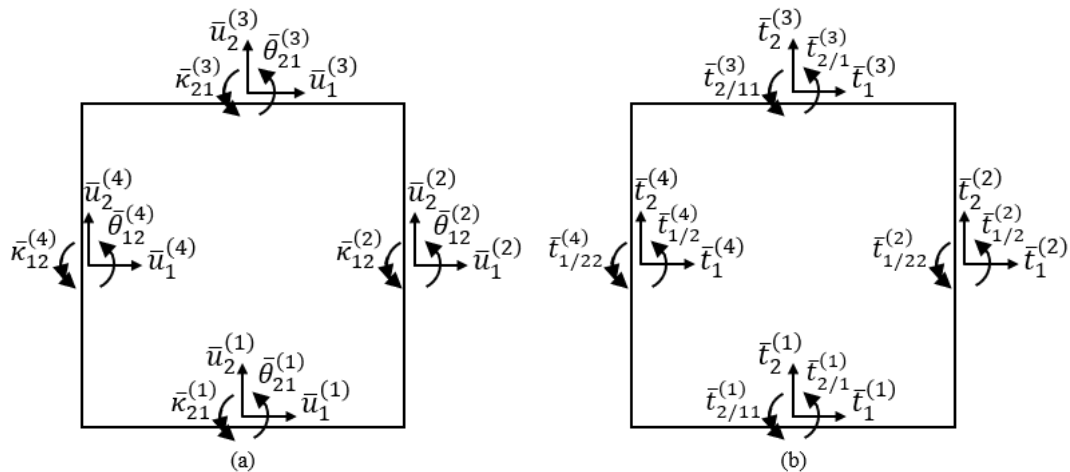
where $i = 1, 2$ and $W_{i(mn)}^{(q)}$ are the unknown coefficients of the displacement field. These coefficients are expressed as a function of the following kinematic quantities: surface-averaged displacements, rotations, and curvatures, which are responsible for determining the generalized stiffness matrices (CAVALCANTE; PINDERA, 2012a).

Figure 03 – Discretized analysis domain and local coordinate system of a generic subvolume q



Font: Adapted from Cavalcante and Pindera (2012a).

Figure 04 – Surface-averaged quantities: (a) surface-averaged kinematic quantities and (b) surface-averaged static quantities



Font: Author (2022).

Figure 4a illustrates the kinematic quantities associated with each face of a generic subvolume q . Therefore, these quantities in terms of surface-averaged displacements, rotations and curvatures can be defined, respectively, as follows

$$\begin{aligned}
\bar{u}_i^{(1,3)} &= \frac{1}{l_q} \int_{-\frac{l_q}{2}}^{\frac{l_q}{2}} u_i \left(x_1^{(q)}, \mp \frac{h_q}{2} \right) dx_1^{(q)} \\
\bar{u}_i^{(2,4)} &= \frac{1}{h_q} \int_{-\frac{h_q}{2}}^{\frac{h_q}{2}} u_i \left(\pm \frac{l_q}{2}, x_2^{(q)} \right) dx_2^{(q)} \\
\bar{\theta}_{21}^{(1,3)} &= \frac{1}{l_q} \int_{-\frac{l_q}{2}}^{\frac{l_q}{2}} \frac{\partial u_2 \left(x_1^{(q)}, \mp \frac{h_q}{2} \right)}{\partial x_1^{(q)}} dx_1^{(q)} \\
\bar{\theta}_{12}^{(2,4)} &= -\frac{1}{h_q} \int_{-\frac{h_q}{2}}^{\frac{h_q}{2}} \frac{\partial u_1 \left(\pm \frac{l_q}{2}, x_2^{(q)} \right)}{\partial x_2^{(q)}} dx_2^{(q)} \quad , \\
\bar{\kappa}_{21}^{(1,3)} &= \frac{1}{l_q} \int_{-\frac{l_q}{2}}^{\frac{l_q}{2}} \frac{\partial^2 u_2 \left(x_1^{(q)}, \mp \frac{h_q}{2} \right)}{\partial x_1^{2(q)}} dx_1^{(q)} \\
\bar{\kappa}_{12}^{(2,4)} &= -\frac{1}{h_q} \int_{-\frac{h_q}{2}}^{\frac{h_q}{2}} \frac{\partial^2 u_1 \left(\pm \frac{l_q}{2}, x_2^{(q)} \right)}{\partial x_2^{2(q)}} dx_2^{(q)}
\end{aligned} \tag{2.2}$$

where the superscript indicates the subvolume face number, indexed as illustrated in Figure 4a. The surface-averaged quantities are evaluated along the edges, assuming a unitary dimension along the x_3 coordinate axis.

Thereafter, the compatibility conditions are established in terms of the surface-averaged variables, which is motivated by the satisfaction of point-wise continuity conditions between adjacent subvolumes (CAVALCANTE; PINDERA, 2012a). Thus, the kinematic compatibilization between the third and first faces of adjacent subvolumes is established as

$$\begin{aligned}
\bar{u}_i^{(3)} \Big|^{(q)} &= \bar{u}_i^{(1)} \Big|^{(q+1)} \\
\bar{\theta}_{21}^{(3)} \Big|^{(q)} &= \bar{\theta}_{21}^{(1)} \Big|^{(q+1)} \\
\bar{\kappa}_{21}^{(3)} \Big|^{(q)} &= \bar{\kappa}_{21}^{(1)} \Big|^{(q+1)}
\end{aligned} \tag{2.3}$$

Similarly, the kinematic variables must be also compatibilized between the second and fourth faces of adjacent subvolumes. Substituting the polynomial representation of the displacement field, Eq. (2.1), in Eq. (2.2), 16 expressions are obtained for the surface-averaged displacements, rotations, and curvatures, which can be represented in matrix notation as follows

$$\begin{bmatrix} \bar{\mathbf{u}}^{(q)} \\ \bar{\boldsymbol{\theta}}^{(q)} \\ \bar{\boldsymbol{\kappa}}^{(q)} \end{bmatrix} = \mathbf{A}_{(16 \times 16)}^{(q)} \begin{bmatrix} \mathbf{W}^{(q)} \\ \mathbf{W}_{\nabla}^{(q)} \\ \mathbf{W}_{\nabla^2}^{(q)} \end{bmatrix} + \mathbf{a}_{(16 \times 2)}^{(q)} \mathbf{W}_{(00)}^{(q)}, \quad (2.4)$$

where $\bar{\mathbf{u}}^{(q)} = [\bar{u}_1^{(q,1)}, \bar{u}_2^{(q,1)}, \bar{u}_1^{(q,2)}, \bar{u}_2^{(q,2)}, \bar{u}_1^{(q,3)}, \bar{u}_2^{(q,3)}, \bar{u}_1^{(q,4)}, \bar{u}_2^{(q,4)}]^T$ is the local surface-averaged displacement vector, $\bar{\boldsymbol{\theta}}^{(q)} = [\bar{\theta}_{21}^{(q,1)}, \bar{\theta}_{12}^{(q,2)}, \bar{\theta}_{21}^{(q,3)}, \bar{\theta}_{12}^{(q,4)}]^T$ is the local surface-averaged rotation vector, $\bar{\boldsymbol{\kappa}}^{(q)} = [\bar{\kappa}_{21}^{(q,1)}, \bar{\kappa}_{12}^{(q,2)}, \bar{\kappa}_{21}^{(q,3)}, \bar{\kappa}_{12}^{(q,4)}]^T$ is the local surface-averaged curvature vector, $\mathbf{W}^{(q)} = [W_{1(10)}^{(q)}, W_{1(01)}^{(q)}, W_{1(20)}^{(q)}, W_{1(02)}^{(q)}, W_{2(10)}^{(q)}, W_{2(01)}^{(q)}, W_{2(20)}^{(q)}, W_{2(02)}^{(q)}]^T$ is the vector containing the unknown coefficients related to the zeroth-order finite-volume theory, $\mathbf{W}_{\nabla}^{(q)} = [W_{1(11)}^{(q)}, W_{2(11)}^{(q)}, W_{1(21)}^{(q)}, W_{2(12)}^{(q)}]^T$ is the vector formed by the unknown coefficients related to the first-order finite-volume theory, $\mathbf{W}_{\nabla^2}^{(q)} = [W_{1(12)}^{(q)}, W_{2(21)}^{(q)}, W_{1(22)}^{(q)}, W_{2(22)}^{(q)}]^T$ is the vector composed by the unknown coefficients related exclusively to the second-order finite-volume theory and $\mathbf{W}_{(00)}^{(q)} = [W_{1(00)}^{(q)}, W_{2(00)}^{(q)}]^T$ is the vector containing the zeroth-order unknown coefficients. $\mathbf{A}_{(16 \times 16)}^{(q)}$ and $\mathbf{a}_{(16 \times 2)}^{(q)}$ are matrices that depend on the geometric features of the subvolume q , which can be found in Araujo (2018).

Similarly, the surface-averaged static quantities, shown in Figure 4b, can be defined in terms of averaged tractions, first and second derivative of normal tractions acting on the faces of a generic subvolume. Thus, these surface-averaged static quantities are respectively defined as

$$\begin{aligned}
\bar{t}_i^{(1,3)} &= \mp \frac{1}{l_q} \int_{-\frac{l_q}{2}}^{\frac{l_q}{2}} \sigma_{2i} \left(x_1^{(q)}, \mp \frac{h_q}{2} \right) dx_1^{(q)} \\
\bar{t}_i^{(2,4)} &= \pm \frac{1}{h_q} \int_{-\frac{h_q}{2}}^{\frac{h_q}{2}} \sigma_{1i} \left(\pm \frac{l_q}{2}, x_2^{(q)} \right) dx_2^{(q)} \\
\bar{t}_{2/1}^{(1,3)} &= \mp \frac{1}{l_q} \int_{-\frac{l_q}{2}}^{\frac{l_q}{2}} \frac{\partial \sigma_{22} \left(x_1^{(q)}, \mp \frac{h_q}{2} \right)}{\partial x_1^{(q)}} dx_1^{(q)} \\
\bar{t}_{1/2}^{(2,4)} &= \mp \frac{1}{h_q} \int_{-\frac{h_q}{2}}^{\frac{h_q}{2}} \frac{\partial \sigma_{11} \left(\pm \frac{l_q}{2}, x_2^{(q)} \right)}{\partial x_2^{(q)}} dx_2^{(q)} \\
\bar{t}_{2/11}^{(1,3)} &= \mp \frac{1}{l_q} \int_{-\frac{l_q}{2}}^{\frac{l_q}{2}} \frac{\partial^2 \sigma_{22} \left(x_1^{(q)}, \mp \frac{h_q}{2} \right)}{\partial x_1^{2(q)}} dx_1^{(q)} \\
\bar{t}_{1/22}^{(2,4)} &= \mp \frac{1}{h_q} \int_{-\frac{h_q}{2}}^{\frac{h_q}{2}} \frac{\partial^2 \sigma_{11} \left(\pm \frac{l_q}{2}, x_2^{(q)} \right)}{\partial x_2^{2(q)}} dx_2^{(q)}
\end{aligned} \tag{2.5}$$

In the static analysis, the continuity conditions between the third and first faces of adjacent subvolumes are imposed as follows

$$\begin{aligned}
\bar{t}_i^{(3)} \Big|^{(q)} - \bar{t}_i^{(1)} \Big|^{(q+1)} &= 0 \\
\bar{t}_{2/1}^{(3)} \Big|^{(q)} - \bar{t}_{1/2}^{(1)} \Big|^{(q+1)} &= 0 \\
\bar{t}_{2/11}^{(3)} \Big|^{(q)} - \bar{t}_{2/11}^{(1)} \Big|^{(q+1)} &= 0
\end{aligned} \tag{2.6}$$

These continuities must also be established between the fourth and second faces of adjacent subvolumes.

Considering linear elastic isotropic materials, where the generalized Hooke's law ($\sigma_{ij}^{(q)} = C_{ijkl}^{(q)} \varepsilon_{kl}^{(q)}$) is valid, 16 expressions are obtained for the surface-averaged static variables in terms of the unknown coefficients. These expressions can be arranged in matrix notation as follows

$$\begin{bmatrix} \bar{\mathbf{t}}^{(q)} \\ \bar{\mathbf{t}}_{\nabla}^{(q)} \\ \bar{\mathbf{t}}_{\nabla^2}^{(q)} \end{bmatrix} = \mathbf{B}_{(16 \times 16)}^{(q)} \begin{bmatrix} \mathbf{W}^{(q)} \\ \mathbf{W}_{\nabla}^{(q)} \\ \mathbf{W}_{\nabla^2}^{(q)} \end{bmatrix}, \tag{2.7}$$

where $\bar{\mathbf{t}}^{(q)} = \left[\bar{t}_1^{(q,1)}, \bar{t}_2^{(q,1)}, \bar{t}_1^{(q,2)}, \bar{t}_2^{(q,2)}, \bar{t}_1^{(q,3)}, \bar{t}_2^{(q,3)}, \bar{t}_1^{(q,4)}, \bar{t}_2^{(q,4)} \right]^T$ is the local surface-averaged traction vector, $\bar{\mathbf{t}}_{\nabla}^{(q)} = \left[\bar{t}_{2/1}^{(q,1)}, \bar{t}_{1/2}^{(q,2)}, \bar{t}_{2/1}^{(q,3)}, \bar{t}_{1/2}^{(q,4)} \right]^T$ is the local surface-averaged normal traction first derivative vector and $\bar{\mathbf{t}}_{\nabla^2}^{(q)} = \left[\bar{t}_{2/11}^{(q,1)}, \bar{t}_{1/22}^{(q,2)}, \bar{t}_{2/11}^{(q,3)}, \bar{t}_{1/22}^{(q,4)} \right]^T$ is the local surface-averaged normal traction second derivative vector. $\mathbf{B}_{(16 \times 16)}^{(q)}$ is a matrix that depends on the

subvolume dimensions and the material elastic properties, which elements can be found in Araujo (2018).

In the absence of body forces, the equilibrium conditions at the subvolume level are established as

$$\sum_{p=1}^4 \bar{\mathbf{t}}_{(p)}^{(q)} L_p^{(q)} = \mathbf{0}, \quad (2.8)$$

where $L_1^{(q)} = l_q$, $L_2^{(q)} = h_q$, $L_3^{(q)} = l_q$ and $L_4^{(q)} = h_q$ are the subvolume edges lengths and $\bar{\mathbf{t}}_{(p)}^{(q)}$ is taken from Eq. (2.7) and can be expressed as

$$\bar{\mathbf{t}}_{(p)}^{(q)} = \mathbf{B}_{(2 \times 16)}^{(q,p)} \left(\mathbf{A}^{(q)} \right)^{-1} \left(\bar{\mathbf{u}}^{(q)} - \mathbf{a}^{(q)} \mathbf{W}_{(00)}^{(q)} \right), \quad (2.9)$$

where $\mathbf{B}_{(2 \times 16)}^{(q,p)}$ are submatrices of selected components of the matrix $\mathbf{B}^{(q)}$ related to the surface-averaged tractions acting on a face p of the subvolume q . Replacing Eqs. (2.4) and (2.7) in Eqs. (2.9) and (2.8), the following expression is obtained

$$\left(\sum_{p=1}^4 \mathbf{B}^{(q,p)} L_p^{(q)} \right) \left(\mathbf{A}^{(q)} \right)^{-1} \begin{bmatrix} \bar{\mathbf{u}}^{(q)} \\ \bar{\boldsymbol{\theta}}^{(q)} \\ \bar{\boldsymbol{\kappa}}^{(q)} \end{bmatrix} = \left(\sum_{p=1}^4 \mathbf{B}^{(q,p)} L_p^{(q)} \right) \left(\mathbf{A}^{(q)} \right)^{-1} \mathbf{a}^{(q)} \mathbf{W}_{(00)}^{(q)}. \quad (2.10)$$

The vector $\mathbf{W}_{(00)}^{(q)}$ can be obtained from Eq. (2.10), which is given by

$$\mathbf{W}_{(00)}^{(q)} = \bar{\mathbf{a}}_{(2 \times 16)}^{(q)} \begin{bmatrix} \bar{\mathbf{u}}^{(q)} \\ \bar{\boldsymbol{\theta}}^{(q)} \\ \bar{\boldsymbol{\kappa}}^{(q)} \end{bmatrix}, \quad (2.11)$$

where $\bar{\mathbf{a}}_{(2 \times 16)}^{(q)} = \left[\left(\sum_{p=1}^4 \mathbf{B}^{(q,p)} L_p^{(q)} \right) \left(\mathbf{A}^{(q)} \right)^{-1} \mathbf{a}^{(q)} \right]^{-1} \left(\sum_{p=1}^4 \mathbf{B}^{(q,p)} L_p^{(q)} \right) \left(\mathbf{A}^{(q)} \right)^{-1}$. Replacing Eq. (2.11) in Eq. (2.4), the following expression can be obtained:

$$\begin{bmatrix} \mathbf{W}^{(q)} \\ \mathbf{W}_{\nabla}^{(q)} \\ \mathbf{W}_{\nabla^2}^{(q)} \end{bmatrix} = \bar{\mathbf{A}}_{(16 \times 16)}^{(q)} \begin{bmatrix} \bar{\mathbf{u}}^{(q)} \\ \bar{\boldsymbol{\theta}}^{(q)} \\ \bar{\boldsymbol{\kappa}}^{(q)} \end{bmatrix}, \quad (2.12)$$

where $\bar{\mathbf{A}}_{(16 \times 16)}^{(q)} = \left(\mathbf{A}^{(q)} \right)^{-1} - \left(\mathbf{A}^{(q)} \right)^{-1} \mathbf{a}^{(q)} \bar{\mathbf{a}}^{(q)}$. Thus, the local system of equations for a generic subvolume can be obtained by replacing Eq. (2.12) in Eq. (2.7), which gives

$$\begin{bmatrix} \bar{\mathbf{t}}^{(q)} \\ \bar{\mathbf{t}}_{\nabla}^{(q)} \\ \bar{\mathbf{t}}_{\nabla^2}^{(q)} \end{bmatrix} = \mathbf{K}_{(16 \times 16)}^{(q)} \begin{bmatrix} \bar{\mathbf{u}}^{(q)} \\ \bar{\boldsymbol{\theta}}^{(q)} \\ \bar{\boldsymbol{\kappa}}^{(q)} \end{bmatrix}, \quad (2.13)$$

where $\mathbf{K}_{(16 \times 16)}^{(q)} = \mathbf{B}^{(q)} \bar{\mathbf{A}}^{(q)}$ is the local stiffness matrix, which is a not symmetric matrix.

For the global stiffness matrix assemblage, each subvolume's contribution is considered on the discretized structure. Therefore, the global system of equations can be defined as

$$\mathbf{T}_{(ndof \times 1)} = \mathbf{K}_{(ndof \times ndof)} \mathbf{U}_{(ndof \times 1)}, \quad (2.14)$$

where $ndof$ is the total number of degrees of freedom, $\mathbf{T}_{(ndof \times 1)}$ and $\mathbf{U}_{(ndof \times 1)}$ are the global surface-averaged static and kinematic vectors, respectively, and $\mathbf{K}_{(ndof \times ndof)}$ is the global stiffness matrix evaluated by

$$\mathbf{K}_{(ndof \times ndof)} = \sum_{q=1}^{N_q} \left[\left(\mathbf{L}_{(16 \times ndof)}^{(q)} \right)^T \mathbf{K}_{(16 \times 16)}^{(q)} \mathbf{L}_{(16 \times ndof)}^{(q)} \right], \quad (2.15)$$

where $\mathbf{L}_{(16 \times ndof)}^{(q)}$ is the kinematic and static incidence matrix. The global stiffness matrix is a sparse and not symmetric matrix that can be used to obtain the surface-averaged kinematic variables by the product of its inverse and the global surface-averaged static vector. The inverse bar in MatLab software can optimize this process by using a Gaussian elimination once the global stiffness matrix is square (MATLAB, 2016).

The mechanical analysis can also be evaluated in a surface-averaged sense in each subvolume in terms of strain and stress. Therefore, the local strain tensor can be obtained from the following kinematic relation:

$$\varepsilon_{ij} = \frac{1}{2} \left(\frac{\partial u_i}{\partial x_j} + \frac{\partial u_j}{\partial x_i} \right). \quad (2.16)$$

By employing the displacement field approximation presented in Eq. (2.1), the local strain tensor can be written as

$$\begin{aligned} \boldsymbol{\varepsilon}^{(q)} \left(x_1^{(q)}, x_2^{(q)} \right) &= \mathbf{E}_0^{(q)} \left(x_1^{(q)}, x_2^{(q)} \right) \mathbf{W}^{(q)} + \mathbf{E}_1^{(q)} \left(x_1^{(q)}, x_2^{(q)} \right) \mathbf{W}_{\bar{v}}^{(q)} + \\ &\mathbf{E}_2^{(q)} \left(x_1^{(q)}, x_2^{(q)} \right) \mathbf{W}_{\bar{v}^2}^{(q)}, \end{aligned} \quad (2.17)$$

where $\mathbf{E}_m^{(q)} \left(x_1^{(q)}, x_2^{(q)} \right)$ are the kinematic matrices relating the strain vector to the unknown coefficients and can be found in the Appendix B. Consequently, the local stress tensor can be obtained using the material constitutive relation as

$$\boldsymbol{\sigma}^{(q)} \left(x_1^{(q)}, x_2^{(q)} \right) = \mathbf{C}^{(q)} \boldsymbol{\varepsilon}^{(q)} \left(x_1^{(q)}, x_2^{(q)} \right), \quad (2.18)$$

where $\mathbf{C}^{(q)}$ is the constitutive matrix for linear elastic isotropic materials under plane stress state. The previous theoretical development corresponds to the formulation of the second-order version of the generalized finite-volume theory for continuum elastic structures. For the lower order versions of the generalized finite-volume theory, the framework can be obtained by uncoupling curvatures, in the case of the first-order version, and curvatures and rotations, in the case of the zeroth-order version. The vectors composed by the unknown coefficients must also be uncoupled following the corresponding version of the generalized finite-volume theory.

2.2 Finite-Volume Theory for Elastoplastic Analysis

This technique employs the volume average of the different fields that define the material behavior and imposes boundary and continuity conditions between adjacent subvolumes in an average-sense. In this contribution, it is employed an incremental formulation of the finite-volume theory that considers the elastoplastic behavior of the material. Therefore, the equilibrium equations are satisfied in an average-sense in the volume, and the incremental displacement field in the subvolume is modeled by second-order polynomials defined in local coordinates.

2.2.1 Incremental formulation of the finite-volume theory for elastoplastic analysis

Figure 3 shows the adopted rectangular domain in $x_1 - x_2$ plane with $0 \leq x_1 \leq L$ and $0 \leq x_2 \leq H$, which is discretized in N_β horizontal subvolumes and N_γ vertical subvolumes. The subvolume dimensions are l_q and h_q for $q = 1, \dots, N_q$, where $N_q = N_\beta \cdot N_\gamma$ is the total number of subvolumes. Here, we adopt the zeroth-order finite-volume theory for rectangular analysis domains discretized in rectangular subvolumes, as shown in Figure 3, and an incomplete quadratic incremental displacement field representation in the subvolume q ,

$$\begin{aligned} \Delta u_i^{(q)} = & \Delta W_{i(00)}^{(q)} + x_1^{(q)} \Delta W_{i(10)}^{(q)} + x_2^{(q)} \Delta W_{i(01)}^{(q)} + \frac{1}{2} \left(3 \left(x_1^{(q)} \right)^2 - \frac{l_q^2}{4} \right) \Delta W_{i(20)}^{(q)} + \\ & \frac{1}{2} \left(3 \left(x_2^{(q)} \right)^2 - \frac{h_q^2}{4} \right) \Delta W_{i(02)}^{(q)}, \end{aligned} \quad (2.19)$$

where $i = 1, 2$, and $\Delta W_{i(mn)}^{(q)}$ are unknown coefficients.

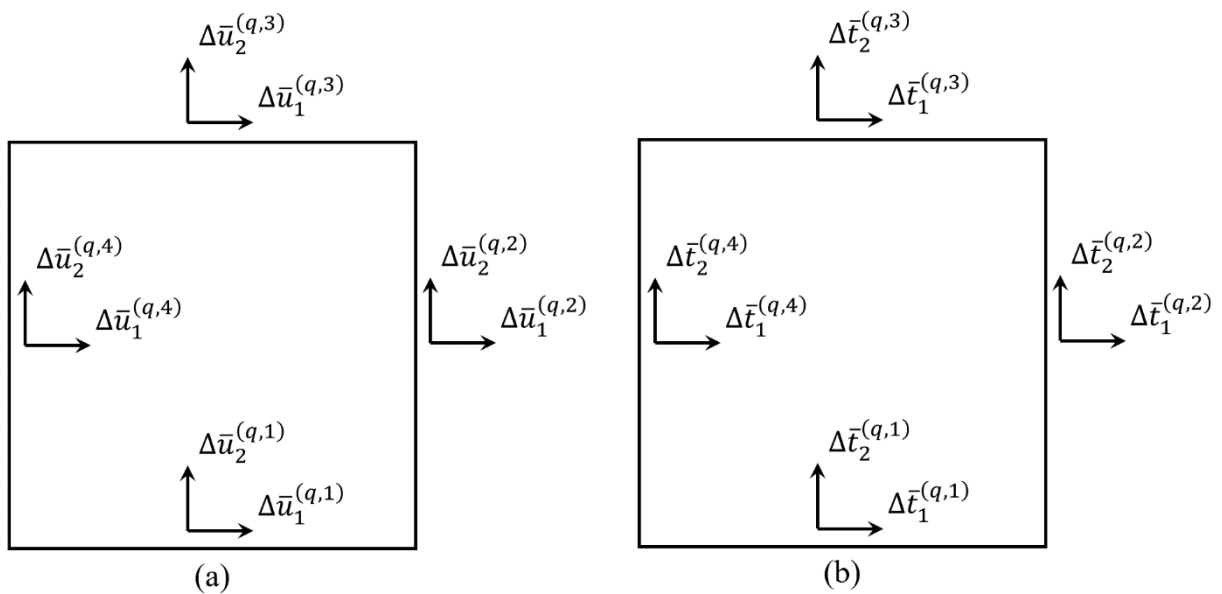
2.2.2 Local tangent stiffness matrix

The surface-averaged incremental displacement components at the subvolume faces can be evaluated by the following expressions:

$$\begin{aligned}\Delta\bar{u}_i^{(q,p)} &= \frac{1}{l_q} \int_{-l_q/2}^{+l_q/2} \Delta u_i^{(q)}(x_1^{(q)}, \mp h_q/2) dx_1^{(q)}, \text{ for } p = 1, 3 \\ \Delta\bar{u}_i^{(q,p)} &= \frac{1}{h_q} \int_{-h_q/2}^{+h_q/2} \Delta u_i^{(q)}(\pm l_q/2, x_2^{(q)}) dx_2^{(q)}, \text{ for } p = 2, 4\end{aligned}\quad (2.20)$$

where $\Delta\bar{u}_i^{(q,p)}$ are the surface-averaged incremental displacements of a generic subvolume q , Figure 5a.

Figure 05 – Surface-averaged kinematic and static quantities for a generic subvolume q : (a) surface-averaged incremental displacements and (b) surface-averaged incremental tractions



Font: Author (2022).

Employing the components of the incremental displacement field, Eq. (2.19), in Eq. (2.20), eight expressions are obtained for the surface-averaged incremental displacements as a function of the incremental displacement field coefficients. Such expressions can be organized in matrix notation as follows:

$$\Delta\bar{\mathbf{u}}^{(q)} = \mathbf{A}_{(8 \times 8)}^{(q)} \Delta\mathbf{W}^{(q)} + \mathbf{a}_{(8 \times 2)}^{(q)} \Delta\mathbf{W}_{(00)}^{(q)}, \quad (2.21)$$

where $\Delta\bar{\mathbf{u}}^{(q)} = [\Delta\bar{u}_1^{(q,1)}, \Delta\bar{u}_2^{(q,1)}, \Delta\bar{u}_1^{(q,2)}, \Delta\bar{u}_2^{(q,2)}, \Delta\bar{u}_1^{(q,3)}, \Delta\bar{u}_2^{(q,3)}, \Delta\bar{u}_1^{(q,4)}, \Delta\bar{u}_2^{(q,4)}]^T$ is the surface-averaged incremental displacement vector, $\Delta\mathbf{W}^{(q)} = [\Delta W_{1(10)}^{(q)}, \Delta W_{1(01)}^{(q)}, \Delta W_{1(20)}^{(q)}, \Delta W_{1(02)}^{(q)}, \dots, \Delta W_{2(02)}^{(q)}]^T$ is the vector containing the first and second order unknown coefficients and $\Delta\mathbf{W}_{(00)}^{(q)} = [\Delta W_{1(00)}^{(q)}, \Delta W_{2(00)}^{(q)}]^T$ is the vector

containing the zeroth-order unknown coefficients. The matrices $\mathbf{A}_{(8 \times 8)}^{(q)}$ and $\mathbf{a}_{(8 \times 2)}^{(q)}$ can be found in the Appendix A. Therefore, the vector $\Delta \mathbf{W}^{(q)}$ can be evaluated as a function of $\Delta \bar{\mathbf{u}}^{(q)}$ and $\Delta \mathbf{W}_{(00)}^{(q)}$ as follows:

$$\Delta \mathbf{W}^{(q)} = \left(\mathbf{A}^{(q)} \right)^{-1} \Delta \bar{\mathbf{u}}^{(q)} - \left(\mathbf{A}^{(q)} \right)^{-1} \mathbf{a}^{(q)} \Delta \mathbf{W}_{(00)}^{(q)}. \quad (2.22)$$

Employing Cauchy's relations, the components of the incremental traction vectors, acting in an averaged sense on the faces of a generic subvolume q , can be expressed as shown:

$$\begin{aligned} \Delta \bar{t}_i^{(q,p)} &= \mp \frac{1}{l_q} \int_{-l_q/2}^{+l_q/2} \Delta \sigma_{2i} \left(x_1^{(q)}, \mp h_q/2 \right) dx_1^{(q)}, \text{ for } p = 1, 3 \\ \Delta \bar{t}_i^{(q,p)} &= \pm \frac{1}{h_q} \int_{-h_q/2}^{+h_q/2} \Delta \sigma_{1i} \left(\pm l_q/2, x_2^{(q)} \right) dx_2^{(q)}, \text{ for } p = 2, 4 \end{aligned} \quad (2.23)$$

Applying the kinematic relations between strains and displacements and the tangent constitutive relationship, eight expressions in terms of the unknown coefficients can be obtained and organized in matrix notation as follows:

$$\Delta \bar{\mathbf{t}}^{(q)} = \mathbf{B}_{(8 \times 8)}^{(q)} \Delta \mathbf{W}^{(q)}, \quad (2.24)$$

where $\Delta \bar{\mathbf{t}}^{(q)} = \left[\Delta t_1^{(q,1)}, \Delta t_2^{(q,1)}, \Delta t_1^{(q,2)}, \Delta t_2^{(q,2)}, \Delta t_1^{(q,3)}, \Delta t_2^{(q,3)}, \Delta t_1^{(q,4)}, \Delta t_2^{(q,4)} \right]^T$ is the surface-averaged incremental traction vector, Figure 4b. The matrix $\mathbf{B}_{(8 \times 8)}^{(q)}$ can be found in the Appendix A.

In the absence of body forces, the satisfaction of equilibrium conditions is ensured by the following expression:

$$\sum_{p=1}^4 \Delta \bar{\mathbf{t}}^{(q,p)} L_p^{(q)} = \mathbf{0}_{(2 \times 1)}, \quad (2.25)$$

where $L_1^{(q)} = l_q$, $L_2^{(q)} = h_q$, $L_3^{(q)} = l_q$ e $L_4^{(q)} = h_q$ are the faces' lengths of the subvolume q , and $\Delta \bar{\mathbf{t}}^{(q,p)}$ can be evaluate as follows

$$\Delta \bar{\mathbf{t}}^{(q,p)} = \mathbf{B}_{(2 \times 8)}^{(q,p)} \left(\mathbf{A}^{(q)} \right)^{-1} \Delta \bar{\mathbf{u}}^{(q)} - \mathbf{B}_{(2 \times 8)}^{(q,p)} \left(\mathbf{A}^{(q)} \right)^{-1} \mathbf{a}^{(q)} \Delta \mathbf{W}_{(00)}^{(q)}, \quad (2.26)$$

where $\mathbf{B}_{(2 \times 8)}^{(q,p)}$ are composed by different two lines of $\mathbf{B}^{(q)}$.

Substituting Eq. (2.26) in Eq. (2.25), the following equation can be developed:

$$\left(\sum_{p=1}^4 \mathbf{B}^{(q,p)} L_p^{(q)} \right) \left(\mathbf{A}^{(q)} \right)^{-1} \Delta \bar{\mathbf{u}}^{(q)} - \left(\sum_{p=1}^4 \mathbf{B}^{(q,p)} L_p^{(q)} \right) \left(\mathbf{A}^{(q)} \right)^{-1} \mathbf{a}^{(q)} \Delta \mathbf{W}_{(00)}^{(q)} = \mathbf{0}. \quad (2.27)$$

From Eq. (2.27), the vector $\Delta \mathbf{W}_{(00)}^{(q)}$ can be evaluated as

$$\Delta \mathbf{W}_{(00)}^{(q)} = \bar{\mathbf{a}}_{(2 \times 8)}^{(q)} \Delta \bar{\mathbf{u}}^{(q)}, \quad (2.28)$$

$$\text{where } \bar{\mathbf{a}}_{(2 \times 8)}^{(q)} = \left[\left(\sum_{p=1}^4 \mathbf{B}^{(q,p)} L_p^{(q)} \right) \left(\mathbf{A}^{(q)} \right)^{-1} \mathbf{a}^{(q)} \right]^{-1} \left(\sum_{p=1}^4 \mathbf{B}^{(q,p)} L_p^{(q)} \right) \left(\mathbf{A}^{(q)} \right)^{-1}.$$

By replacing Eq. (2.28) in Eq. (2.21), the following expression can be obtained:

$$\Delta \mathbf{W}^{(q)} = \bar{\mathbf{A}}_{(8 \times 8)}^{(q)} \Delta \bar{\mathbf{u}}^{(q)}, \quad (2.29)$$

$$\text{where } \bar{\mathbf{A}}_{(8 \times 8)}^{(q)} = \left(\mathbf{A}^{(q)} \right)^{-1} - \left(\mathbf{A}^{(q)} \right)^{-1} \mathbf{a}^{(q)} \bar{\mathbf{a}}^{(q)}.$$

Finally, replacing Eq. (2.29) in Eq. (2.24), the local system of equations is obtained for a generic subvolume as follows:

$$\Delta \bar{\mathbf{t}}^{(q)} = \mathbf{K}_{(8 \times 8)}^{(q)} \Delta \bar{\mathbf{u}}^{(q)}, \quad (2.30)$$

where $\mathbf{K}_{(8 \times 8)}^{(q)} = \mathbf{B}^{(q)} \bar{\mathbf{A}}^{(q)}$ is the local tangent stiffness matrix of a generic subvolume q .

2.2.3 Global tangent stiffness matrix assemblage

The global tangent stiffness matrix of the structure is assembled considering the individual contribution of each subvolume of the discretized domain. If the structure is subdivided in $N_q = N_\beta N_\gamma$ subvolumes, considering two degrees of freedom per face, we have $ndof = 2N_\beta(N_\gamma + 1) + 2(N_\beta + 1)N_\gamma$ degrees of freedom for the structure. Based on the kinematic and static compatibility conditions, the expression that defines the global system of equations can be written as

$$\Delta \mathbf{T}_{(ndof \times 1)} = \mathbf{K}_{(ndof \times ndof)} \Delta \mathbf{U}_{(ndof \times 1)}, \quad (2.31)$$

where $\Delta \mathbf{U}_{(ndof \times 1)}$ and $\Delta \mathbf{T}_{(ndof \times 1)}$ are the global surface-averaged incremental displacement vector and the global surface-averaged incremental traction vector, respectively, and the global tangent stiffness matrix can be obtained by the following equation:

$$\mathbf{K}_{(ndof \times ndof)} = \sum_{q=1}^{N_q} \left[\left(\mathbf{L}_{(8 \times ndof)}^{(q)} \right)^T \mathbf{K}_{(8 \times 8)}^{(q)} \mathbf{L}_{(8 \times ndof)}^{(q)} \right], \quad (2.32)$$

where $\mathbf{L}_{(8 \times ndof)}^{(q)}$ and $\left(\mathbf{L}_{(8 \times ndof)}^{(q)} \right)^T$ are the kinematic and static compatibility matrices of the structure, respectively.

2.2.4 Tangent material stiffness matrix

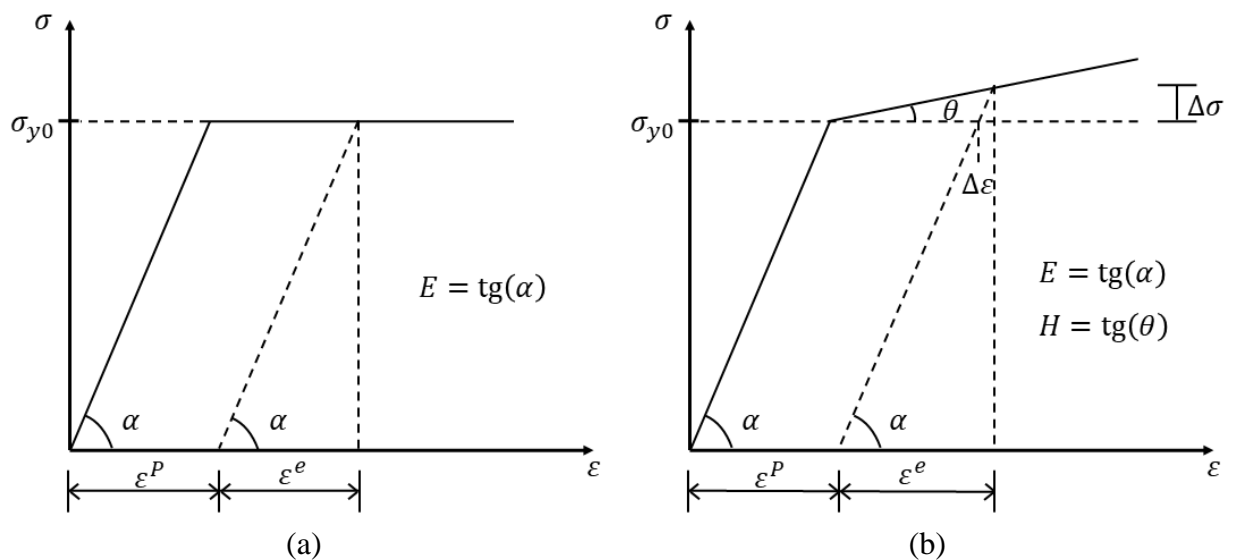
The elastoplastic behavior is characterized by an initially elastic material response and, from a certain stress level, by an essentially plastic behavior. The elastic behavior is reversible, and its domain is delimited by the yield surface, which, if exceeded, will lead to a plastic behavior. The plastic behavior of the material is generally accompanied by invariance of its volume. Two uniaxial models of elastoplastic behavior of the material are explained below, as well as their respective formulations and graphic representations.

Elastic perfectly plastic model: In this uniaxial model, the material will present linear elastic behavior until reaching the yield stress (σ_y). From this stress level, the material will show a perfectly plastic behavior, i.e., without work hardening of the material. Figure 6a illustrates this model in more details. Considering the definition of this model and its graphical representation, it follows this mathematical expression for the yield stress:

$$\sigma_y(\varepsilon_P) = \sigma_{y0} \quad (2.33)$$

where σ_{y0} is the initial yield stress of the material and ε_P is the plastic strain.

Figure 06 – Uniaxial elastoplastic material models



Font: Author (2022).

Bilinear elastoplastic model: In this uniaxial model, the material will present a linear elastic behavior until reaching the yield stress (σ_y). From this stress level, the material will start to show a plastic behavior with linear hardening. In other words, the stress must be increased linearly along with the evolution of the plastic strain. Figure 6b illustrates this

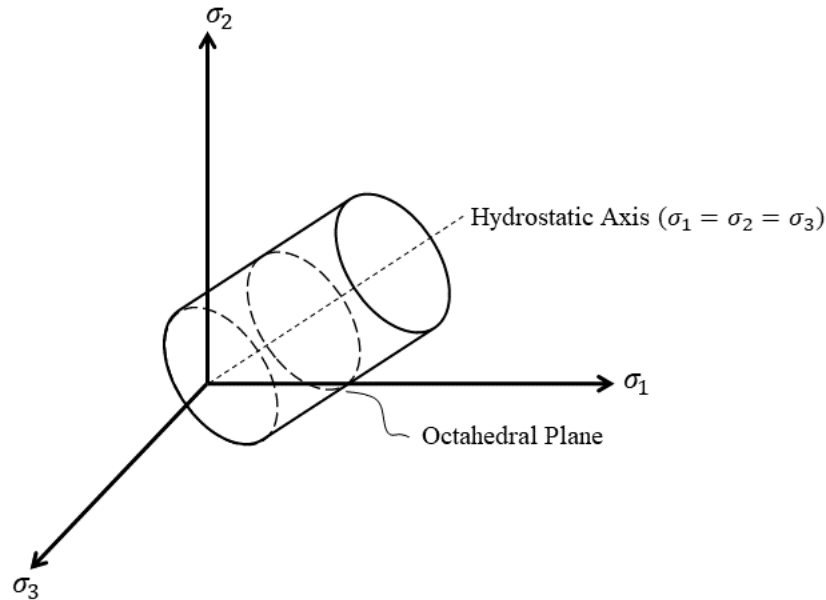
model more detailed. Considering the definition of this model and its graphical representation, it gives the following expression for the yield stress:

$$\sigma_y(\varepsilon_p) = \sigma_{y0} + \frac{EH}{E - H} \varepsilon_p \quad (2.34)$$

where E is the elastic modulus and H is the hardening coefficient of the material.

The plastic behavior is conditioned to a yield criterion. The von Mises yield criterion for elastoplastic materials with isotropic hardening can be geometrically represented by an infinite circular cylinder with radius equal to $\sqrt{\frac{2}{3}} \sigma_y(\varepsilon_p)$, represented in the coordinate system σ_1 , σ_2 and σ_3 (principal stresses), as shown in Figure 7.

Figure 07 – Geometric representation of the von Mises yield criterion



Font: Author (2022).

The multi-axial von Mises yield function in terms of the principal stresses considering an isotropic hardening can be mathematically expressed as follows:

$$f(\sigma_1, \sigma_2, \sigma_3, \varepsilon_p) = \sigma_{vm}(\sigma_1, \sigma_2, \sigma_3) - \sigma_y(\varepsilon_p) \quad (2.35)$$

where $\sigma_{vm}(\sigma_1, \sigma_2, \sigma_3) = \sqrt{\frac{1}{2}[(\sigma_1 - \sigma_2)^2 + (\sigma_2 - \sigma_3)^2 + (\sigma_3 - \sigma_1)^2]}$ is the equivalent von Mises stress and $\varepsilon_p = \sqrt{\frac{2}{3}[(\varepsilon_1^p)^2 + (\varepsilon_2^p)^2 + (\varepsilon_3^p)^2]}$ is the effective plastic strain for an incompressible plastic material, with ε_i^p being a principal plastic strain component.

The exact tangent material stiffness matrix $\mathbf{C}^{(q)}$ employed in the proposed incremental elastoplastic formulation of the finite-volume theory can be evaluated for the elastic perfectly plastic material, Eq. (2.36), and the bilinear elastoplastic material, Eq. (2.37), as follows:

$$\mathbf{C}^{(q)} = \mathbf{C}_{el}^{(q)} \quad \text{for } \sigma_{vm}(\sigma_1, \sigma_2, \sigma_3) < \sigma_y(\varepsilon_p)$$

$$\mathbf{C}^{(q)} = \mathbf{C}_{el}^{(q)} \left[\mathbf{I} - \frac{\mathbf{1}}{\left(\frac{\partial f}{\partial \boldsymbol{\sigma}}\right)^T \mathbf{C}_{el}^{(q)} \left(\frac{\partial f}{\partial \boldsymbol{\sigma}}\right)} \left(\frac{\partial f}{\partial \boldsymbol{\sigma}}\right) \left(\frac{\partial f}{\partial \boldsymbol{\sigma}}\right)^T \mathbf{C}_{el}^{(q)} \right] \quad \text{for } \sigma_{vm}(\sigma_1, \sigma_2, \sigma_3) \geq \sigma_y(\varepsilon_p) \quad (2.36)$$

$$\mathbf{C}^{(q)} = \mathbf{C}_{el}^{(q)} \quad \text{for } \sigma_{vm}(\sigma_1, \sigma_2, \sigma_3) < \sigma_y(\varepsilon_p)$$

$$\mathbf{C}^{(q)} = \mathbf{C}_{el}^{(q)} \left[\mathbf{I} - \frac{\mathbf{1}}{\left(\frac{\partial f}{\partial \boldsymbol{\sigma}}\right)^T \mathbf{C}_{el}^{(q)} \left(\frac{\partial f}{\partial \boldsymbol{\sigma}}\right) - \left(\frac{\partial f}{\partial \varepsilon_p}\right) \sqrt{\frac{2}{3} \left(\frac{\partial f}{\partial \boldsymbol{\sigma}}\right)^T \left(\frac{\partial f}{\partial \boldsymbol{\sigma}}\right)}} \left(\frac{\partial f}{\partial \boldsymbol{\sigma}}\right) \left(\frac{\partial f}{\partial \boldsymbol{\sigma}}\right)^T \mathbf{C}_{el}^{(q)} \right] \quad \text{for } \sigma_{vm}(\sigma_1, \sigma_2, \sigma_3) \geq \sigma_y(\varepsilon_p) \quad (2.37)$$

where \mathbf{I} is the identity matrix and $\mathbf{C}_{el}^{(q)}$ is the elastic material stiffness matrix. In the evaluation of the exact tangent material stiffness matrix was considered the elastic modulus $E_q(\rho_q) = \rho_q^p E_0$, the hardening coefficient $H_q(\rho_q) = \rho_q^p H_0$ and the initial yield stress $\sigma_{y0}^{(q)} = \rho_q^p \sigma_{y0}^0$, being ρ_q the relative density of the material, p the penalization factor, and E_0 , H_0 and σ_{y0}^0 the reference elastic modulus, hardening coefficient and initial yield stress, respectively.

The plane stress state condition is satisfied through the constitutive relationship that relates stress with elastic strain:

$$\Delta \boldsymbol{\sigma}^{(q)} = \mathbf{C}_{el}^{(q)} \Delta \boldsymbol{\varepsilon}_{el}^{(q)} = \mathbf{C}_{el}^{(q)} \left(\Delta \boldsymbol{\varepsilon}^{(q)} - \Delta \boldsymbol{\varepsilon}_p^{(q)} \right) \quad (2.38)$$

where $\Delta \boldsymbol{\sigma}^{(q)}$ is the stress increment vector, $\Delta \boldsymbol{\varepsilon}^{(q)}$ is the strain increment vector, $\Delta \boldsymbol{\varepsilon}_{el}^{(q)}$ is the elastic strain increment vector and $\Delta \boldsymbol{\varepsilon}_p^{(q)}$ is the plastic strain increment vector in the subvolume q .

The associated von Mises flow rule, which results in the Prandtl-Reuss equations, establishes a relationship between the infinitesimal plastic strain vector with the infinitesimal strain vector, which results in the exact tangent material stiffness matrix shown in Eqs. (2.36) and (2.37). In the case of an infinitesimal analysis, this procedure satisfies the consistency condition (maintenance of the stress state on the yield surface). However, the consistency condition is no longer satisfied for a purely incremental formulation, demanding an iterative-

incremental formulation based on the radial return method and the consistent elastoplastic stiffness matrix proposed by Simo and Taylor (1986). Thus, the employment of an incremental elastoplastic formulation based on an exact tangent material stiffness matrix, which relates the infinitesimal stress vector with the infinitesimal strain vector, can satisfy the plane stress state, not the consistency condition. Thereafter, it is necessary to adopt very small increments of loading to approximately satisfy the consistency condition in the analysis domain. Besides, the out-of-plane strain component can be evaluated by employing the elastic constitutive relationship for the elastic part and the plastic incompressibility for the plastic part, as shown below:

$$\Delta\varepsilon_{3(el)}^{(q)} = -\nu_q \left(\Delta\varepsilon_{1(el)}^{(q)} + \Delta\varepsilon_{2(el)}^{(q)} \right) \quad (2.39)$$

$$\Delta\varepsilon_{3(p)}^{(q)} = -\Delta\varepsilon_{1(p)}^{(q)} - \Delta\varepsilon_{2(p)}^{(q)} \quad (2.40)$$

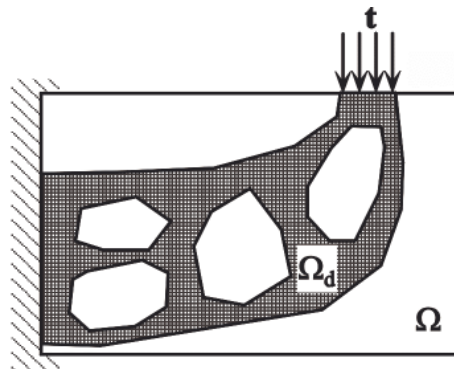
$$\Delta\varepsilon_3^{(q)} = \Delta\varepsilon_{3(el)}^{(q)} + \Delta\varepsilon_{3(p)}^{(q)} \quad (2.41)$$

3 TOPOLOGY OPTIMIZATION PROBLEMS

In general, the topology optimization problem is formulated as an algorithm that seeks to find the best material distribution inside a reference domain. Basically, a topology optimization problem consists of finding a subdomain Ω_d , with a volume limit of \bar{V} , included in a prescribed design domain Ω , which optimizes a given objective function, as illustrated in Figure 8. By introducing a density function ρ , defined in Ω , that assumes values of 1 in Ω_d and 0 in the other points of the design domain, thus, a topology optimization problem with volume constraint can be defined as follows

$$\left\{ \begin{array}{l} \min g_0(\rho) \\ \text{subject to:} \\ \int_{\Omega} \rho d\Omega \leq \bar{V}, \\ \rho(x) = 0 \text{ or } 1, \quad \forall x \in \Omega \end{array} \right. , \quad (3.1)$$

Figure 08 – Topology optimization problem domains



Font: Adapted from Silva (2003).

3.1 Material Model

Since the optimization problem presented in Equation (3.1) has a high complexity, which can generate an integer optimization, the SIMP model is employed with the intention to model the material distribution adequately (KIYONO et al., 2016). The relaxation promoted by the SIMP method consists of increasing the design domain, thus, the relative density, which on the original problem could only assume values of 0 or 1, according to the presence of material, can assume any real value between 0 and 1 ($0 < \rho \leq 1$), providing a project with different tones of gray. Intermediate values for ρ can have different interpretations, such as thickness or porosity (KIYONO et al., 2016). Here, the purpose is to avoid intermediate values employing the following power-law formulation:

$$E(\rho) = \eta_c(\rho)E_0, \quad (3.2)$$

where $E(\rho)$ is the Young modulus at density ρ , E_0 is the Young modulus of the solid material, and $\eta_c(\rho) = \rho^p$ (LE et al., 2010), where p is the penalization power used to push ρ towards to 0 or 1 (BRUGGI, 2008).

As well known, the gradient-based algorithms can present problems to find a global minimum, once small changes in the simulation parameters can result in a local minimum instead of a global minimum solution. These problems occur due to the loss of convexity when a value larger than one is assumed to the density penalty factor. Different procedures have been suggested to minimize this problem, for instance, the continued penalization scheme, where a gradual increase to the density penalty factor is employed during the optimization process, reduces the local minima effects by providing a gradual convergence to the overall optimization problem (CHRISTENSEN; KLARBRING, 2009). For compliance minimization problems, the penalty factor's value can increase gradually from 1 to 4, which provides a gradual convergence to the optimization process and reduces the local minima issue's effects.

3.2 Compliance Minimization Problem

In the last three decades, since the work of Bendsøe and Kikuchi (1988), a significant part of the advances in topology optimization has been achieved by employing methodologies based on structural compliance minimization problems, defined from the work done by external loading in the energy analysis (COLLET et al., 2017). Some examples of applications using this type of optimization problem are presented in Rozvany (2009), Vatanabe et al. (2016), Shobeiri (2016), and Wang et al. (2017). More recent studies on this field can be found in Ferrari and Sigmund (2020), Li et al. (2020), and Zhao et al. (2020). Here, the minimum compliance topology optimization problem is employed due to its low complexity, which facilitates the interpretation and production of good results.

The topology optimization problem based on the power-law approach applied in the context of the finite element method, where the objective is to minimize the compliance structural function under a volume constraint, can be described as

$$\left\{ \begin{array}{l} \min c(\boldsymbol{\rho}) = \sum_{q=1}^N (\rho_q)^p \mathbf{d}_q^T \mathbf{K}_q^0 \mathbf{d}_q \\ \text{subject to:} \\ \quad \frac{V(\boldsymbol{\rho})}{\bar{V}} = f \\ \quad 0 < \rho_{min} \leq \rho_q \leq 1 \end{array} \right. , \quad (3.3)$$

where $V(\boldsymbol{\rho})$ and \bar{V} are the material and the reference domain volumes, respectively, \mathbf{d}_q is the local displacement vector, \mathbf{K}_q^0 is the local stiffness matrix for a unitary relative density, $\boldsymbol{\rho}$ is the relative density vector, f is the prescribed volume fraction, ρ_{min} is the minimum relative density, ρ_q is the relative density associated with each element and N is the total number of elements.

3.3 OC Method

The optimization problems presented in Equation (3.3) can be solved by using the classical approach denoted by optimality criteria (OC) method. Therefore, following the procedure suggested by Bendsøe and Sigmund (2003), a heuristic update for the design variables is established as

$$\rho_q^{k+1} = \begin{cases} \max(\rho_{min}, \rho_q - m), & \text{if } \rho_q^k B_q^\eta \leq \max(\rho_{min}, \rho_q - m) \\ \rho_q^k B_q^\eta, & \text{if } \max(\rho_{min}, \rho_q - m) < \rho_q^k B_q^\eta < \min(1, \rho_q + m), \\ \min(1, \rho_q + m), & \text{if } \min(1, \rho_q + m) \leq \rho_q^k B_q^\eta \end{cases} \quad (3.4)$$

where k is the current iteration, m is the move-limit, η is the damping factor and B_q is given by

$$B_q = -\frac{\frac{\partial c}{\partial \rho_q}}{\lambda \frac{\partial f}{\partial \rho_q}}, \quad (3.5)$$

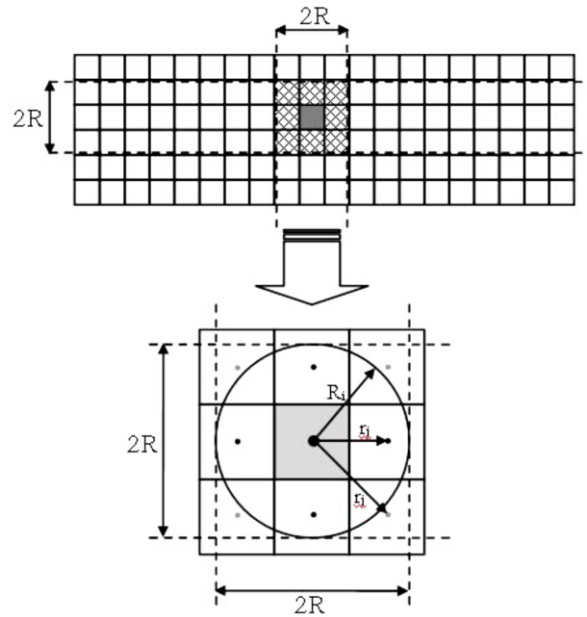
where λ is the Lagrangian multiplier for the constrained volume, which is determined by a bisection method.

The damping factor can be used to regularize possible oscillations during the optimization, mainly when no filtering techniques are employed. The parameter η is directly related to the method performance, once this affects the speed variation of B_q^η (Montes, 2016). A high value for η can accelerate the optimization convergence process, which may cause oscillations in the displacement field for the low-density regions (Ma et al., 1993). Also, the adoption of minor values of η can prevent divergence in the topology optimization algorithm; however, this results in small changes in the design variables, which leads to a slower

convergence process (Ma et al., 1993). The value of η that provides the faster convergence for the overall process is $1/2$, so it is recommended to maintain the damping factor as close as possible of this value.

3.4 Mesh-Independency Filter

Figure 09 – Elements or subvolumes participating in filtering for one element or subvolume



Font: Pedersen et al. (2006).

The problems related to mesh-dependency numerical issue can be solved by applying filtering techniques, as introduced by Sigmund (1994 and 1997). To avoid the occurrence of mesh dependency, it is suggested the modification of the elements' sensitivities by the following expression:

$$\frac{\partial c}{\partial \rho_q} = \frac{1}{\rho_q \sum_{f=1}^N \hat{H}_f} \sum_{f=1}^N \hat{H}_f \rho_f \frac{\partial c}{\partial \rho_f}, \quad (3.6)$$

where \hat{H}_f is the convolution operator (weighting function) given as

$$\hat{H}_f = R - \text{dist}(q, f) \text{ for } \text{dist}(q, f) \leq R \text{ and } \hat{H}_f = 0 \text{ otherwise,} \quad (3.7)$$

where $\text{dist}(q, f)$ is the distance between the element center of e and the element center of f (SIGMUND, 2001). To consider the contribution only of the neighbor elements (with shared nodes), it is adopted a filter radius of $R = 1.01 \sqrt{(l_q)^2 + (h_q)^2}$, as illustrated by the filter

radius R_i represented in Figure 9. According to Sigmund (2007), the main idea, beyond the

mesh-independency filtering, is to base design updates on filtered sensitivities instead of the real values for sensitivities. As a result, this is a potential risk approach, especially in cases of line-search-based optimization schemes, since the sensitivity data may not represent a descent direction; therefore, the optimization may stop prematurely. On the other hand, several applications have shown that this method is robust and reliable for the most popular optimization tools (SIGMUND, 2007).

4 COMPLIANCE ESTIMATION FOR THE GENERALIZED FINITE-VOLUME THEORY

In general, the total strain energy of a deforming material and the work done by external loading are equivalent to a conservative internal force system in a quasi-static analysis. Therefore, in structural analysis, this principle is mostly observed on energy-based numerical methods, as the finite element method. However, in the finite-volume theory, this feature is observed only for the zeroth-order version of the generalized finite-volume theory, once the local equilibrium is established only in terms of the surface-averaged tractions. In the higher-order versions of the generalized finite-volume theory, there is a residual difference between the work done by external forces and the total strain energy, especially when the employed mesh is not sufficiently fine. This contribution addresses numerical approaches to compute the total strain energy and the work done by external loading of continuum elastic structures based on the generalized finite-volume theory, which assists in defining the compliance function for the proposed optimization problem.

The compliance function can be defined as twice the total strain energy produced by a displacement field \mathbf{u} ; thus, this function can be expressed as

$$c(\mathbf{u}, \boldsymbol{\rho}) = 2U(\mathbf{u}, \boldsymbol{\rho}) = \iiint_{\Omega} 2\bar{U}(\mathbf{u}, \boldsymbol{\rho}) d\Omega = \iiint_{\Omega} \sigma_{ij}(\mathbf{u}, \boldsymbol{\rho}) \varepsilon_{ij}(\mathbf{u}) d\Omega = \iiint_{\Omega} C_{ijkl}(\boldsymbol{\rho}) \varepsilon_{kl}(\mathbf{u}) \varepsilon_{ij}(\mathbf{u}) d\Omega, \quad (4.1)$$

where $U(\mathbf{u}, \boldsymbol{\rho})$ is the total strain energy, $\bar{U}(\mathbf{u}, \boldsymbol{\rho})$ is the specific strain energy, $\sigma_{ij}(\mathbf{u}, \boldsymbol{\rho})$ is the stress tensor, $\varepsilon_{ij}(\mathbf{u})$ is the strain tensor, and $C_{ijkl}(\boldsymbol{\rho})$ is the stiffness tensor.

From the definition of work done by external surface loading in a solid domain, not considering the inertial and gravity effects, suitable for quasi-static analysis, the work done by external loading can be defined as

$$W = \frac{1}{2} \iint_{S_{\sigma}} t_i u_i dS, \quad (4.2)$$

where S_{σ} is the external surface subjected to external loading, S_u is the external surface with predicted displacements and $S = S_u \cup S_{\sigma}$.

Applying Cauchy's law and the divergence theorem to Equation (4.2), it follows

$$2W = \iiint_{\Omega} \frac{\partial \sigma_{ji}}{\partial x_j} u_i d\Omega + \iiint_{\Omega} \sigma_{ij} \varepsilon_{ij} d\Omega + \iiint_{\Omega} \sigma_{ji} \omega_{ij} d\Omega, \quad (4.3)$$

where $\omega_{ij} = 1/2 (\partial u_i / \partial x_j - \partial u_j / \partial x_i)$ is the asymmetric rotation tensor. Considering the symmetry of σ_{ij} , Equation (4.3) can be written as

$$2W = \iiint_{\Omega} \frac{\partial \sigma_{ji}}{\partial x_j} u_i d\Omega + 2U(\mathbf{u}). \quad (4.4)$$

Considering the equilibrium stress state, where $\partial \sigma_{ji} / \partial x_j = 0$, the compliance can be estimated as

$$c(\mathbf{u}, \boldsymbol{\rho}) = 2U(\mathbf{u}, \boldsymbol{\rho}) = 2W(\mathbf{u}, \boldsymbol{\rho}) = \iint_S t_i u_i dS, \quad (4.5)$$

where t_i represent the traction vector components.

The previous assumption is valid for the formulation based on the zeroth-order finite-volume theory once the equilibrium established in Equation (2.8) also satisfies the differential equilibrium equations. However, for consistency with the assumed displacement field, the strain energy and the external work must be evaluated considering the polynomial approximation inside the subvolumes, as shown in the next sections. As a result, there is no guarantee of equivalence between work done by external loading and total strain energy for the higher-order versions of the generalized finite-volume theory, since the equilibrium established in Equation (2.8) does not guarantee the satisfaction of the differential equilibrium equations, which is satisfied when a sufficiently fine mesh is employed. This contribution considered the absence of volume forces for simplification. However, the energy balance must also be satisfied when considering the volume forces once they also produce internal and external energy in a deforming material.

The energy balance is always satisfied in the finite element method. The finite element formulation employed in this investigation can be developed from the virtual work principle for elastic systems subject to conservative forces or the minimum total potential energy principle. The application of these principles for quasi-static analysis results in the equality between the work done by external loading and the total strain energy, even in the finite-element scenario, once kinematically admissible displacements are employed (SHAMES; DYM, 1986). For the employed finite element formulation, the following energy analysis can be done, starting with the definition of the total strain energy

$$U = \frac{1}{2} \iiint_{\Omega} \boldsymbol{\sigma}^T \boldsymbol{\varepsilon} d\Omega = \frac{1}{2} \iiint_{\Omega} \boldsymbol{\varepsilon}^T \mathbf{C}^T \boldsymbol{\varepsilon} d\Omega = \frac{1}{2} \iiint_{\Omega} \boldsymbol{\varepsilon}^T \mathbf{C} \boldsymbol{\varepsilon} d\Omega, \quad (4.6)$$

where $\boldsymbol{\sigma}$ and $\boldsymbol{\varepsilon}$ are the vectors with the stress and strain components, respectively, and \mathbf{C} is the stiffness material matrix.

Using the definition of the strain displacement matrix \mathbf{B} (SHAMES; DYM, 1986), it follows

$$U = \frac{1}{2} \mathbf{d}^T \iiint_{\Omega} \mathbf{B}^T \mathbf{C} \mathbf{B} d\Omega \mathbf{d} = \frac{1}{2} \mathbf{d}^T \mathbf{K} \mathbf{d} = \frac{1}{2} \mathbf{d}^T \mathbf{F}, \quad (4.7)$$

where \mathbf{d} is the global displacement vector, \mathbf{K} is the global stiffness matrix, and \mathbf{F} is the global force vector. In the absence of body forces, the work done by external loading can be evaluated as follows

$$W = \frac{1}{2} \iint_S \mathbf{u}^T \mathbf{t} dS = \frac{1}{2} \mathbf{d}^T \iint_S \mathbf{N}^T \mathbf{t} dS = \frac{1}{2} \mathbf{d}^T \mathbf{F}, \quad (4.8)$$

where \mathbf{u} is the displacement vector, \mathbf{t} is the surface stress vector, and \mathbf{N} is the matrix with the shape functions (SHAMES; DYM, 1986). This results in the equality between the total strain energy and the work done by external loading.

On the other hand, the local equilibrium in the element level is not guaranteed, only for the linear triangular finite element, where the stress field is constant, and the differential equilibrium equations are satisfied. The displacement finite element formulation explored in this investigation satisfies the local equilibrium only at the nodes and at the element level when a sufficiently refined mesh is employed. In the linear triangular finite element, the differential equilibrium equations' satisfaction results in the local satisfaction of equilibrium at the element level, and this can be demonstrated by applying Cauchy's stress formula and the divergence theorem. In the absence of body forces, the force resultant at the finite element can be evaluated as follows

$$R_i = \iint_{S_e} t_i dS_e = \iint_{S_e} \sigma_{ji} n_j dS_e = \iiint_{\Omega_e} \frac{\partial \sigma_{ji}}{\partial x_j} d\Omega_e, \quad (4.9)$$

where n_j is the outward normal vector to the finite element surface S_e . Thus, in the absence of body forces, the equilibrium can be satisfied, $R_i = 0$, when the differential equilibrium equations are identically satisfied, $\partial \sigma_{ji} / \partial x_j = 0$, which is the case for the linear triangular finite element.

4.1 Strain Energy Evaluation by the Generalized Finite-Volume Theory

The total structural strain energy is a function of strains and stresses acting on a solid as follows

$$U = \iiint_{\Omega} \frac{1}{2} \boldsymbol{\sigma}^T \boldsymbol{\varepsilon} d\Omega = \iiint_{\Omega} \frac{1}{2} \boldsymbol{\varepsilon}^T \mathbf{C} \boldsymbol{\varepsilon} d\Omega, \quad (4.10)$$

where $\boldsymbol{\sigma}$, $\boldsymbol{\varepsilon}$, and \boldsymbol{C} are the stress, strain, and stiffness tensor, respectively. Considering the local strain tensor obtained in Eq. (2.17) and constitutive relation for linear elastic materials in plane stress state, thus, the strain energy at the subvolume level can be evaluated as

$$U^{(q)} = \int_{-\frac{h_q}{2}}^{\frac{h_q}{2}} \int_{-\frac{l_q}{2}}^{\frac{l_q}{2}} \frac{1}{2} \boldsymbol{\varepsilon}^{(q)T} \boldsymbol{C}^{(q)} \boldsymbol{\varepsilon}^{(q)} dx_1^{(q)} dx_2^{(q)}. \quad (4.11)$$

As the unknown coefficients of the displacement field are independents from the local coordinate system $x_1^{(q)}$ and $x_2^{(q)}$, the local strain energy can be expressed as

$$U^{(q)} = \frac{1}{2} \left(\boldsymbol{W}^{(q)} \boldsymbol{D}_{00}^{(q)} \boldsymbol{W}^{(q)} + \boldsymbol{W}^{(q)} \boldsymbol{D}_{01}^{(q)} \boldsymbol{W}_{\nabla}^{(q)} + \boldsymbol{W}_{\nabla}^{(q)} \boldsymbol{D}_{10}^{(q)} \boldsymbol{W}^{(q)} + \boldsymbol{W}_{\nabla}^{(q)} \boldsymbol{D}_{11}^{(q)} \boldsymbol{W}_{\nabla}^{(q)} + \boldsymbol{W}_{\nabla^2}^{(q)} \boldsymbol{D}_{22}^{(q)} \boldsymbol{W}_{\nabla^2}^{(q)} \right), \quad (4.12)$$

where $\boldsymbol{D}_{mn}^{(q)} = \int_{-\frac{h_q}{2}}^{\frac{h_q}{2}} \int_{-\frac{l_q}{2}}^{\frac{l_q}{2}} \frac{1}{2} \boldsymbol{E}_m^{(q)T} \boldsymbol{C}^{(q)} \boldsymbol{E}_n^{(q)} dx_1^{(q)} dx_2^{(q)}$ and $\boldsymbol{D}_{02}^{(q)}$, $\boldsymbol{D}_{12}^{(q)}$, $\boldsymbol{D}_{20}^{(q)}$, and $\boldsymbol{D}_{21}^{(q)}$ are found to be null matrices. The non-zero matrices $\boldsymbol{D}_{mn}^{(q)}$ are shown in the Appendix B.

Thus, the total strain energy of a deforming structure can be obtained by summing the individual contribution of each subvolume as follows

$$U = \iiint_{\Omega} \bar{U} d\Omega = \sum_{q=1}^{N_q} U^{(q)}. \quad (4.13)$$

The expression presented in Equation (4.12) is valid only for the second-order version of the generalized finite-volume theory. For the first-order version, the strain energy at the subvolume level can be obtained by making $\boldsymbol{W}_{\nabla^2}^{(q)} = \mathbf{0}$, and for the zeroth-order version, the strain energy at the subvolume level can be obtained by making $\boldsymbol{W}_{\nabla}^{(q)} = \mathbf{0}$ and $\boldsymbol{W}_{\nabla^2}^{(q)} = \mathbf{0}$.

4.2 External Work Evaluation by the Generalized Finite-Volume Theory

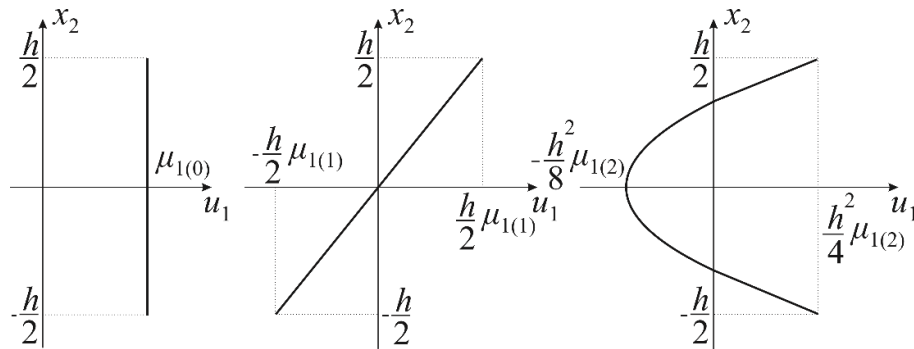
The displacement and traction distributions must be assumed polynomial along the faces for the generalized finite-volume theory; different displacement or traction distributions will not produce the equivalence between external work and strain energy, even for the zeroth-order version; only surface-averaged compatibilities and boundary conditions are imposed on the faces of the subvolumes. For the work done by external loading, the horizontal displacement on the vertical face of a subvolume can be approximated by three Legendre polynomials, as illustrated in Figure 10, and following the same features presented in Equation (2.1). Therefore, the horizontal displacement is written as

$$u_1^{(q)}(x_2^{(q)}) = \mu_{1(0)}^{(q)} + x_2^{(q)} \mu_{1(1)}^{(q)} + \frac{1}{2} \left(3x_2^{(q)2} - \frac{h_q^2}{4} \right) \mu_{1(2)}^{(q)}, \quad (4.14)$$

where $\mu_{1(m)}^{(q)}$ are the unknown coefficients of the horizontal displacement on a vertical face. Additionally, the counterclockwise rotation and curvature associated with the vertical face are respectively given by

$$\begin{aligned} \theta_{12}^{(q)}(x_2^{(q)}) &= -\frac{du_1^{(q)}}{dx_2^{(q)}}(x_2^{(q)}) = -\mu_{1(1)}^{(q)} - 3x_2^{(q)} \mu_{1(2)}^{(q)} \\ \kappa_{12}^{(q)}(x_2^{(q)}) &= -\frac{d^2u_1^{(q)}}{dx_2^{2(q)}}(x_2^{(q)}) = -3\mu_{1(2)}^{(q)} \end{aligned} \quad (4.15)$$

Figure 10 – Legendre polynomials representation employed for the estimative of horizontal displacement in the subvolume vertical faces



Font: Araujo (2018).

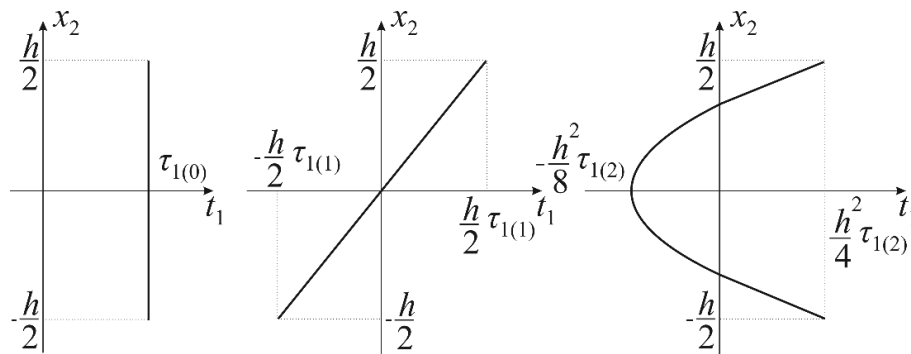
Similarly, the normal traction acting on a vertical face can be estimated by Legendre polynomials' superposition presented in Figure 11. Thus, the normal traction on a subvolume vertical face is estimated as

$$t_1^{(q)}(x_2^{(q)}) = \tau_{1(0)}^{(q)} + x_2^{(q)} \tau_{1(1)}^{(q)} + \frac{1}{2} \left(3x_2^{(q)2} - \frac{h_q^2}{4} \right) \tau_{1(2)}^{(q)}, \quad (4.16)$$

where $\tau_{1(m)}^{(q)}$ are unknown coefficients associated with the normal tractions acting on the vertical subvolume face. Therefore, the first and second normal traction derivatives can be respectively evaluated as

$$\begin{aligned} t_{1/2}^{(q)}(x_2^{(q)}) &= -\frac{dt_1^{(q)}}{dx_2^{(q)}}(x_2^{(q)}) = -\tau_{1(1)}^{(q)} - 3x_2^{(q)} \tau_{1(2)}^{(q)} \\ t_{1/22}^{(q)}(x_2^{(q)}) &= -\frac{d^2t_1^{(q)}}{dx_2^{2(q)}}(x_2^{(q)}) = -3\tau_{1(2)}^{(q)} \end{aligned} \quad (4.17)$$

Figure 11 – Legendre polynomials representation employed for estimative of normal tractions in the subvolume vertical faces



Font: Araujo (2018).

As a result, the surface-averaged kinematic and static quantities associated with the vertical faces of a generic subvolume q can be estimated as

$$\begin{aligned}
 \bar{u}_1^{(q)} &= \frac{1}{h_q} \int_{-\frac{h_q}{2}}^{\frac{h_q}{2}} u_1^{(q)}(x_2^{(q)}) dx_2^{(q)} = \mu_{1(0)}^{(q)} \\
 \bar{t}_1^{(q)} &= \frac{1}{h_q} \int_{-\frac{h_q}{2}}^{\frac{h_q}{2}} t_1^{(q)}(x_2^{(q)}) dx_2^{(q)} = \tau_{1(0)}^{(q)} \\
 \bar{\theta}_{12}^{(q)} &= \frac{1}{h_q} \int_{-\frac{h_q}{2}}^{\frac{h_q}{2}} \theta_{12}^{(q)}(x_2^{(q)}) dx_2^{(q)} = -\mu_{1(1)}^{(q)} \\
 \bar{t}_{1/2}^{(q)} &= \frac{1}{h_q} \int_{-\frac{h_q}{2}}^{\frac{h_q}{2}} t_{1/2}^{(q)}(x_2^{(q)}) dx_2^{(q)} = -\tau_{1(1)}^{(q)} \\
 \bar{\kappa}_{12}^{(q)} &= \frac{1}{h_q} \int_{-\frac{h_q}{2}}^{\frac{h_q}{2}} \kappa_{12}^{(q)}(x_2^{(q)}) dx_2^{(q)} = -3\mu_{1(2)}^{(q)} \\
 \bar{t}_{1/22}^{(q)} &= \frac{1}{h_q} \int_{-\frac{h_q}{2}}^{\frac{h_q}{2}} t_{1/22}^{(q)}(x_2^{(q)}) dx_2^{(q)} = -3\tau_{1(2)}^{(q)}
 \end{aligned} \tag{4.18}$$

Replacing Equation (4.18) in Equations (4.14) and (4.16), the following expressions can be respectively obtained

$$\begin{aligned}
 u_1^{(q)}(x_2^{(q)}) &= \bar{u}_1^{(q)} - x_2^{(q)} \bar{\theta}_{12}^{(q)} - \frac{1}{6} \left(3x_2^{(q)2} - \frac{h_q^2}{4} \right) \bar{\kappa}_{12}^{(q)} \\
 t_1^{(q)}(x_2^{(q)}) &= \bar{t}_1^{(q)} - x_2^{(q)} \bar{t}_{1/2}^{(q)} - \frac{1}{6} \left(3x_2^{(q)2} - \frac{h_q^2}{4} \right) \bar{t}_{1/22}^{(q)}
 \end{aligned} \tag{4.19}$$

From Equation (4.19), the resultant static quantities associated with the subvolume vertical face can be evaluated as

$$\begin{aligned}
R_1^{(q)} &= \int_{-\frac{h_q}{2}}^{\frac{h_q}{2}} t_1^{(q)}(x_2^{(q)}) dx_2^{(q)} = \bar{t}_1^{(q)} h_q \\
R_2^{(q)} &= \int_{-\frac{h_q}{2}}^{\frac{h_q}{2}} t_2^{(q)}(x_2^{(q)}) dx_2^{(q)} = \bar{t}_2^{(q)} h_q \\
M_R^{(q)} &= - \int_{-\frac{h_q}{2}}^{\frac{h_q}{2}} t_1^{(q)}(x_2^{(q)}) x_2^{(q)} dx_2^{(q)} = \bar{t}_{1/2}^{(q)} \frac{h_q^3}{12} \\
S_R^{(q)} &= \int_{-\frac{h_q}{2}}^{\frac{h_q}{2}} t_1^{(q)}(x_2^{(q)}) \frac{1}{6} \left(3x_2^{(q)2} - \frac{h_q^2}{4} \right) dx_2^{(q)} = \bar{t}_{1/22}^{(q)} \frac{h_q^5}{720}
\end{aligned} \tag{4.20}$$

where $R_i^{(q)}$ is the resultant force along the x_i direction acting on a subvolume vertical face, $M_R^{(q)}$ is the resultant bending moment acting on a subvolume vertical face and $S_R^{(q)}$ is the second-order bending moment acting on a subvolume vertical face. Thus, the work done on a subvolume vertical face can be evaluated as

$$\begin{aligned}
\tilde{W}^{(q)} &= \frac{1}{2} \int_{-\frac{h_q}{2}}^{\frac{h_q}{2}} t_1^{(q)}(x_2^{(q)}) u_1^{(q)}(x_2^{(q)}) dx_2^{(q)} = \frac{1}{2} \left(\bar{u}_1^{(q)} R_1^{(q)} + \bar{u}_2^{(q)} R_2^{(q)} + \right. \\
&\quad \left. \bar{\theta}_{12}^{(q)} M_R^{(q)} + \bar{\kappa}_{12}^{(q)} S_R^{(q)} \right).
\end{aligned} \tag{4.21}$$

By applying the same procedure to the other faces of the same subvolume, the following equation can be obtained

$$W^{(q)} = \frac{1}{2} \left(\mathbf{R}^{(q)} \bar{\mathbf{u}}^{(q)} + \mathbf{M}_R^{(q)} \bar{\boldsymbol{\theta}}^{(q)} + \mathbf{S}_R^{(q)} \bar{\boldsymbol{\kappa}}^{(q)} \right), \tag{4.22}$$

where $\mathbf{R}^{(q)}$ is the local resultant force vector, $\mathbf{M}_R^{(q)}$ is the local resultant bending moment vector and $\mathbf{S}_R^{(q)}$ is the local resultant second-order bending moment vector acting on the faces of a generic subvolume q . The global work done by external forces can be obtained by summing the individual contribution of each subvolume, thus,

$$W = \sum_{q=1}^{N_q} W^{(q)}. \tag{4.23}$$

The work done on the subvolume q , presented in Equation (4.22), is valid for the second-order version of the generalized finite-volume theory. For the first-order version, this expression can be updated by uncoupling the surface-averaged curvatures, and for the zeroth-order version, besides the curvatures, the surface-averaged rotations must also be uncoupled.

4.3 Sensitivity Analysis for the Compliance Function by the Generalized Finite-Volume Theory

For the OC method implementation, it is necessary to compute the objective's function gradient, which can be defined as twice the external work done or total strain energy. As a result, its sensitivity can be defined by considering a modified local system of equations:

$$\begin{bmatrix} \mathbf{R}^{(q)} \\ \mathbf{M}_R^{(q)} \\ \mathbf{S}_R^{(q)} \end{bmatrix} = \begin{bmatrix} \hat{\mathbf{L}}_{(0)}^{(q)} & \mathbf{0} & \mathbf{0} \\ \mathbf{0} & \hat{\mathbf{L}}_{(1)}^{(q)} & \mathbf{0} \\ \mathbf{0} & \mathbf{0} & \hat{\mathbf{L}}_{(2)}^{(q)} \end{bmatrix} \begin{bmatrix} \bar{\mathbf{t}}^{(q)} \\ \bar{\mathbf{t}}_{\nabla}^{(q)} \\ \bar{\mathbf{t}}_{\nabla^2}^{(q)} \end{bmatrix} = \hat{\mathbf{K}}^{(q)} \begin{bmatrix} \bar{\mathbf{u}}^{(q)} \\ \bar{\boldsymbol{\theta}}^{(q)} \\ \bar{\mathbf{k}}^{(q)} \end{bmatrix}, \quad (4.24)$$

where $\hat{\mathbf{K}}^{(q)} = \begin{bmatrix} \hat{\mathbf{L}}_{(0)}^{(q)} & \mathbf{0} & \mathbf{0} \\ \mathbf{0} & \hat{\mathbf{L}}_{(1)}^{(q)} & \mathbf{0} \\ \mathbf{0} & \mathbf{0} & \hat{\mathbf{L}}_{(2)}^{(q)} \end{bmatrix} \mathbf{K}_{(16 \times 16)}^{(q)}$ is the modified local stiffness matrix, and $\hat{\mathbf{L}}_{(i)}^{(q)}$ are

matrices that depend on the subvolume geometric features, which can be written as follows

$$\begin{aligned} \hat{\mathbf{L}}_{(0)}^{(q)} &= \begin{bmatrix} \hat{\mathbf{L}}_{(0)}^{(q,1)} & \mathbf{0} & \mathbf{0} & \mathbf{0} \\ \mathbf{0} & \hat{\mathbf{L}}_{(0)}^{(q,2)} & \mathbf{0} & \mathbf{0} \\ \mathbf{0} & \mathbf{0} & \hat{\mathbf{L}}_{(0)}^{(q,3)} & \mathbf{0} \\ \mathbf{0} & \mathbf{0} & \mathbf{0} & \hat{\mathbf{L}}_{(0)}^{(q,4)} \end{bmatrix} \text{ for } \hat{\mathbf{L}}_{(0)}^{(q,p)} = \begin{bmatrix} L_p^{(q)} & 0 \\ 0 & L_p^{(q)} \end{bmatrix}, \\ \hat{\mathbf{L}}_{(1)}^{(q)} &= \begin{bmatrix} \hat{\mathbf{L}}_{(1)}^{(q,1)} & 0 & 0 & 0 \\ 0 & \hat{\mathbf{L}}_{(1)}^{(q,2)} & 0 & 0 \\ 0 & 0 & \hat{\mathbf{L}}_{(1)}^{(q,3)} & 0 \\ 0 & 0 & 0 & \hat{\mathbf{L}}_{(1)}^{(q,4)} \end{bmatrix} \text{ for } \hat{\mathbf{L}}_{(1)}^{(q,p)} = (L_p^{(q)})^3 / 12, \\ \hat{\mathbf{L}}_{(2)}^{(q)} &= \begin{bmatrix} \hat{\mathbf{L}}_{(2)}^{(q,1)} & 0 & 0 & 0 \\ 0 & \hat{\mathbf{L}}_{(2)}^{(q,2)} & 0 & 0 \\ 0 & 0 & \hat{\mathbf{L}}_{(2)}^{(q,3)} & 0 \\ 0 & 0 & 0 & \hat{\mathbf{L}}_{(2)}^{(q,4)} \end{bmatrix} \text{ for } \hat{\mathbf{L}}_{(2)}^{(q,p)} = (L_p^{(q)})^5 / 720. \end{aligned} \quad (4.25)$$

Thereafter, the modified global system of equations can be established as

$$\begin{bmatrix} \mathbf{R} \\ \mathbf{M}_R \\ \mathbf{S}_R \end{bmatrix} = \hat{\mathbf{K}} \begin{bmatrix} \bar{\mathbf{u}} \\ \bar{\boldsymbol{\theta}} \\ \bar{\mathbf{k}} \end{bmatrix}, \quad (4.26)$$

where \mathbf{R} is the global resultant force vector, \mathbf{M}_R is the global resultant bending moment vector, \mathbf{S}_R is the global resultant second-order bending moment vector acting on the

subvolume faces, and $\hat{\mathbf{K}} = \sum_{q=1}^{N_q} \mathbf{L}^{(q)T} \hat{\mathbf{K}}^{(q)} \mathbf{L}^{(q)}$ is the modified global stiffness matrix. Therefore, the compliance function for the proposed topology optimization problem can be established as

$$C(\boldsymbol{\rho}) = \sum_{q=1}^{N_q} \begin{bmatrix} \mathbf{R}^{(q)} \\ \mathbf{M}_R^{(q)} \\ \mathbf{S}_R^{(q)} \end{bmatrix}^T \begin{bmatrix} \bar{\mathbf{u}}^{(q)} \\ \bar{\boldsymbol{\theta}}^{(q)} \\ \bar{\mathbf{k}}^{(q)} \end{bmatrix} = \sum_{q=1}^{N_q} \begin{bmatrix} \bar{\mathbf{u}}^{(q)} \\ \bar{\boldsymbol{\theta}}^{(q)} \\ \bar{\mathbf{k}}^{(q)} \end{bmatrix}^T \hat{\mathbf{K}}^{(q)T} \begin{bmatrix} \bar{\mathbf{u}}^{(q)} \\ \bar{\boldsymbol{\theta}}^{(q)} \\ \bar{\mathbf{k}}^{(q)} \end{bmatrix}. \quad (4.27)$$

Employing the chain rule, the objective's function gradient can be determined by

$$\frac{\partial C(\boldsymbol{\rho})}{\partial \rho_r} = \sum_{q=1}^{N_q} \left(\frac{\partial}{\partial \rho_r} \left(\begin{bmatrix} \bar{\mathbf{u}}^{(q)} \\ \bar{\boldsymbol{\theta}}^{(q)} \\ \bar{\mathbf{k}}^{(q)} \end{bmatrix}^T \hat{\mathbf{K}}^{(q)T} \right) \begin{bmatrix} \bar{\mathbf{u}}^{(q)} \\ \bar{\boldsymbol{\theta}}^{(q)} \\ \bar{\mathbf{k}}^{(q)} \end{bmatrix} + \begin{bmatrix} \bar{\mathbf{u}}^{(q)} \\ \bar{\boldsymbol{\theta}}^{(q)} \\ \bar{\mathbf{k}}^{(q)} \end{bmatrix}^T \hat{\mathbf{K}}^{(q)T} \frac{\partial}{\partial \rho_r} \begin{bmatrix} \bar{\mathbf{u}}^{(q)} \\ \bar{\boldsymbol{\theta}}^{(q)} \\ \bar{\mathbf{k}}^{(q)} \end{bmatrix} \right). \quad (4.28)$$

Equation (4.28) can be written as

$$\begin{aligned} \frac{\partial C(\boldsymbol{\rho})}{\partial \rho_r} &= \begin{bmatrix} \bar{\mathbf{u}}^{(r)} \\ \bar{\boldsymbol{\theta}}^{(r)} \\ \bar{\mathbf{k}}^{(r)} \end{bmatrix}^T \frac{\partial \hat{\mathbf{K}}^{(r)T}}{\partial \rho_r} \begin{bmatrix} \bar{\mathbf{u}}^{(r)} \\ \bar{\boldsymbol{\theta}}^{(r)} \\ \bar{\mathbf{k}}^{(r)} \end{bmatrix} + \frac{\partial}{\partial \rho_r} \begin{bmatrix} \bar{\mathbf{u}} \\ \bar{\boldsymbol{\theta}} \\ \bar{\mathbf{k}} \end{bmatrix}^T \sum_{q=1}^{N_q} \left[\mathbf{L}^{(q)T} \hat{\mathbf{K}}^{(q)T} \mathbf{L}^{(q)} \right] \begin{bmatrix} \bar{\mathbf{u}} \\ \bar{\boldsymbol{\theta}} \\ \bar{\mathbf{k}} \end{bmatrix} + \\ &\begin{bmatrix} \bar{\mathbf{u}} \\ \bar{\boldsymbol{\theta}} \\ \bar{\mathbf{k}} \end{bmatrix}^T \sum_{q=1}^{N_q} \left[\mathbf{L}^{(q)T} \hat{\mathbf{K}}^{(q)T} \mathbf{L}^{(q)} \right] \frac{\partial}{\partial \rho_r} \begin{bmatrix} \bar{\mathbf{u}} \\ \bar{\boldsymbol{\theta}} \\ \bar{\mathbf{k}} \end{bmatrix}. \end{aligned} \quad (4.29)$$

Considering $\hat{\mathbf{K}}^T = \sum_{q=1}^{N_q} \mathbf{L}^{(q)T} \hat{\mathbf{K}}^{(q)T} \mathbf{L}^{(q)}$, it follows:

$$\frac{\partial C(\boldsymbol{\rho})}{\partial \rho_r} = \begin{bmatrix} \bar{\mathbf{u}}^{(r)} \\ \bar{\boldsymbol{\theta}}^{(r)} \\ \bar{\mathbf{k}}^{(r)} \end{bmatrix}^T \frac{\partial \hat{\mathbf{K}}^{(r)T}}{\partial \rho_r} \begin{bmatrix} \bar{\mathbf{u}}^{(r)} \\ \bar{\boldsymbol{\theta}}^{(r)} \\ \bar{\mathbf{k}}^{(r)} \end{bmatrix} + \frac{\partial}{\partial \rho_r} \begin{bmatrix} \bar{\mathbf{u}} \\ \bar{\boldsymbol{\theta}} \\ \bar{\mathbf{k}} \end{bmatrix}^T \hat{\mathbf{K}}^T \begin{bmatrix} \bar{\mathbf{u}} \\ \bar{\boldsymbol{\theta}} \\ \bar{\mathbf{k}} \end{bmatrix} + \begin{bmatrix} \bar{\mathbf{u}} \\ \bar{\boldsymbol{\theta}} \\ \bar{\mathbf{k}} \end{bmatrix}^T \hat{\mathbf{K}}^T \frac{\partial}{\partial \rho_r} \begin{bmatrix} \bar{\mathbf{u}} \\ \bar{\boldsymbol{\theta}} \\ \bar{\mathbf{k}} \end{bmatrix}. \quad (4.30)$$

Differentiating Equation (4.26) in relation to ρ_r , it follows:

$$\mathbf{0} = \mathbf{L}^{(r)T} \frac{\partial \hat{\mathbf{K}}^{(r)}}{\partial \rho_r} \mathbf{L}^{(r)} \begin{bmatrix} \bar{\mathbf{u}} \\ \bar{\boldsymbol{\theta}} \\ \bar{\mathbf{k}} \end{bmatrix} + \hat{\mathbf{K}} \frac{\partial}{\partial \rho_r} \begin{bmatrix} \bar{\mathbf{u}} \\ \bar{\boldsymbol{\theta}} \\ \bar{\mathbf{k}} \end{bmatrix}, \quad (4.31)$$

by simplifying, the following sentence can be obtained:

$$\frac{\partial}{\partial \rho_r} \begin{bmatrix} \bar{\mathbf{u}} \\ \bar{\boldsymbol{\theta}} \\ \bar{\mathbf{k}} \end{bmatrix}^T \hat{\mathbf{K}}^T = - \begin{bmatrix} \bar{\mathbf{u}}^{(r)} \\ \bar{\boldsymbol{\theta}}^{(r)} \\ \bar{\mathbf{k}}^{(r)} \end{bmatrix}^T \frac{\partial \hat{\mathbf{K}}^{(r)T}}{\partial \rho_r} \mathbf{L}^{(r)} \quad (4.32)$$

once $\begin{bmatrix} \bar{\mathbf{u}}^{(r)} \\ \bar{\boldsymbol{\theta}}^{(r)} \\ \bar{\mathbf{k}}^{(r)} \end{bmatrix}^T = \mathbf{L}^{(r)} \begin{bmatrix} \bar{\mathbf{u}} \\ \bar{\boldsymbol{\theta}} \\ \bar{\mathbf{k}} \end{bmatrix}$ from kinematic incidence of each subvolume in the global kinematic

vector. Substituting Equation (4.32) in Equation (4.30), we have

$$\frac{\partial C(\boldsymbol{\rho})}{\partial \rho_r} = \begin{bmatrix} \bar{\mathbf{u}}^{(r)} \\ \bar{\boldsymbol{\theta}}^{(r)} \\ \bar{\mathbf{k}}^{(r)} \end{bmatrix}^T \frac{\partial \hat{\mathbf{K}}^{(r)T}}{\partial \rho_r} \begin{bmatrix} \bar{\mathbf{u}}^{(r)} \\ \bar{\boldsymbol{\theta}}^{(r)} \\ \bar{\mathbf{k}}^{(r)} \end{bmatrix} - \begin{bmatrix} \bar{\mathbf{u}}^{(r)} \\ \bar{\boldsymbol{\theta}}^{(r)} \\ \bar{\mathbf{k}}^{(r)} \end{bmatrix}^T \frac{\partial \hat{\mathbf{K}}^{(r)T}}{\partial \rho_r} \mathbf{L}^{(r)} \begin{bmatrix} \bar{\mathbf{u}} \\ \bar{\boldsymbol{\theta}} \\ \bar{\mathbf{k}} \end{bmatrix} + \begin{bmatrix} \bar{\mathbf{u}} \\ \bar{\boldsymbol{\theta}} \\ \bar{\mathbf{k}} \end{bmatrix}^T \hat{\mathbf{K}}^T \frac{\partial}{\partial \rho_r} \begin{bmatrix} \bar{\mathbf{u}} \\ \bar{\boldsymbol{\theta}} \\ \bar{\mathbf{k}} \end{bmatrix}, \quad (4.33)$$

which can be simplified to

$$\frac{\partial C(\boldsymbol{\rho})}{\partial \rho_r} = \begin{bmatrix} \bar{\mathbf{u}} \\ \bar{\boldsymbol{\theta}} \\ \bar{\mathbf{k}} \end{bmatrix}^T \hat{\mathbf{K}}^T \frac{\partial}{\partial \rho_r} \begin{bmatrix} \bar{\mathbf{u}} \\ \bar{\boldsymbol{\theta}} \\ \bar{\mathbf{k}} \end{bmatrix}. \quad (4.34)$$

The compliance function can be also written as

$$C(\boldsymbol{\rho}) = \sum_{q=1}^{N_q} \begin{bmatrix} \bar{\mathbf{u}}^{(q)} \\ \bar{\boldsymbol{\theta}}^{(q)} \\ \bar{\mathbf{k}}^{(q)} \end{bmatrix}^T \hat{\mathbf{K}}^{(q)T} \begin{bmatrix} \bar{\mathbf{u}}^{(q)} \\ \bar{\boldsymbol{\theta}}^{(q)} \\ \bar{\mathbf{k}}^{(q)} \end{bmatrix} = \begin{bmatrix} \bar{\mathbf{u}} \\ \bar{\boldsymbol{\theta}} \\ \bar{\mathbf{k}} \end{bmatrix}^T \hat{\mathbf{K}}^T \begin{bmatrix} \bar{\mathbf{u}} \\ \bar{\boldsymbol{\theta}} \\ \bar{\mathbf{k}} \end{bmatrix} = \begin{bmatrix} \mathbf{R} \\ \mathbf{M}_R \\ \mathbf{S}_R \end{bmatrix}^T \begin{bmatrix} \bar{\mathbf{u}} \\ \bar{\boldsymbol{\theta}} \\ \bar{\mathbf{k}} \end{bmatrix}, \quad (4.35)$$

which provides the following relation

$$C(\boldsymbol{\rho}) = \begin{bmatrix} \bar{\mathbf{u}} \\ \bar{\boldsymbol{\theta}} \\ \bar{\mathbf{k}} \end{bmatrix}^T \begin{bmatrix} \mathbf{R} \\ \mathbf{M}_R \\ \mathbf{S}_R \end{bmatrix} = \begin{bmatrix} \bar{\mathbf{u}} \\ \bar{\boldsymbol{\theta}} \\ \bar{\mathbf{k}} \end{bmatrix}^T \hat{\mathbf{K}} \begin{bmatrix} \bar{\mathbf{u}} \\ \bar{\boldsymbol{\theta}} \\ \bar{\mathbf{k}} \end{bmatrix} \therefore \begin{bmatrix} \mathbf{R} \\ \mathbf{M}_R \\ \mathbf{S}_R \end{bmatrix}^T = \begin{bmatrix} \bar{\mathbf{u}} \\ \bar{\boldsymbol{\theta}} \\ \bar{\mathbf{k}} \end{bmatrix}^T \hat{\mathbf{K}}^T = \begin{bmatrix} \bar{\mathbf{u}} \\ \bar{\boldsymbol{\theta}} \\ \bar{\mathbf{k}} \end{bmatrix}^T \hat{\mathbf{K}}. \quad (4.36)$$

Substituting Equation (4.36) in Equation (4.34), we have

$$\frac{\partial C(\boldsymbol{\rho})}{\partial \rho_r} = \begin{bmatrix} \bar{\mathbf{u}} \\ \bar{\boldsymbol{\theta}} \\ \bar{\mathbf{k}} \end{bmatrix}^T \hat{\mathbf{K}} \frac{\partial}{\partial \rho_r} \begin{bmatrix} \bar{\mathbf{u}} \\ \bar{\boldsymbol{\theta}} \\ \bar{\mathbf{k}} \end{bmatrix}. \quad (4.37)$$

Substituting the transpose of Equation (4.32) in Equation (4.37), we have

$$\begin{aligned} \frac{\partial C(\boldsymbol{\rho})}{\partial \rho_r} &= - \begin{bmatrix} \bar{\mathbf{u}} \\ \bar{\boldsymbol{\theta}} \\ \bar{\mathbf{k}} \end{bmatrix}^T \mathbf{L}^{(r)T} \frac{\partial \hat{\mathbf{K}}^{(r)}}{\partial \rho_r} \begin{bmatrix} \bar{\mathbf{u}}^{(r)} \\ \bar{\boldsymbol{\theta}}^{(r)} \\ \bar{\mathbf{k}}^{(r)} \end{bmatrix} = - \begin{bmatrix} \bar{\mathbf{u}}^{(r)} \\ \bar{\boldsymbol{\theta}}^{(r)} \\ \bar{\mathbf{k}}^{(r)} \end{bmatrix}^T \frac{\partial \hat{\mathbf{K}}^{(r)}}{\partial \rho_r} \begin{bmatrix} \bar{\mathbf{u}}^{(r)} \\ \bar{\boldsymbol{\theta}}^{(r)} \\ \bar{\mathbf{k}}^{(r)} \end{bmatrix} = \\ &= -p\rho_r^{p-1} \begin{bmatrix} \bar{\mathbf{u}}^{(r)} \\ \bar{\boldsymbol{\theta}}^{(r)} \\ \bar{\mathbf{k}}^{(r)} \end{bmatrix}^T \hat{\mathbf{K}}^{(r)}(1) \begin{bmatrix} \bar{\mathbf{u}}^{(r)} \\ \bar{\boldsymbol{\theta}}^{(r)} \\ \bar{\mathbf{k}}^{(r)} \end{bmatrix}, \end{aligned} \quad (4.38)$$

where $\hat{\mathbf{K}}^{(r)}(1)$ is modified local stiffness matrix considering a unitary relative density and p represents the penalty factor. Thus, Equation (4.38) can be simplified to

$$\frac{\partial C(\boldsymbol{\rho})}{\partial \rho_r} = -p\rho_r^{p-1} \begin{bmatrix} \mathbf{R}^{(r)} \\ \mathbf{M}_R^{(r)} \\ \mathbf{S}_R^{(r)} \end{bmatrix}^T \begin{bmatrix} \bar{\mathbf{u}}^{(r)} \\ \bar{\boldsymbol{\theta}}^{(r)} \\ \bar{\mathbf{k}}^{(r)} \end{bmatrix} = -2p\rho_r^{p-1} W^{(r)} \approx -2p\rho_r^{p-1} U^{(r)}, \quad (4.39)$$

where $W^{(r)}$ is the external work done in the subvolume r , computed as described in Equation (4.22), and $U^{(r)}$ is the local strain energy in the subvolume r , computed as presented in Equation (4.12). As previously discussed, the approximation in Equation (4.39) emerges from

the fact that the external work done and total strain energy in a quasi-static analysis of structures are approximately equivalent for the higher-order versions of the generalized finite-volume theory, especially when a not sufficiently fine is employed. The presented formulation corresponds to the objective's function gradient for the second-order version of the generalized finite-volume theory. Therefore, the gradient for the first-order version of the theory can be obtained by uncoupling the curvatures in the presented formulation, and for zeroth-order version in addition to the curvatures, the rotations must be uncoupled.

4.4 Compliance Function and Sensitivity for Elastoplastic Analysis based on the Standard Finite-Volume Theory

Although a structural material is often modeled considering only its elastic properties, the consideration of the plastic material behavior when the acting stress is over the material yield stress can produce more realistic optimized topologies. Figure 12 shows the interpretation of the strain energy minimization problem considering linear elastic and elastoplastic structures. Therefore, to ensure that the load reaches the prescribed value of \mathbf{P} , it can be assumed an elastoplastic behavior with linear hardening for the structural material, assuming a determined value for the hardening parameter H_p . In this case, θ_2 represents the mean slope of the curve of load versus displacement when the structure is out of the elastic regime. On the other hand, assuming a perfectly plastic elastic behavior, there is no guarantee that the applied load reaches the predefined value of \mathbf{P} .

Following the previous sensitivity deductions, the modified local tangent stiffness matrix can be defined as

$$\Delta \mathbf{R}_k^{(q)} = \hat{\mathbf{L}}_{(0)}^{(q)} \Delta \bar{\mathbf{t}}_k^{(q)} = \hat{\mathbf{K}}_k^{(q)} \Delta \bar{\mathbf{u}}_k^{(q)}, \quad (4.40)$$

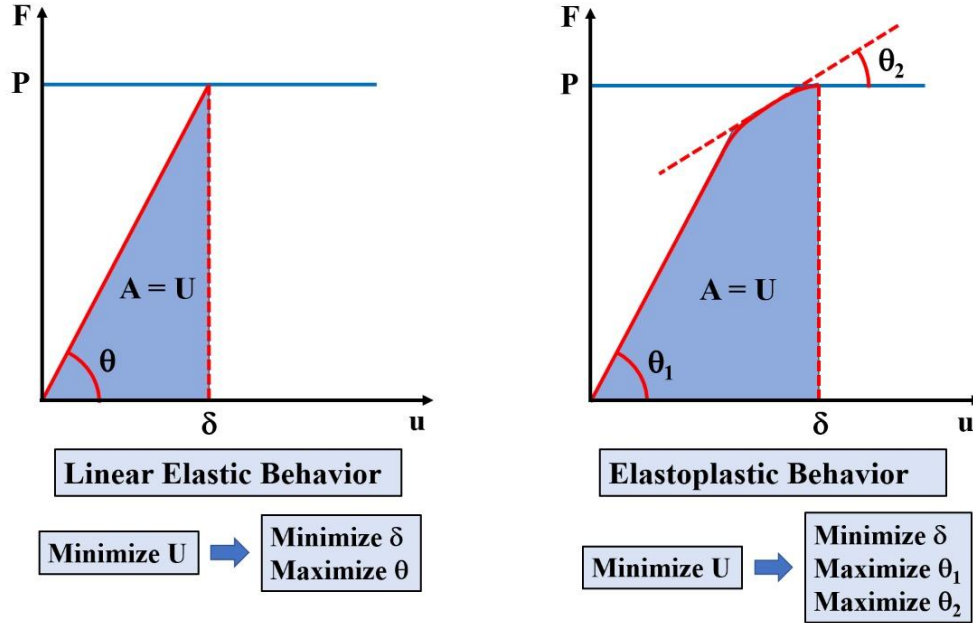
$$\text{where } \hat{\mathbf{K}}_k^{(q)} = \hat{\mathbf{L}}_{(0)}^{(q)} \mathbf{K}_k^{(q)} \text{ and } \hat{\mathbf{L}}_{(0)}^{(q)} = \begin{bmatrix} \hat{\mathbf{L}}_{(0)}^{(q,1)} & \mathbf{0} & \mathbf{0} & \mathbf{0} \\ \mathbf{0} & \hat{\mathbf{L}}_{(0)}^{(q,2)} & \mathbf{0} & \mathbf{0} \\ \mathbf{0} & \mathbf{0} & \hat{\mathbf{L}}_{(0)}^{(q,3)} & \mathbf{0} \\ \mathbf{0} & \mathbf{0} & \mathbf{0} & \hat{\mathbf{L}}_{(0)}^{(q,4)} \end{bmatrix} \text{ for } \hat{\mathbf{L}}_{(0)}^{(q,p)} = \begin{bmatrix} L_p^{(q)} & 0 \\ 0 & L_p^{(q)} \end{bmatrix}.$$

Additionally, the modified global tangent stiffness matrix can be written as

$$\Delta \mathbf{R}_k = \hat{\mathbf{K}}_k \Delta \bar{\mathbf{u}}_k, \quad (4.41)$$

$$\text{where } \Delta \mathbf{R}_k = \sum_{q=1}^{N_q} \mathbf{L}^{(q)T} \Delta \mathbf{R}_k^{(q)} \text{ and } \hat{\mathbf{K}}_k = \sum_{q=1}^{N_q} \mathbf{L}^{(q)T} \hat{\mathbf{K}}_k^{(q)} \mathbf{L}^{(q)} \text{ for } \Delta \bar{\mathbf{u}}_k^{(q)} = \mathbf{L}^{(q)} \Delta \bar{\mathbf{u}}_k.$$

Figure 12 – Interpretation of the compliance minimization problem considering the linear elastic and elastoplastic behavior



Font: Author (2022).

From Figure 12, the total strain energy can be evaluated as the area above the graphic for the elastoplastic behavior, which can be assessed by the sum of each trapeze discretized along the displacement axis., as follows

$$U(\rho) = \sum_{q=1}^{N_q} \int_0^{\bar{u}^{(q)}} \mathbf{R}^{(q)T} (\bar{\mathbf{u}}'^{(q)}) d\bar{\mathbf{u}}'^{(q)} \cong \sum_{q=1}^{N_q} \sum_{k=2}^{N_k} \mathbf{R}_{k-1}^{(q)T} \Delta \bar{\mathbf{u}}_k^{(q)} + \frac{1}{2} \sum_{q=1}^{N_q} \sum_{k=1}^{N_k} \Delta \mathbf{R}_k^{(q)T} \Delta \bar{\mathbf{u}}_k^{(q)}, \quad (4.42)$$

which can be rewritten by

$$U(\rho) \cong \sum_{q=1}^{N_q} \sum_{k=2}^{N_k} \sum_{k'=1}^{k-1} \Delta \mathbf{R}_{k'}^{(q)T} \Delta \bar{\mathbf{u}}_k^{(q)} + \frac{1}{2} \sum_{q=1}^{N_q} \sum_{k=1}^{N_k} \Delta \bar{\mathbf{u}}_k^{(q)T} \hat{\mathbf{R}}_k^{(q)T} \Delta \bar{\mathbf{u}}_k^{(q)} = \sum_{q=1}^{N_q} \sum_{k=2}^{N_k} \sum_{k'=1}^{k-1} \Delta \bar{\mathbf{u}}_{k'}^{(q)T} \hat{\mathbf{R}}_{k'}^{(q)T} \Delta \bar{\mathbf{u}}_k^{(q)} + \frac{1}{2} \sum_{q=1}^{N_q} \sum_{k=1}^{N_k} \Delta \bar{\mathbf{u}}_k^{(q)T} \hat{\mathbf{R}}_k^{(q)T} \Delta \bar{\mathbf{u}}_k^{(q)}. \quad (4.43)$$

Considering the global system of equations assemblage, Eq. (4.43) is rewritten as

$$U(\rho) \cong \sum_{k=2}^{N_k} \sum_{k'=1}^{k-1} \Delta \bar{\mathbf{u}}_{k'}^T \sum_{q=1}^{N_q} \left(\mathbf{L}^{(q)T} \hat{\mathbf{R}}_{k'}^{(q)T} \mathbf{L}^{(q)} \right) \Delta \bar{\mathbf{u}}_k + \frac{1}{2} \sum_{k=1}^{N_k} \Delta \bar{\mathbf{u}}_k^T \sum_{q=1}^{N_q} \left(\mathbf{L}^{(q)T} \hat{\mathbf{R}}_k^{(q)T} \mathbf{L}^{(q)} \right) \Delta \bar{\mathbf{u}}_k = \sum_{k=2}^{N_k} \sum_{k'=1}^{k-1} \Delta \bar{\mathbf{u}}_{k'}^T \hat{\mathbf{R}}_{k'}^T \Delta \bar{\mathbf{u}}_k + \frac{1}{2} \sum_{k=1}^{N_k} \Delta \bar{\mathbf{u}}_k^T \hat{\mathbf{R}}_k^T \Delta \bar{\mathbf{u}}_k. \quad (4.44)$$

Assuming $\Delta \mathbf{R}_k^T \Delta \bar{\mathbf{u}}_k = \Delta \mathbf{R}_k^T \Delta \bar{\mathbf{u}}_k$ or $\Delta R_{i(k')} = \Delta R_{i(k)}$ for the free degrees of freedom and $\Delta \bar{\mathbf{u}}_{i(k)} = 0$ for the prescribed degrees of freedom, Eq. (4.44) can be updated to

$$U(\boldsymbol{\rho}) \cong \sum_{k=2}^{N_k} (k-1) \Delta \mathbf{R}_k^T \Delta \bar{\mathbf{u}}_k + \frac{1}{2} \sum_{k=1}^{N_k} \Delta \mathbf{R}_k^T \Delta \bar{\mathbf{u}}_k = \sum_{k=1}^{N_k} \left(k - \frac{1}{2}\right) \Delta \bar{\mathbf{u}}_k^T \hat{\mathbf{K}}_k^T \Delta \bar{\mathbf{u}}_k. \quad (4.45)$$

As $\Delta \mathbf{R}_k^T \Delta \bar{\mathbf{u}}_k = \Delta \bar{\mathbf{u}}_k^T \Delta \mathbf{R}_k$, the compliance function based on total strain energy can be estimated by

$$U(\boldsymbol{\rho}) \cong \sum_{k=1}^{N_k} \left(k - \frac{1}{2}\right) \Delta \bar{\mathbf{u}}_k^T \Delta \mathbf{R}_k = \sum_{k=1}^{N_k} \left(k - \frac{1}{2}\right) \Delta \bar{\mathbf{u}}_k^T \hat{\mathbf{K}}_k \Delta \bar{\mathbf{u}}_k. \quad (4.46)$$

Thereafter, the objective function's gradient is given by

$$\begin{aligned} \frac{\partial U(\boldsymbol{\rho})}{\partial \rho_r} &\cong \sum_{k=1}^{N_k} \left(k - \frac{1}{2}\right) \left[\frac{\partial}{\partial \rho_r} (\Delta \bar{\mathbf{u}}_k^T \hat{\mathbf{K}}_k) \Delta \bar{\mathbf{u}}_k + \Delta \bar{\mathbf{u}}_k^T \hat{\mathbf{K}}_k \frac{\partial \Delta \bar{\mathbf{u}}_k}{\partial \rho_r} \right] = \sum_{k=1}^{N_k} \left(k - \right. \\ &\left. \frac{1}{2}\right) \left(\frac{\partial \Delta \bar{\mathbf{u}}_k^T}{\partial \rho_r} \hat{\mathbf{K}}_k \Delta \bar{\mathbf{u}}_k + \Delta \bar{\mathbf{u}}_k^T \frac{\partial \hat{\mathbf{K}}_k}{\partial \rho_r} \Delta \bar{\mathbf{u}}_k + \Delta \bar{\mathbf{u}}_k^T \hat{\mathbf{K}}_k \frac{\partial \Delta \bar{\mathbf{u}}_k}{\partial \rho_r} \right). \end{aligned} \quad (4.47)$$

By differentiating $\Delta \mathbf{R}_k = \hat{\mathbf{K}}_k \Delta \bar{\mathbf{u}}_k$ in relation to ρ_r , follows

$$\mathbf{0} = \mathbf{L}^{(r)T} \frac{\partial \hat{\mathbf{K}}_k^{(r)}}{\partial \rho_r} \mathbf{L}^{(r)} \Delta \bar{\mathbf{u}}_k + \hat{\mathbf{K}}_k \frac{\partial \Delta \bar{\mathbf{u}}_k}{\partial \rho_r}, \quad (4.48)$$

which can lead to

$$\hat{\mathbf{K}}_k \frac{\partial \Delta \bar{\mathbf{u}}_k}{\partial \rho_r} = -\mathbf{L}^{(r)T} \frac{\partial \hat{\mathbf{K}}_k^{(r)}}{\partial \rho_r} \mathbf{L}^{(r)} \Delta \bar{\mathbf{u}}_k. \quad (4.49)$$

Thus, Eq. (4.47) can be rewritten as

$$\begin{aligned} \frac{\partial U(\boldsymbol{\rho})}{\partial \rho_r} &\cong \sum_{k=1}^{N_k} \left(k - \frac{1}{2}\right) \Delta \bar{\mathbf{u}}_k^{(r)T} \frac{\partial \hat{\mathbf{K}}_k^{(r)}}{\partial \rho_r} \Delta \bar{\mathbf{u}}_k^{(r)} - \sum_{k=1}^{N_k} \left(k - \frac{1}{2}\right) \Delta \bar{\mathbf{u}}_k^{(r)T} \frac{\partial \hat{\mathbf{K}}_k^{(r)}}{\partial \rho_r} \Delta \bar{\mathbf{u}}_k^{(r)} + \\ &\sum_{k=1}^{N_k} \left(k - \frac{1}{2}\right) \left(\Delta \bar{\mathbf{u}}_k^T \hat{\mathbf{K}}_k^T \frac{\partial \Delta \bar{\mathbf{u}}_k}{\partial \rho_r} \right), \end{aligned} \quad (4.50)$$

which can be simplified by

$$\frac{\partial U(\boldsymbol{\rho})}{\partial \rho_r} \cong \sum_{k=1}^{N_k} \left(k - \frac{1}{2}\right) \left(\Delta \bar{\mathbf{u}}_k^T \hat{\mathbf{K}}_k^T \frac{\partial \Delta \bar{\mathbf{u}}_k}{\partial \rho_r} \right). \quad (4.51)$$

Considering the following relation $\Delta \bar{\mathbf{u}}_k^T \hat{\mathbf{K}}_k^T = \Delta \bar{\mathbf{u}}_k^T \hat{\mathbf{K}}_k$, the topology optimization sensitivity can be evaluated as

$$\frac{\partial U(\boldsymbol{\rho})}{\partial \rho_r} \cong \sum_{k=1}^{N_k} \left(k - \frac{1}{2}\right) \left(\Delta \bar{\mathbf{u}}_k^T \hat{\mathbf{K}}_k \frac{\partial \Delta \bar{\mathbf{u}}_k}{\partial \rho_r} \right) = -\sum_{k=1}^{N_k} \left(k - \frac{1}{2}\right) \Delta \bar{\mathbf{u}}_k^{(r)T} \frac{\partial \hat{\mathbf{K}}_k^{(r)}}{\partial \rho_r} \Delta \bar{\mathbf{u}}_k^{(r)}. \quad (4.52)$$

5 NUMERICAL IMPLEMENTATIONS

5.1 Topology Optimization Algorithm

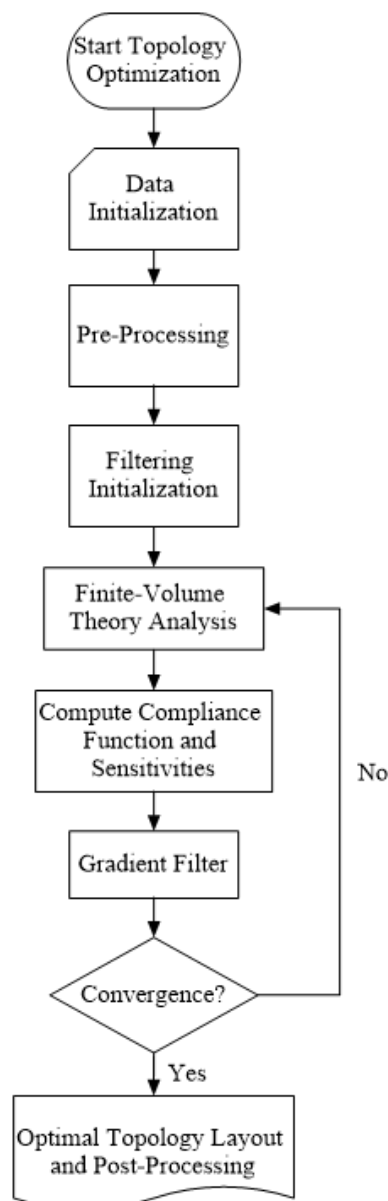
The employment of topology optimization algorithms to design efficient components for the industry is growing fast. Since the pioneering work of Bendsøe and Kikuchi (1988) in the homogenization method, several algorithms have been developed to design optimized components in structural analysis. Most of those algorithms employ a finite element-based strategy, which advantages and disadvantages are well-known. The topology optimization algorithm proposed in this contribution can solve compliance minimization problems based on the generalized finite-volume theory, where the relative density is considered constant in the subvolume, and the continued penalization scheme is adopted. Figure 13 presents a flowchart of the proposed algorithm implemented in MatLab language.

The algorithm is based on a two-step procedure: 1) data initialization and finite-volume theory analysis pre-processing, and 2) topology optimization looping. The proposed MatLab code is initialized by setting the material, geometric and topological properties, such as structure dimensions and discretization, prescribed loads, Young modulus, penalty factors, etc. Furthermore, the boundary value problem is also designated during the data initialization process in terms of essential and natural boundary conditions. The pre-processing step is characterized by mesh-generation, memory allocation for global static and kinematic vectors, insertion of prescribed forces and displacements, prescribing initial relative densities based on the prescribed volume fraction, plotting the initial structural topology, and calculation of the local stiffness matrix considering unitary relative densities. After that, the mesh-independent filter based on the gradient modification is then initialized by memory allocation and definition of the weight function quantities.

In the second algorithm part, the topology optimization procedure is performed, starting with the looping initialization, where the convergence criterium is established as 1% for the maximum change of relative densities between successive steps. The finite-volume theory analysis can be performed by the global stiffness matrix assemblage, which takes under consideration the constitutive relation proposed by the SIMP approach in Equation (3.2). For each step, the global system of equations, proposed in Equation (2.14), is solved, obtaining the surface-averaged kinematic variables used to compute the objective function and the subvolume sensitivities. After that, the gradient filter is called to regularize the topology optimization method by modifying the subvolume sensitivities as expressed in

Equations (3.6) and (3.7). Then, the design variables are updated by the OC method, as expressed in Equations (3.4) and (3.5). If the tolerance is fulfilled, the topology optimization algorithm assumes as converged, and the optimized topology is plotted. The post-processing consists of printing the algorithm performance information as the computational cost, the total number of iterations, the evolution of objective function along the optimization process, and the relative compliance calculated by considering the compliance of the Q8 finite-element result as the reference value.

Figure 13 – Flowchart of the topology optimization algorithm based on the finite-volume theory implemented in MatLab language



Font: Author (2022).

For the topology optimization algorithm in the absence of filtering technique, steps related to the gradient filter can be omitted, which permits the evaluation of the checkerboard-free property of the finite-volume theory and obtaining optimized topologies with thin bars for the Michell structure, as demonstrated by the analytical solution obtained by Michell (1904).

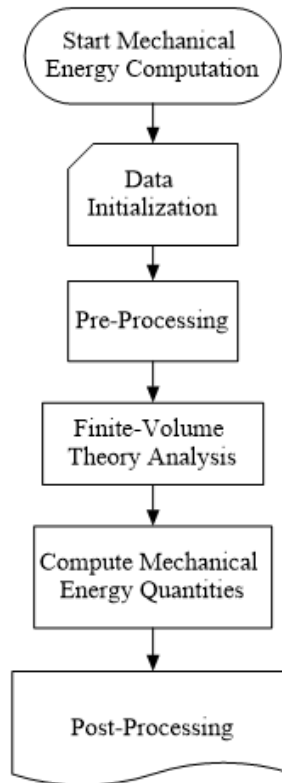
5.2 Energy Computation Algorithm for the Finite-Volume Theory

The second performed algorithm is implemented in MatLab language to compute mechanical energy by employing the generalized finite-volume theory. In this case, the mechanical energy can be computed as total strain energy in a deforming material or work done by external loading, used to verify the equivalence between those different mechanical energy calculations. The convergence to the response obtained by the analytical solution can be verified, checking if the mechanical energy presents a monotonic convergence with the mesh refinement. The flowchart of the algorithm performed to calculate the total strain energy or work done by external loading in a structure is illustrated in Figure 14.

Similarly, the proposed algorithm is divided into 1) data initialization and finite-volume theory analysis, and 2) mechanical energy estimations. The algorithm initially receives the data initialization composed of geometric and material parameters, the intensity of the applied loads, the number of horizontal and vertical subvolumes, and boundary conditions. The second step is to pre-process this data by performing mesh-generation, memory allocation for global force and displacement vectors, and insertion of prescribed displacements and forces. The next step refers to the finite-volume theory analysis, where the local stiffness matrix is obtained, and the global stiffness matrix is assembled. Then, the global system of equations is solved by obtaining the global surface-averaged kinematic vector, which is directly used to compute the structural strain energy, or the work done by external loading as defined in Equations (4.14) and (4.24).

The post-processing step consists of plotting the stress distribution and subvolume deformation, constructing graphs comparing the convergence of each approach, and error estimations based on the results obtained by analytical solutions. For the finite-element approaches, the discretization of the reference domain and the finite-volume theory analysis are substituted for mesh-generations, boundary conditions, and stress analyzes based on the assumptions of the finite-element method.

Figure 14 – Flowchart of the mechanical energy computation algorithm based on the finite-volume theory implemented in MatLab language



Font: Author (2022).

6 RESULTS AND DISCUSSIONS

6.1 Energy Evaluation for the Generalized Finite-Volume Theory

To verify the generalized finite-volume theory's mechanical energy properties, it is proposed to analyze two different examples. Numerical solutions based on the Q4 and Q8 elements of the finite element method and analytical solutions are provided as comparison and verification sources. Through these examples, the equivalence between the work done by external loading and total strain energy is verified for the zeroth order finite-volume theory. While the difference between those mechanical energy approaches has been also verified for the higher order versions of the generalized finite-volume theory. The plane stress state assumption was adopted for all the performed numerical analyzes. The employed computational environment, in terms of programming language and computer, can be described as MatLab R2016a (64-bits)/Intel® Core™ i7 CPU 2.93 GHz/16.0 GB RAM/64-bits. The codes were developed in-house to evaluate the global stiffness matrix and the global force vector for all the approaches, and the MatLab linear solver was employed to solve the global systems of equations.

6.1.1 Example 1: Cantilever beam

The first example considers a cantilever beam, whose domain of analysis and numerical boundary conditions are presented in Figure 15. The employed geometric parameters for this beam are taken as $h = 1$ m, $l = 4$ m, and $P = 1,000$ kN (resultant force of the parabolic distributed loading at the ends), while the adopted material properties are $E = 200$ GPa (elastic moduli) and $\nu = 0.32$ (Poisson's ratio). The analytical solution for this problem is well-known and can be found in Timoshenko and Goodier (1951), the expressions for the stress components are given by

$$\begin{aligned} \sigma_{11}(x_1, x_2) &= \frac{12P}{h^3} x_2 (l - x_1) \\ \sigma_{22}(x_1, x_2) &= 0 \\ \sigma_{12}(x_1, x_2) &= \frac{6P}{h^3} \left(x_2^2 - \frac{h^2}{4} \right) \end{aligned}, \quad (6.1)$$

and the strain components can be expressed as

$$\begin{aligned}
\varepsilon_{11}(x_1, x_2) &= -\frac{12Px_1x_2}{h^3E} \\
\varepsilon_{22}(x_1, x_2) &= \frac{12\nu Px_1x_2}{h^3E} \\
\varepsilon_{12}(x_1, x_2) &= \frac{12P(1+\nu)}{h^3E} \left(x_2^2 - \frac{h^2}{4} \right)
\end{aligned} \tag{6.2}$$

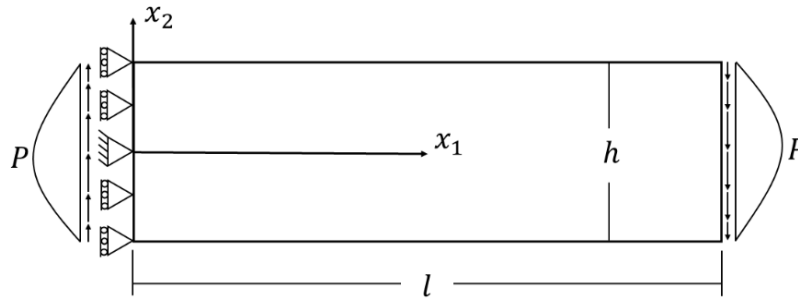
As a result, the total strain energy for the analytical solution can be computed as

$$\begin{aligned}
U &= \frac{1}{2} \int_0^l \int_{-\frac{h}{2}}^{\frac{h}{2}} (\sigma_{11}\varepsilon_{11} + \sigma_{22}\varepsilon_{22} + \sigma_{12}\varepsilon_{12}) dx_2 dx_1 = \frac{1}{2} \int_0^l \int_{-\frac{h}{2}}^{\frac{h}{2}} \left[\frac{12Px_1x_2^2}{h^6E} (x_1 - l) + \right. \\
&\left. \frac{72P(1+\nu)}{h^3E} \left(x_2^2 - \frac{h^2}{4} \right)^2 \right] dx_2 dx_1 = 671.68 \text{ J.}
\end{aligned} \tag{6.3}$$

The employed boundary conditions in the numerical approaches must reflect the boundary conditions considered in the analytical solution to ensure the correctness verification of the proposed formulations.

The finite-volume theory and finite element analysis are performed using the same discretizations with rectangular subvolumes or elements. As the work done by external loading and the total strain energy are equals for energy-based numerical approaches, only the work done by external loading is evaluated for the finite element analyzes.

Figure 15 – Cantilever beam



Font: Author (2022).

Table 01 presents the investigated numerical aspects for the total strain energy and the work done by external loading, employing the different numerical approaches based on the finite element method and finite-volume theory, and considering different mesh refinements. As expected, the total strain energy and the external work, employing the zeroth-order finite-volume theory (FVT^{0th}) approach, are similar for all evaluated meshes. At the same time, for the first and second-order versions of the generalized finite-volume theory (FVT^{1st} and FVT^{2nd}, respectively), there is a difference between the employed energy evaluation approaches. However, for the most refined mesh, this difference corresponds to

approximately 0.02%, for the higher-order versions of the generalized finite-volume theory. The Q8 element seems to converge to a slightly different solution relative to the analytical approach due to the boundary conditions' differences at the fixed end.

In terms of computational cost, the Q4 element approach is the fastest solution, followed by the zeroth-order finite-volume theory. On the other hand, the second-order finite-volume theory has presented the highest processing time, followed by the Q8 element approach and the first-order finite-volume theory, respectively. The number of degrees of freedom partially explains these differences in computational cost since it defines the size of the global system of equations.

The error is evaluated relative to the analytical solution as follows

$$\text{Error} = \frac{U|W_{\text{numerical}} - U_{\text{analytical}}}{U_{\text{analytical}}}, \quad (6.4)$$

where $U|W_{\text{numerical}}$ is the total strain energy or work done by external loading, depending on the studied approach, and $U_{\text{analytical}}$ corresponds to the total strain energy obtained for the analyzed structure employing the numerical integration of the strain energy density from the analytical solution.

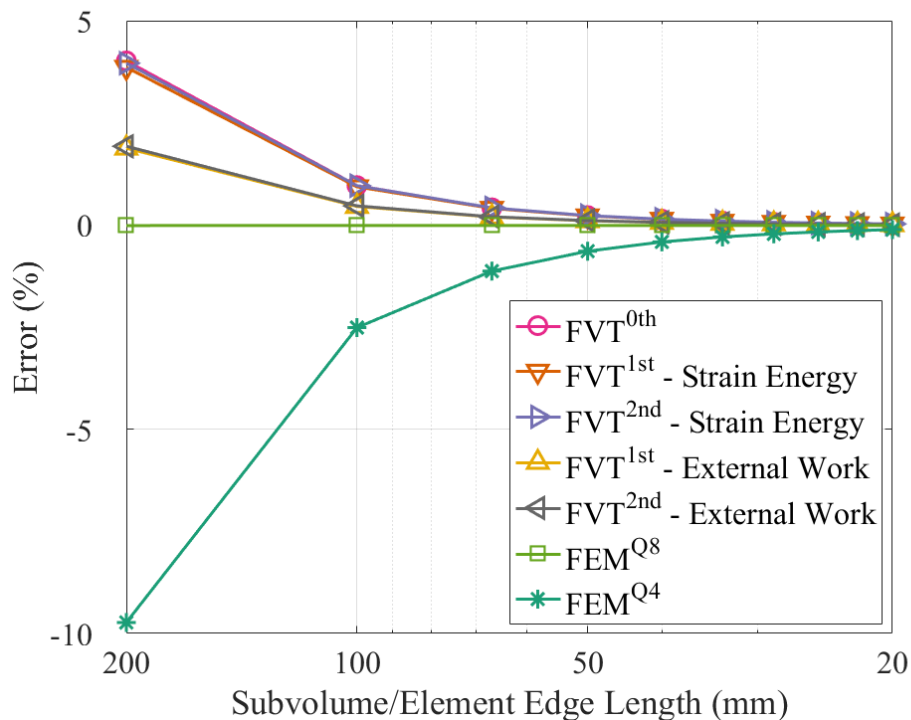
Table 01 – Mechanical energy analysis for the cantilever beam

Analysis	Mesh	ndof	Strain Energy			External Work		
			Processing Time (s)	Value (J)	Error (%)	Processing Time (s)	Value (J)	Error (%)
FVT ^{0th}	20x5	450	0.030	698.65	4.015	0.027	698.65	4.015
	100x25	10250	3.796	672.63	0.142	3.775	672.63	0.142
	200x50	40500	36.727	671.85	0.026	36.342	671.85	0.026
FVT ^{1st}	20x5	675	0.595	697.60	3.859	0.149	684.31	1.880
	100x25	15375	10.530	672.60	0.138	4.969	672.09	0.061
	200x50	60750	71.142	671.85	0.025	60.356	671.72	0.006
FVT ^{2nd}	20x5	900	0.211	698.28	3.960	0.121	684.63	1.927
	100x25	20500	7.892	672.64	0.142	6.301	672.11	0.064
	200x50	81000	86.946	671.85	0.026	85.096	671.72	0.006
Q4	20x5	252	-	-	-	0.035	606.32	-9.732
	100x25	5252	-	-	-	0.887	668.89	-0.416
	200x50	20502	-	-	-	14.019	670.92	-0.114
Q8	20x5	702	-	-	-	0.075	671.58	-0.015
	100x25	15502	-	-	-	6.400	671.59	-0.013
	200x50	61002	-	-	-	77.126	671.59	-0.013
Analytical	-	-	-	671.68	-	-	671.68	-

Font: Author (2022).

Figure 16 presents the overall convergence for the different evaluated approaches relative to the analytical solution. As expected, the Q8 element approach has presented the fastest convergence to the analytical result, while the Q4 element approach has presented the lowest convergence to the same result. For the higher-order versions of the generalized finite-volume theory, it is observed that the work done by external loading presents a faster convergence and tends to give a stiffer response to the analyzed structure in comparison to the total strain energy approach. As expected, the finite element method tends to present a stiffer response due to the displacement representation restrictions. Once the Q4 element has a poorer displacement representation relative to the Q8 element, this results in a stiffer response. In both cases, full numerical integration was adopted to evaluate the local stiffness matrices. Although the generalized finite-volume theory presents a more compliance response for this example, it does not have a defined trend as the finite element method once it is an equilibrium-based formulation.

Figure 16 – Convergence analysis for the cantilever beam

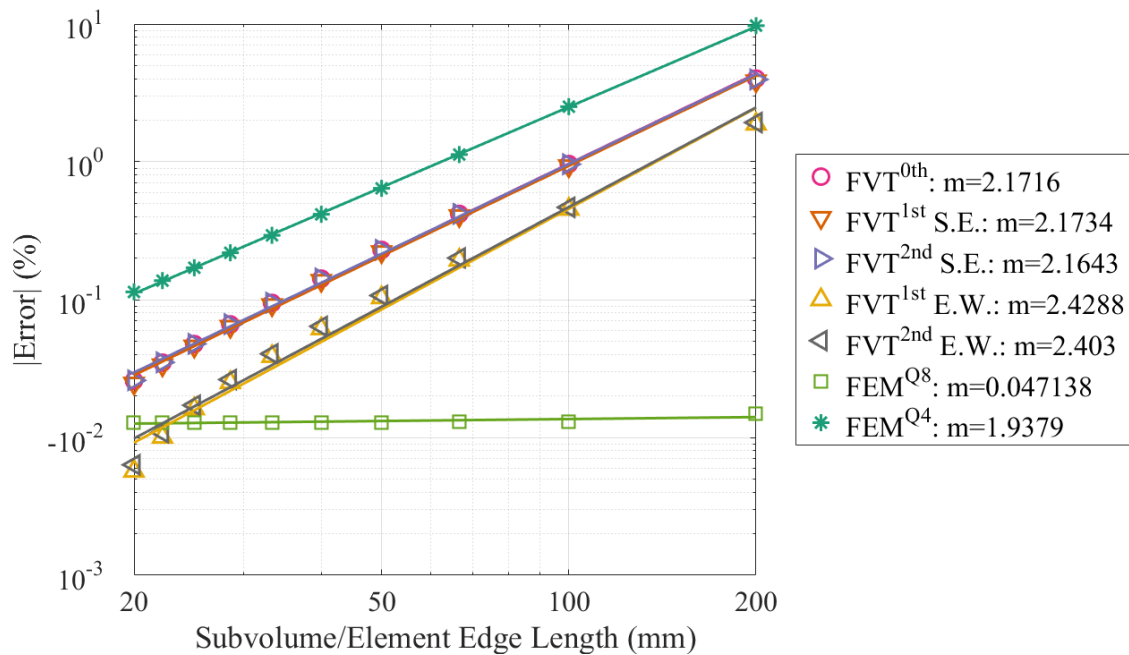


Font: Author (2022).

Figure 17 shows the convergence rate analysis for the evaluated approaches relative to the analytical solution, where m is the angular coefficient (slope) of the linear regression adjustments (least-squares method) for the log-log graph. The Q8 element approach has presented the lowest convergence rate once the result with the coarsest mesh already shows an

excellent agreement with the analytical solution due to the linear and quadratic variation of the normal and shear stress components for this problem. The Q4 element approach presents the worst convergence rate among the other techniques and the worst results for all the analyzed meshes. The finite-volume theory has presented higher convergence rates in comparison to the finite element method for this example. In general, the approach based on the External Work (E.W.) has obtained higher convergence rates relative to the same approach based on the Strain Energy (S.E.) for the first and second-order versions of the generalized finite-volume theory. Additionally, the above convergence rates are in line with the expected values for the angular coefficient for this problem, where they are expected to be from 1 to 2 for linear or quadratic numerical approaches. For the Q8 element, the agreement with the analytical solution is achieved when one element is employed in the vertical direction once cross coefficients appear in the stress field, which explains the low value obtained for the convergence rate.

Figure 17 – Convergence rate analysis for the cantilever beam



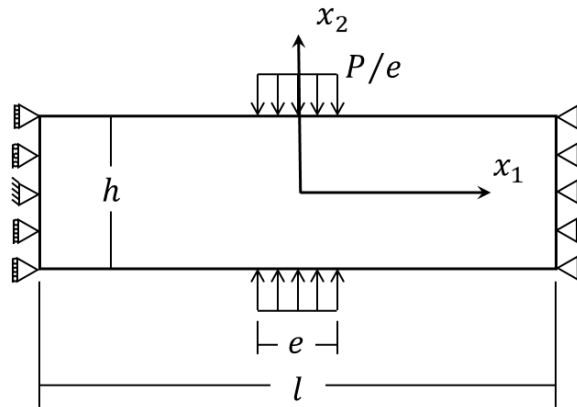
Font: Author (2022).

6.1.2 Example 2: Rectangular beam subjected to concentrated loads

The other proposed structural problem is a rectangular beam under concentrated loads at the top and bottom beam surfaces, intending to examine these approaches' behavior in a problem with stress concentration. The domain of analysis and numerical boundary conditions can be checked in Figure 18, where $h = 1$ m, $l = 3$ m, $e = 0.2$ m, $P = 1,000$ kN, $\nu = 0.33$

and $E = 68.9$ GPa. Analytical solutions for this problem can be found in Cavalcante and Pindera (2012b) and Timoshenko and Goodier (1951).

Figure 18 – Rectangular beam under concentrated and uniform normal tractions



Font: Author (2022).

A stress-based formulation can solve this problem, with the solution technique employing the Fourier transform. Considering the geometric and boundary conditions symmetries, the expressions for the stress components are given by

$$\begin{aligned}\sigma_{11}(x_1, x_2) &= \frac{2P}{\pi} \int_0^\infty \frac{2}{es} \sin\left(\frac{es}{2}\right) \frac{\cos(sx_1)}{sh + \sinh(sh)} \left\{ \left[\frac{sh}{2} \cosh\left(\frac{sh}{2}\right) - \sinh\left(\frac{sh}{2}\right) \right] \cosh(sx_2) - \right. \\ &\quad \left. sx_2 \sinh\left(\frac{sh}{2}\right) \sinh(sx_2) \right\} ds \\ \sigma_{22}(x_1, x_2) &= -\frac{2P}{\pi} \int_0^\infty \frac{2}{es} \sin\left(\frac{es}{2}\right) \frac{\cos(sx_1)}{sh + \sinh(sh)} \left\{ \left[\frac{sh}{2} \cosh\left(\frac{sh}{2}\right) + \right. \right. \\ &\quad \left. \left. \sinh\left(\frac{sh}{2}\right) \right] \cosh(sx_2) - sx_2 \sinh\left(\frac{sh}{2}\right) \sinh(sx_2) \right\} ds \\ \sigma_{12}(x_1, x_2) &= \frac{2P}{\pi} \int_0^\infty \frac{2}{es} \sin\left(\frac{es}{2}\right) \frac{\sin(sx_1)}{sh + \sinh(sh)} \left[\frac{sh}{2} \cosh\left(\frac{sh}{2}\right) \cdot \sinh(sx_2) - \right. \\ &\quad \left. sx_2 \sinh\left(\frac{sh}{2}\right) \cosh(sx_2) \right] ds\end{aligned}\tag{6.5}$$

which are numerically evaluated employing the Simpson's rule with 650 subintervals and $s = 700$ for the upper integrand limit. For plane stress state, the strain components can be obtained by

$$\begin{bmatrix} \varepsilon_{11} \\ \varepsilon_{22} \\ \varepsilon_{12} \end{bmatrix} = \begin{bmatrix} S_{11} & S_{12} & 0 \\ S_{12} & S_{11} & 0 \\ 0 & 0 & S_{44} \end{bmatrix} \begin{bmatrix} \sigma_{11} \\ \sigma_{22} \\ \sigma_{12} \end{bmatrix},\tag{6.6}$$

where $S_{11} = 1/E$, $S_{12} = -\nu/E$ and $S_{44} = (1 + \nu)/E$. Thus, the analytical strain energy is given by

$$U = \frac{1}{2} \int_{-\frac{l}{2}}^{\frac{l}{2}} \int_{-\frac{h}{2}}^{\frac{h}{2}} (\sigma_{11}\varepsilon_{11} + \sigma_{22}\varepsilon_{22} + \sigma_{12}\varepsilon_{12}) dx_2 dx_1 = 19.186 \text{ J.} \quad (6.7)$$

The analytical solution assumes stress-free boundary conditions at the lateral borders. Although the numerical solutions assume displacement restrictions at the lateral borders, the self-equilibrium concentrated loadings do not generate stresses at these borders due to Saint-Venant's principle.

Table 02 presents the investigated numerical aspects, such as the computational cost, energy values, and relative errors, for each simulation. Additionally, the result obtained for the analytical solution is also presented. As in the first example, the total strain energy and the work done by external loading evaluated using the zeroth-order finite-volume theory are equal for all performed simulations. While for the first and second-order versions of the theory, there is a difference of approximately 0.056% and 0.005%, respectively, between the total strain energy and the work done by external loading for the most refined mesh, which indicates a convergence between those different energy approaches when the adopted mesh is sufficiently fine.

Table 02 – Mechanical energy analysis for the rectangular beam under concentrated loads

Analysis	Mesh	ndof	Strain Energy			External Work		
			Processing Time (s)	Value (J)	Error (%)	Processing Time (s)	Value (J)	Error (%)
FVT ^{0th}	15x5	340	0.026	16.551	-13.73	0.026	16.551	-13.73
	75x25	7700	0.164	18.993	-1.010	0.157	18.993	-1.010
	150x50	30400	10.390	19.133	-0.277	10.388	19.133	-0.277
FVT ^{1st}	15x5	510	0.123	15.970	-16.76	0.030	15.684	-18.26
	75x25	11550	0.668	18.917	-1.404	0.652	18.877	-1.611
	150x50	45600	21.860	19.109	-0.402	22.097	19.098	-0.463
FVT ^{2nd}	15x5	680	0.057	16.047	-16.36	0.035	15.347	-20.01
	75x25	15400	1.664	18.841	-1.803	1.649	18.826	-1.879
	150x50	60800	33.717	19.083	-0.540	33.743	19.082	-0.547
Q4	15x5	192				0.024	11.479	-40.17
	75x25	3952				0.087	18.313	-4.555
	150x50	15402				4.197	18.929	-1.342
Q8	15x5	532				0.032	17.541	-8.575
	75x25	11652				1.669	19.160	-0.137
	150x50	45802				34.209	19.186	-0.002
Analytical	-	-	-	19.186	-	-	19.186	-

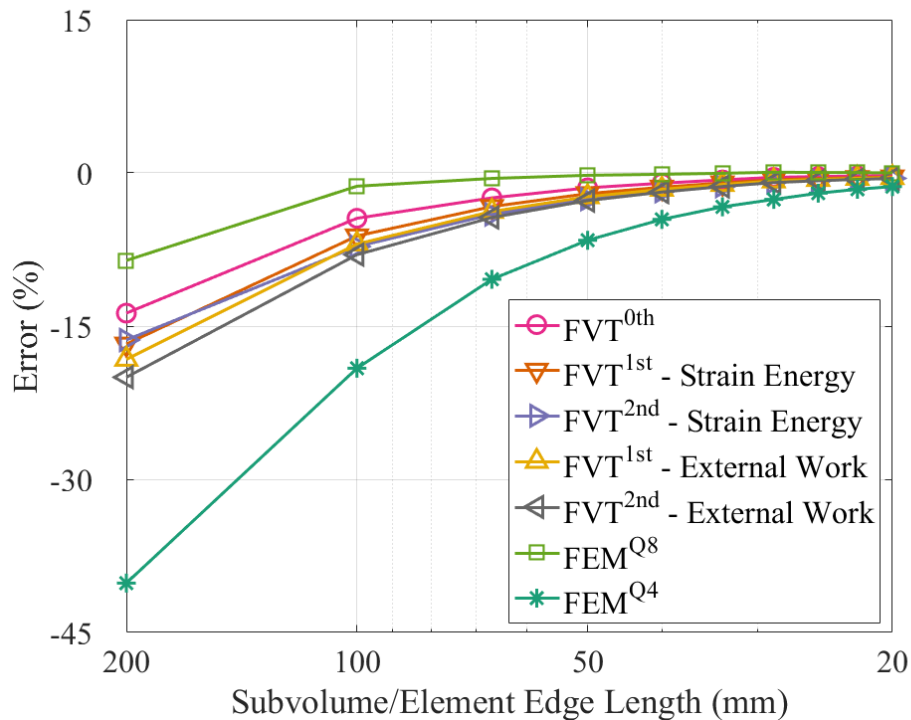
Font: Author (2022).

In terms of computational cost, the Q4 element approach is the fastest numerical solution, while the Q8 element is the slowest approach. Additionally, for the most refined

mesh, the zeroth-order finite-volume theory is approximately 2.48 times slower than the Q4 element approach, and the first and second-order finite-volume theories are 1.55 and 1.01 faster than the same approach based on the Q8 finite element. The number of degrees of freedom partially explains these differences in processing time.

The convergence study for each analyzed approach is shown in Figure 19. The Q8 element approach has presented the fastest convergence to the analytical solution, while the Q4 element has presented the slowest convergence. Also, all proposed approaches have provided a monotonic convergence to the analytical solution. For the higher-order versions of the generalized finite-volume theory, the analyzes based on the work done by external loading have presented a slower convergence and a stiffer response when compared to the same analyzes employing the total strain energy evaluation.

Figure 19 – Convergence analysis for the rectangular beam under concentrated loads

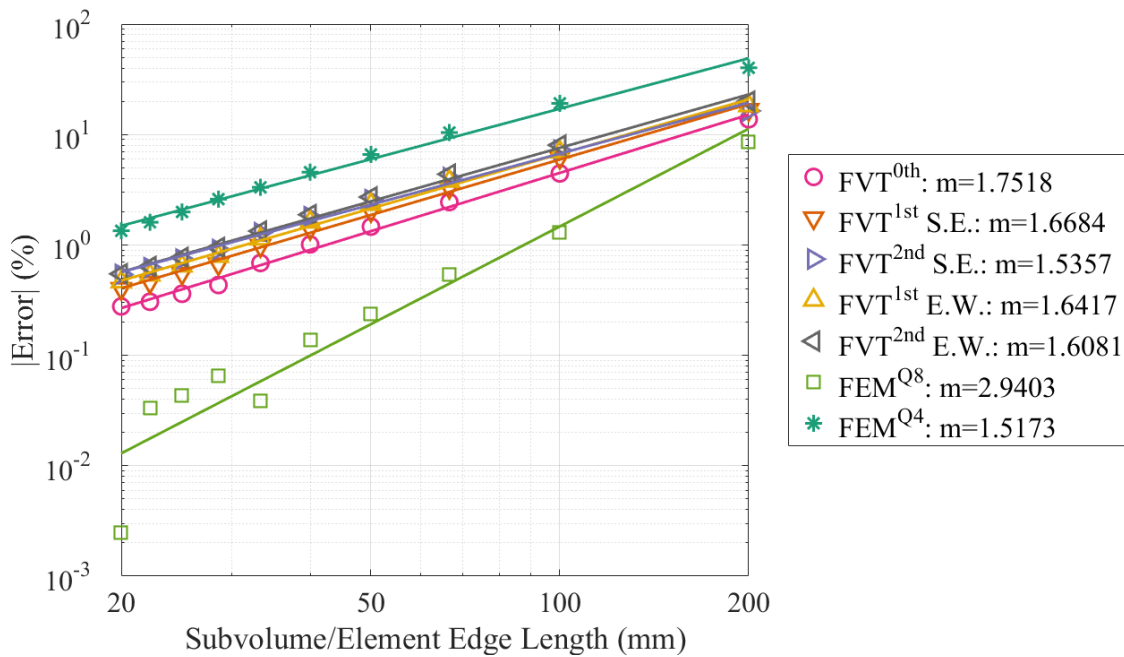


Font: Author (2022).

Figure 20 shows the convergence rate analysis for the rectangular beam under concentrated loads employing the analytical solution, where m is the angular coefficient (slope) of the linear regression adjustments (least-squares method) for the analyzed approaches considering a log-log value distribution in both axis. The Q8 element approach has the highest convergence rate and the best results, while the Q4 element approach presents

the worst convergence rate and the worst results for all the analyzed meshes. The zeroth-order finite-volume theory has the highest convergence rate and the best results among the finite-volume theory versions for this example. In general, the obtained convergence rates are in line with the expected values for the performed approaches, as the expectation is to obtain a value higher than 2 for the Q8 finite-element and values between 1 and 2 for the other approaches.

Figure 20 – Convergence rate analysis for the rectangular beam under concentrated loads



Font: Author (2022).

6.2 Compliance Minimization Problem based on the Generalized Finite-Volume Theory for Elastic Analysis

On this section, two different examples are analyzed, employing the three versions of the generalized finite-volume theory and Q4 and Q8 elements of the finite element method. The studied examples are a cantilever beam subjected to a concentrated load and a *Messerschmitt-Bölkow-Blohm* (MBB) beam. To confirm the checkerboard-free property of the approaches based on the finite-volume theory, the examples are firstly analyzed without employing filtering or image processing techniques. After that, the same examples are analyzed employing a filter that modifies the elements or subvolumes sensitivities, as presented in Equation (3.6), for mesh-independency.

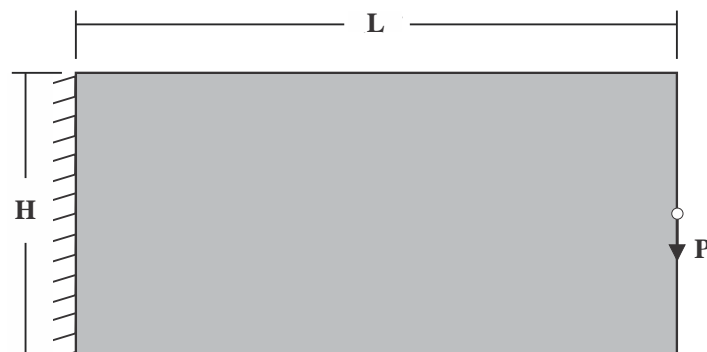
Some numerical aspects are investigated during the analysis, such as the number of iterations, processing time, convergence, and relative compliance. The continued penalization

scheme is adopted, where the penalty factor increases gradually ($\Delta p = 0.5$) from 1 to 4, as suggested by Talischi et al. (2012). As a convergence criterion, the tolerance for the maximum change between relative densities of successive steps is assumed to be 1%. In the absence of filtering techniques, each approach's damping factor is adjusted to avoid any divergence during the optimization process. The damping factor is set up as close as possible to 1/2, since no oscillation in the displacement field is verified when the algorithm is performed. The adopted damping factor for each simulation is shown in the following Tables and was obtained by varying increments of 0.1 as follows: 1/2, 1/2.1, 1/2.2, ..., until its findings convergence in the optimization process.

6.2.1 Example 1: Cantilever beam

A classical problem in the topology optimization of bidimensional structures is the cantilever beam, whose analysis domain and boundary conditions are presented in Figure 21. The proposed optimization problem consists of minimizing the structural compliance function, defined from the total strain energy, with a volume constraint of 40% of the total volume. The computational environment, in terms of programming language and machine, can be described as MatLab R2016a (64-bits)/Intel® Core™ i7 CPU 2.93 GHz/16.0 GB RAM/64-bits. Consistent units are employed for the physical and geometrical parameters.

Figure 21 – Cantilever beam

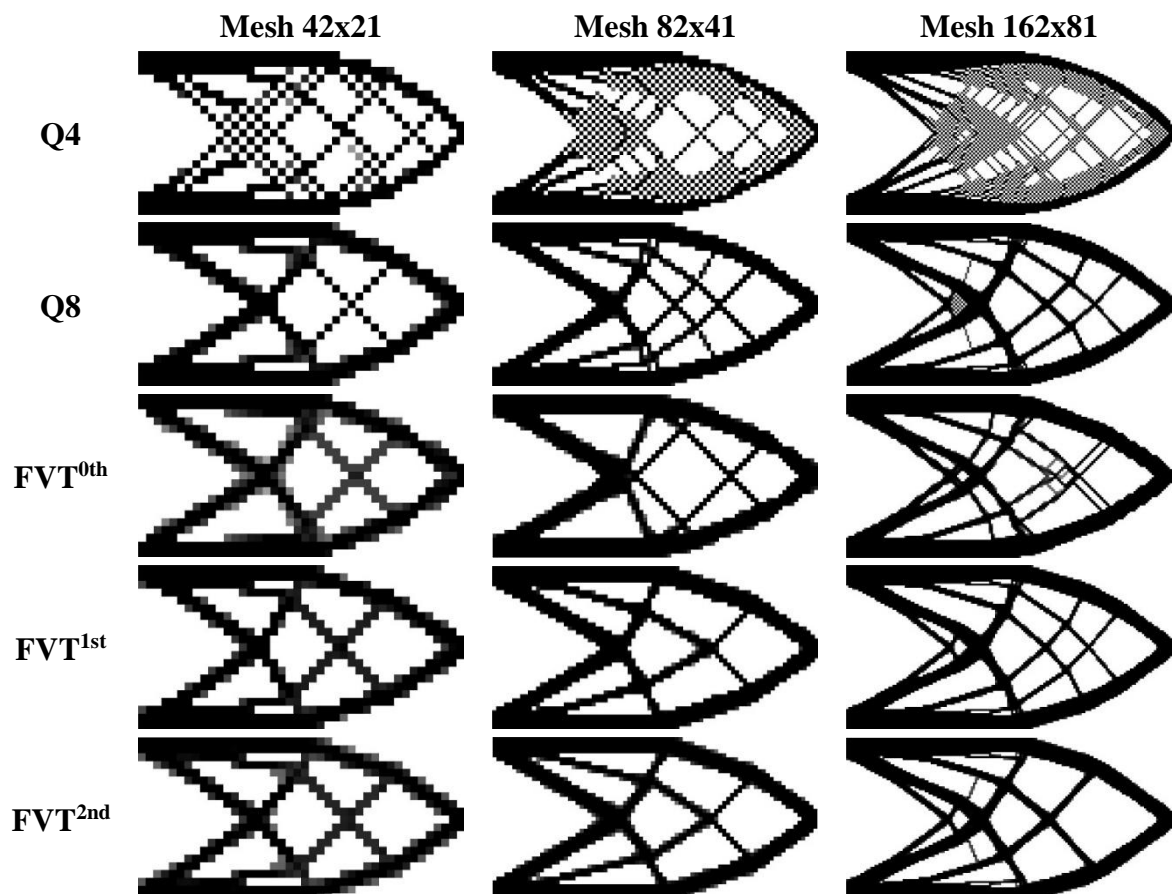


Font: Author (2022).

Figure 22 shows the optimized topologies obtained for each studied mesh size and employing the zeroth, first and second-order finite-volume theory (FVT0th, FVT^{1st}, and FVT^{2nd}, respectively) and the Q4 and Q8 elements. The optimized topologies obtained employing the finite-volume theory approaches have shown to be checkerboard-free. However, the approaches based on the finite element method have generated optimized topologies with the checkerboard pattern issue. For the Q4 element, the checkerboard emerges

in the overall structure, while for the Q8 element, the checkerboard appears only locally. Figure 23 shows the optimized topologies for the finite-element approaches and zeroth-order finite-volume theory; even for a mesh of 20402 Q8 elements, the checkerboard pattern continues to appear very locally. According to Díaz and Sigmund (1995), when the adopted penalty factor is higher than 2.29 in a Q8 finite element-based strategy, the obtained optimized topologies can present the formation of checkerboard regions. Thus, higher-order finite elements can produce checkerboard-free optimized topologies only when a sufficiently refined mesh is employed, which increases the computational cost. On the other hand, no checkerboard pattern has appeared when the finite-volume theory is employed, as shown in Figure 23.

Figure 22 – Optimized topologies for the cantilever beam analysis evaluating the compliance using the strain energy (No filtering)

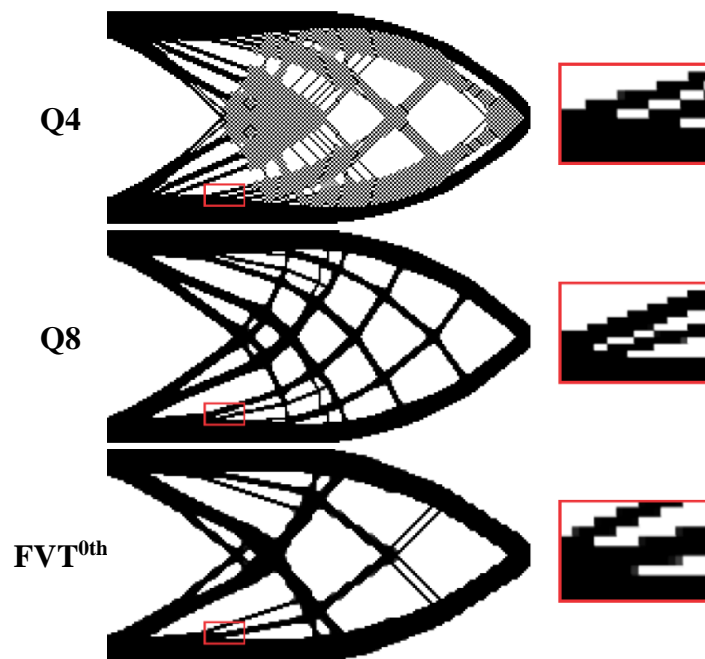


Font: Author (2022).

The checkerboard pattern problem in optimized topologies is directly related to the displacement assumptions of the finite element method, leading to structures artificially rigid (DÍAZ; SIGMUND, 1995). These anomalies are directly related to spurious modes in finite-

element solutions. In these cases, the topology optimization problem's weak formulations induce a variational form that involves independent displacement and density fields, so some combinations of density and displacement interpolation functions can generate designs free of checkerboard regions (JOG et al., 1993 and 1994). According to Jog and Haber (1996), the theory of variational problems for the finite-element method provides an excellent framework to understand the causes of checkerboard patterns. However, the analysis of mixed finite-element models for topology optimizations is complicated due to their non-linear nature. Although Jog and Haber (1996) have pointed out that the Q8 element is stable for checkerboard pattern problem, due to the numerical and computational approaches employed in the topological optimization techniques based on the finite element analysis, the local formation of checkerboard regions can be observed, as illustrated in Figure 23.

Figure 23 – Optimized topologies for the cantilever beam analysis with a mesh size of 202x101 (No filtering)



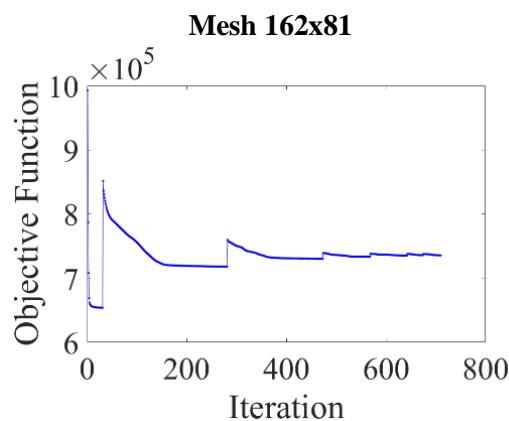
Font: Author (2022).

One of the purposes of this dissertation is to provide a more straightforward idea to solve numerical issues associated with the checkerboard pattern problem once these anomalies are related to the numerical technique usually employed in topology design problems. Since the finite-element method's equilibrium equations and compatibility conditions are established in nodes, nodal connections between adjacent elements are expected in the optimized topologies. As a result, the obtained structure is formed by plates

connected by pins, providing an optimized structure artificially rigid. On the other hand, the satisfaction of equilibrium equations and continuity conditions through the faces of adjacent subvolumes guarantees the checkerboard-free property for the different versions of the finite-volume theory, even when no filtering technique is employed. These features of the finite-volume theory ensure connections between edges of adjacent subvolumes, providing optimized structures more compatible with continuum mechanics assumptions. In addition, for the finite-volume theory, the checkerboard problem would be characterized by regions with disconnected subvolumes, while in the finite-element method, the checkerboard regions are characterized by elements connected by nodes.

However, the optimized topologies obtained for the finite-volume theory approaches, presented in Figure 22, have shown the presence of more subvolumes with the intermediate values of relative density compared to the finite-element approaches. This condition comes from the finite-volume approach to avoid the formation of checkerboard regions with disconnected subregions, inserting some intermediate values of relative density in these neighboring regions. Thus, it is common to observe the presence of more gray regions in the optimized topologies obtained by the finite-volume theory approaches.

Figure 24 – Objective function history along the optimization process for the Q4 finite-element (No filtering)

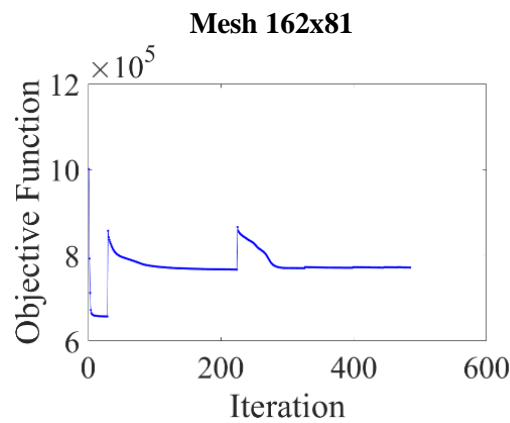


Font: Author (2022).

Figures 24 to 28 present the objective function evolution during the iteration process for the Q4 and Q8 finite-elements, zeroth, first and second-order finite-volume theories, considering the finest employed mesh. In this case, the objective function is considered as the structural strain energy for the finite-volume theory approaches. The presented objective function histories have shown a monotonic convergence with different levels of energy, which

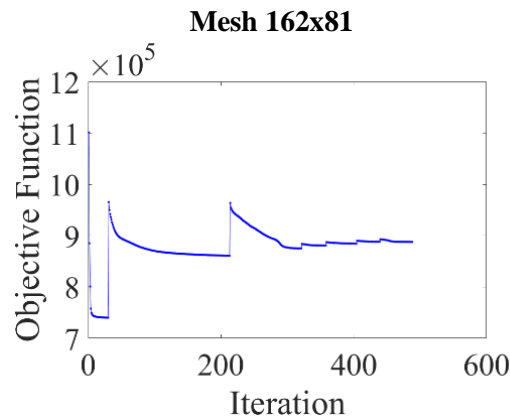
are directly associated with the change in the penalty factor once the continued penalization scheme is adopted. Additionally, with the mesh refinement, the levels of the objective function evolution become well-established, mainly when the last value for penalty factors is achieved. As a result, it is not observed any unusual behavior in the performed analyzes by analyzing the objective function evolution along the iterative process.

Figure 25 – Objective function history along the optimization process for the Q8 finite-element (No filtering)



Font: Author (2022).

Figure 26 – Objective function history along the optimization process for the zeroth-order finite-volume theory (No filtering)



Font: Author (2022).

Figure 27 – Objective function history along the optimization process for the first-order finite-volume theory and compliance defined from the total strain energy (No filtering)

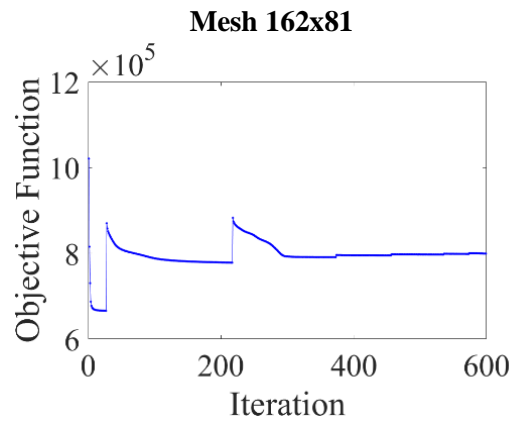


Figure 28 – Objective function history along the optimization process for the second-order finite-volume theory and compliance defined from the total strain energy (No filtering)

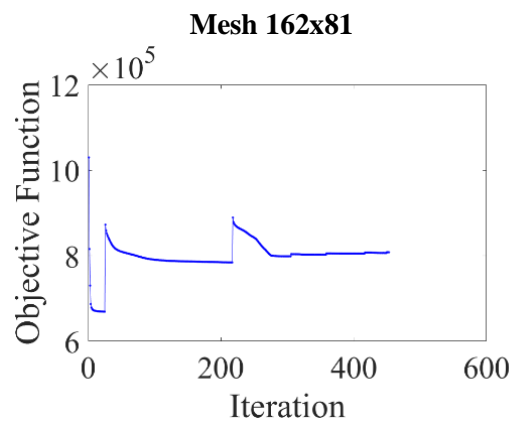


Table 03 presents the total number of iterations, the processing time, the number of degrees of freedom, the relative compliance, and the adopted damping factor, set up to avoid divergence in the optimization process. In general, the number of iterations has varied from one approach to another, presenting higher values when the first-order finite-volume theory and Q4 approaches are employed, and the lowest value was obtained for the second-order finite-volume theory followed by the Q8 and FVT^{0th} approaches. The zeroth-order finite-volume theory has been approximately 1.08 times slower than the Q4 approach for the finest mesh in terms of computational cost. The Q8 approach has presented the highest computational cost: 1.20 times slower than the first-order finite-volume theory and 1.04 times slower than the second-order finite-volume theory, for the finest mesh. The number of degrees

of freedom explains these differences in the computational cost partially since it defines the size of the global system of equations.

Table 03 – Convergence analysis for the cantilever beam evaluating the compliance using the strain energy (No filtering)

Analysis	Mesh	NDOF	Number of Iterations	Processing Time	Damping factor	Relative Compliance
Q4	42x21	1892	270	37 s	1/2.5	1.11808
	82x41	6972	360	10 min 35 s	1/2.5	1.19271
	162x81	26732	710	5 h 24 min 56 s	1/2.6	1.17733
Q8	42x21	5546	266	2 min 37 s	1/2.3	1.00000
	82x41	20666	397	52 min 18 s	1/2.4	1.00000
	162x81	79706	485	15 h 6 min 16 s	1/2.6	1.00000
FVT ^{0th}	42x21	3654	252	51 s	1/2.6	1.10259
	82x41	13694	306	12 min 44 s	1/2.6	0.99889
	162x81	52974	488	5 h 52 min 13 s	1/2.6	1.02000
FVT ^{1st}	42x21	5481	394	2 min 22 s	1/2.8	1.02697
	82x41	20541	376	25 min 1 s	1/2.8	0.99319
	162x81	79461	599	12 h 33 min 28 s	1/3.6	0.99652
FVT ^{2nd}	42x21	7308	287	1 min 25 s	1/3.0	1.06936
	82x41	27388	326	48 min 54 s	1/3.0	1.00437
	162x81	105948	453	14 h 32 min 8 s	1/3.2	0.99906

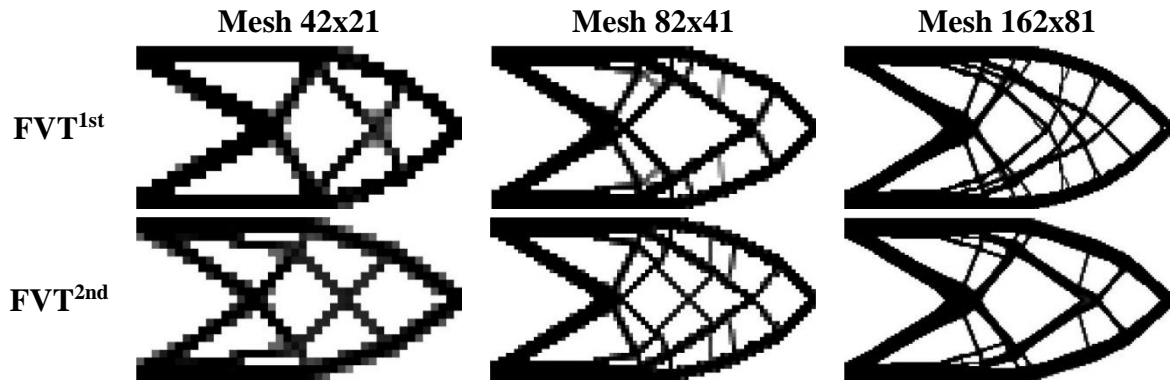
Font: Author (2022).

For a fair and transparent comparison, the compliance of each optimized topology obtained by different approaches is recalculated by employing the Q8 finite-element approach and then divided by the compliance of the optimized topology obtained by the Q8 approach. These relative compliance estimations are presented in Table 03 for the approaches performed in the absence of filtering techniques, with the compliance considered as the strain energy. Thus, the first-order version of the finite-volume theory approach has generally presented the stiffest optimized structures for the performed approaches. In contrast, the Q4 finite-element approach has obtained more flexible optimized structures since the relative compliance values are higher when compared to the other performed approaches.

Similarly, the proposed optimization problem can also be solved by defining the structural compliance as twice the work done by external loading. The obtained optimized topologies are shown in Figure 29 for the first and second-order finite-volume theory since the total strain energy and the work done by external forces are equivalent to the approaches based on the finite element method and the zeroth-order finite-volume theory. The numerical aspects investigated for convergence analysis can be found in Table 04, and the objective function evolution with a monotonic convergence for different discretization levels along the

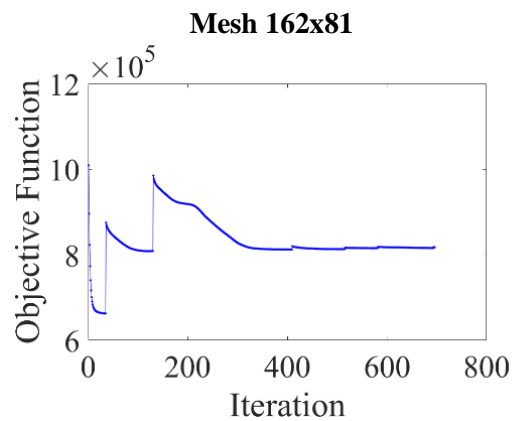
iteration process can be seen in Figures 30 and 31 for the first and second-order finite-volume theories when the compliance function is defined from the work done by external loading. In these analyzes it is not observed any anomalies in the objective function evolution graphs, as expected.

Figure 29 – Optimized topologies for the cantilever beam analysis evaluating the compliance using the work done by external loading (No filtering)



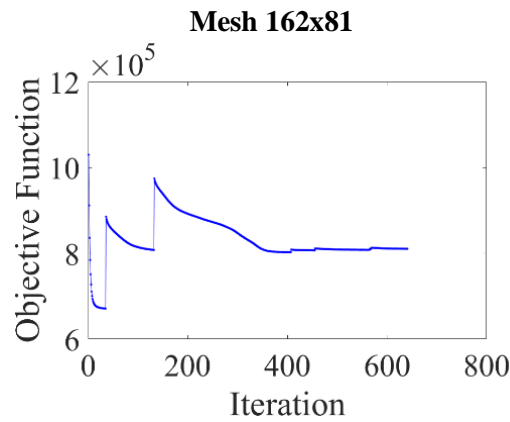
Font: Author (2022).

Figure 30 – Objective function history along the optimization process for the first-order finite-volume theory and compliance defined as twice the external work (No filtering)



Font: Author (2022).

Figure 31 – Objective function history along the optimization process for the second-order finite-volume theory and compliance defined as twice the external work (No filtering)



Font: Author (2022).

Table 04 – Convergence analysis for the cantilever beam evaluating the compliance using the work done by external loading (No filtering)

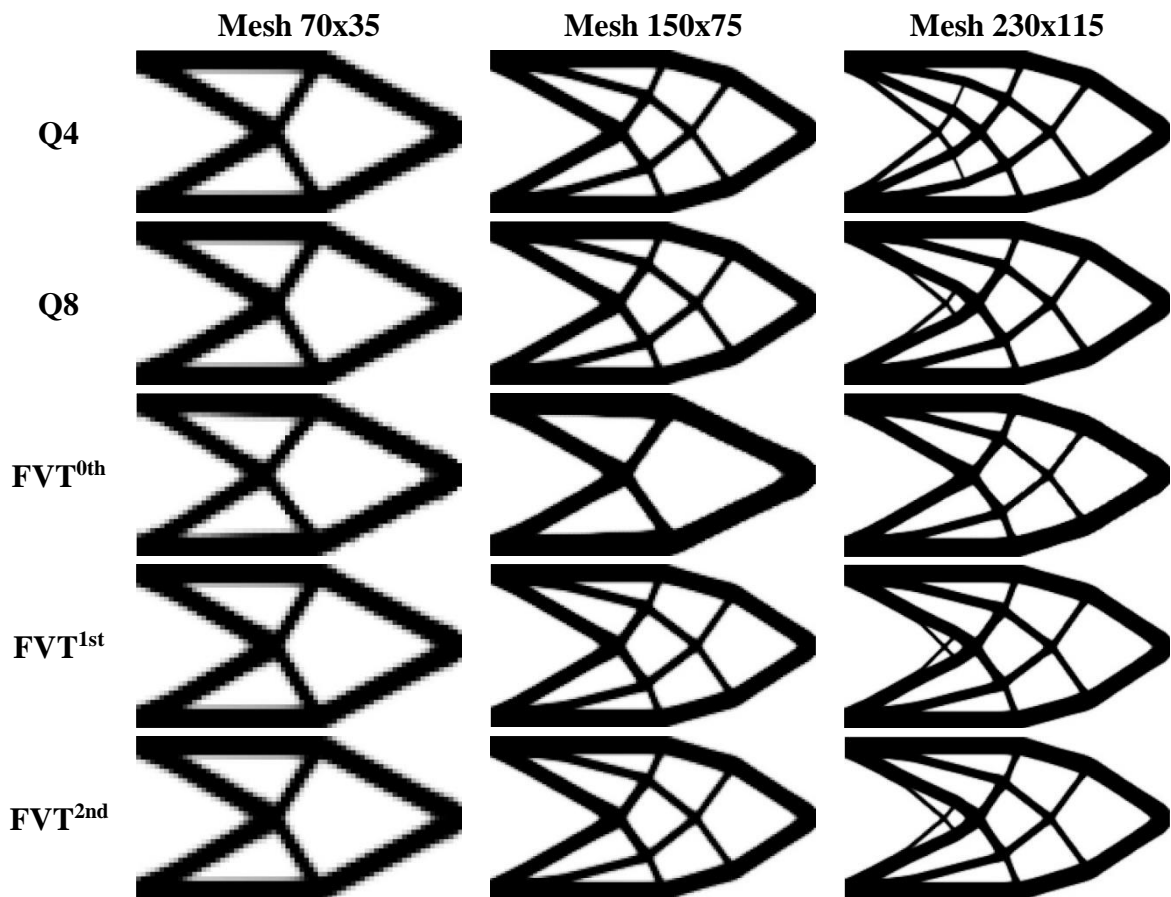
Analysis	Mesh	NDOF	Number of Iterations	Processing Time	Damping factor	Relative Compliance
FVT ^{1st}	42x21	5481	374	1 min 5 s	1/6.2	0.99497
	82x41	20541	401	21 min 37 s	1/8.0	1.01117
	162x81	79461	696	13 h 48 min 11 s	1/10.0	1.01764
FVT ^{2nd}	42x21	7308	287	1 min 25 s	1/3.0	1.06935
	82x41	27388	514	56 min 54 s	1/8.3	1.00375
	162x81	105948	641	20 h 11 min 14 s	1/10.2	1.00405

Font: Author (2022).

When the compliance function is estimated using the external work done by external loading, the optimized topologies tend to show more bars and length scale issues, as illustrated on the optimized topologies presented in Figure 29. The damping factors for these approaches have shown to be much lower when compared to the same approaches employing the strain energy, which turns the convergence process slower and increases the computational cost. The number of iterations tends to be higher, making the approaches employing the external work done by external loading more computational costly, as shown in Table 04. Additionally, the compliance function values for the optimized topologies are higher when the compliance is defined from the work done by external loading. In fact, for the current example, the objective function is better estimated when the compliance function is defined as the strain energy of a deforming material, which guarantees minimum values for the objective function and reduces the oscillatory phenomenon providing faster convergence to the optimization process.

As shown in Figures 22 and 29, although the checkerboard pattern issue can be overcome by the topology optimization approach based on the finite-volume theory, the mesh dependence between successive meshes persists. Therefore, the mesh-independency filter, presented in section 3.4, is employed to avoid mesh dependence, in the approaches based on the finite-volume theory, and checkerboard pattern and mesh dependence, in the approaches based on the finite element method. The optimized topologies for the same problem employing the sensitivity filtering are presented in Figure 30. In this case, the compliance function is evaluated as twice the structural strain energy, and the damping factor is adjusted as 1/2 for all investigated approaches.

Figure 32 – Optimized topologies for the cantilever beam analysis evaluating the compliance using the strain energy (filtering)

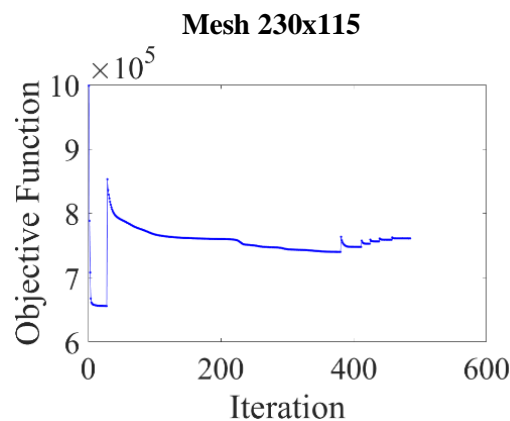


Font: Author (2022).

The optimized topologies presented in Figure 32 are checkerboard-free, and the mesh dependence is better controlled in this scenario. There are some differences between the optimized topologies obtained by the finite-volume theory and the approaches based on the finite element method. In general, the filter radius of $R = 1.01\sqrt{(l_e)^2 + (h_e)^2}$ is sufficient to

solve the checkerboard instability in the employed finite element-based strategies, which does not guarantee the absence of mesh dependence. Usually, this filter radius must be constant for all performed approaches for mesh-independency, independently of the adopted mesh. This varying filter radius is adopted to test which of the analyzed approaches presents more sensitivity with the mesh-refinement by obtaining optimized topologies with more slender bars. For a varying filter radius which only guarantees the absence of checkerboard regions, the optimized topologies obtained by the zeroth-order finite-volume theory have reduced the mesh dependence between successive meshes, providing topologies with fewer bars and reducing the length scale issue, when compared to the other performed approaches.

Figure 33 – Objective function history along the optimization process for the Q4 finite-element (filtering)

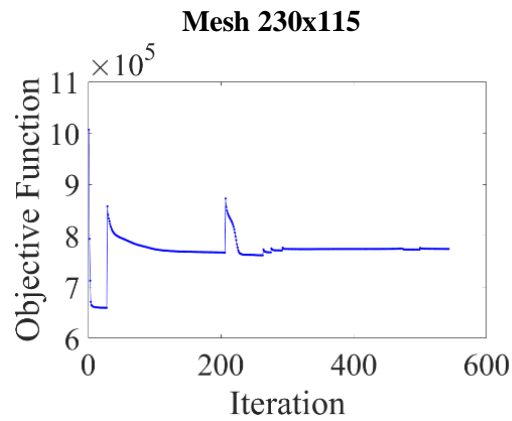


Font: Author (2022).

The most critical topologies are obtained for the Q4 element approach, in this case, the optimized topologies present slender bars with length scale issues, undesirable features for manufacturing. The approaches based on the Q8 element, first and second-order finite-volume theories have presented similar optimized topologies with more bars when compared to the zeroth-order finite-volume theory approach, and fewer bars and length scale issues when compared to the Q4 element approach. In general, the optimized topologies obtained by the zeroth-order finite-volume theory approach are well behaved and more indicated for the design of optimized structures. However, a different dependence can be observed in the optimized topologies since sub-parametric subvolumes, or elements are employed. As a result, the connection between subvolumes or elements occurs in a stair format, which differs from the analytical solution obtained by Michell (1904). This feature is better observed in the obtained optimized topologies for the coarsest mesh in Figure 32. Figures 33 to 37 show the evolution of the objective function during the optimization process, where it is observed a

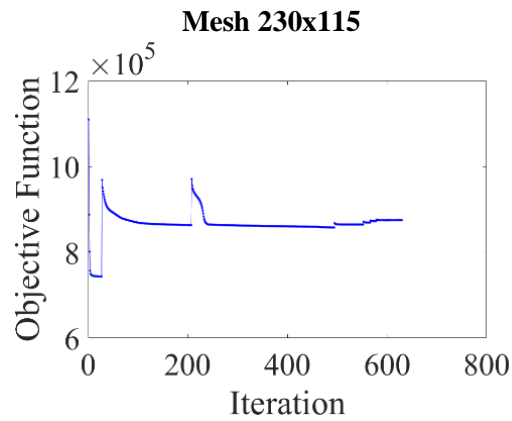
tendency of increasing in the compliance function for the higher values of the penalty factor, including the results obtained for the finest mesh. These graphs do not present any anomalies that should be matter of concerns.

Figure 34 – Objective function history along the optimization process for the Q8 finite-element (filtering)



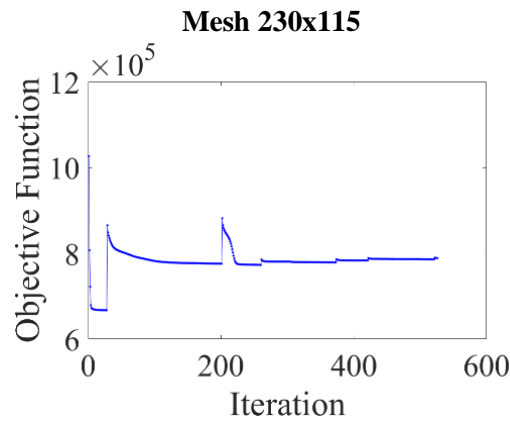
Font: Author (2022).

Figure 35 – Objective function history along the optimization process for the zeroth-order finite-volume theory (filtering)



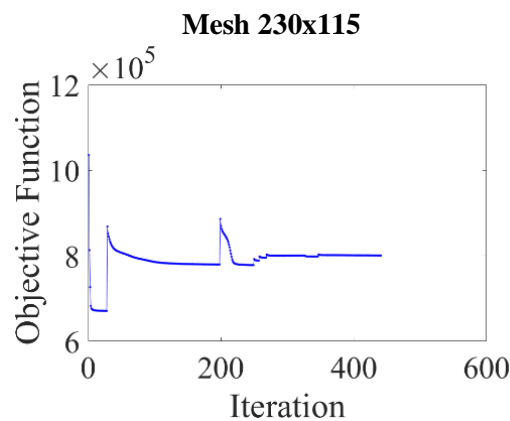
Font: Author (2022).

Figure 36 – Objective function history along the optimization process for the first-order finite-volume theory (filtering)



Font: Author (2022).

Figure 37 – Objective function history along the optimization process for the second-order finite-volume theory (filtering)



Font: Author (2022).

Table 05 presents the results obtained for the overall convergence of the different topology optimization approaches, considering the application of a mesh independent filter that regularizes the element or subvolume sensitivities. In general, the number of iterations has changed from one approach to another, where the minimum values are observed for the second-order finite-volume theory and the Q4 approaches. In terms of computational cost, the Q8 approach has presented the highest processing time, while the Q4 approach has presented the lowest computational cost. The approach based on the zeroth-order finite-volume theory is 1.8 times slower than the same approach based on the Q4 element, for the finest mesh. The number of degrees of freedom explains the computational efficiency of the Q4 approach partially since it defines the size of the global system of equations.

Table 05 – Convergence analysis for the cantilever beam evaluating the compliance using the strain energy (filtering)

Analysis	Mesh	NDOF	Number of Iterations	Processing Time	Relative compliance
Q4	70x35	5112	230	5 min 6 s	1.00053
	150x75	22952	293	1 h 27 min 50 s	1.00056
	230x115	53592	485	14 h 30 min 55 s	1.00364
Q8	70x35	15122	153	10 min 46 s	1.00000
	150x75	68402	320	7 h 9 min 4 s	1.00000
	230x115	160082	543	69 h 3 min 55 s	1.00000
FVT ^{0th}	70x35	10010	156	3 min 15 s	1.01019
	150x75	45450	329	2 h 19 min 2 s	0.99068
	230x115	106490	630	26 h 6 min 54 s	0.99536
FVT ^{1st}	70x35	15015	156	6 min 43 s	0.99833
	150x75	68175	285	4 h 16 min 41 s	0.99952
	230x115	159735	526	43 h 24 min 51 s	0.99731
FVT ^{2nd}	70x35	20020	152	11 min 7 s	1.00309
	150x75	90900	254	5 h 36 min 59 s	1.00419
	230x115	212980	441	55 h 22 min 29 s	1.00246

Font: Author (2022).

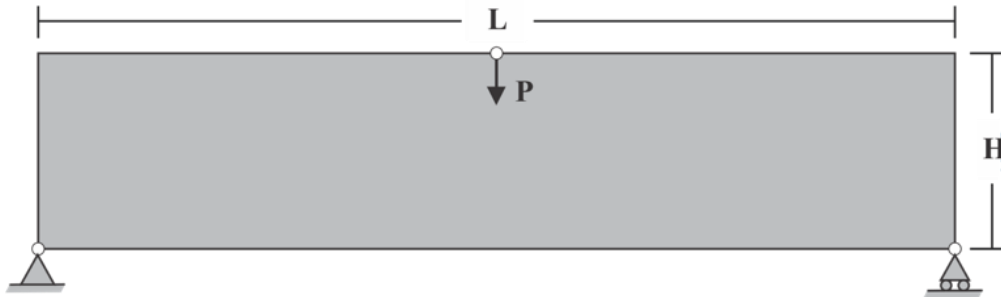
In Table 05, it is presented a numerical parameter, denoted as relative compliance, permitting the comparison between the different approaches in terms of the lowest compliant structure. This value is obtained by recalculating each optimized topology's structural compliance employing a Q8 element; after that, this result is divided by the compliance obtained for the Q8 optimized topologies for the same mesh sizes. The relative compliance values show that the stiffest structures are obtained when the zeroth-order finite-volume theory is employed, especially for the finest mesh, while the approaches based on the Q4 element and the second-order finite-volume theory result in more flexible structures.

6.2.2 Example 2: Messerschmitt-Bölkow-Blom (MBB) beam

Another classical problem in topology optimization is known as *Messerschmitt-Bölkow-Blom* (MBB) beam, whose analysis domain and boundary conditions are shown in Figure 38. The optimization problem consists of finding the stiffest structure with a given volume fraction of 50%. Taking advantage of the structure symmetry, only half of the structure is analyzed, employing boundary conditions that reflect this symmetry. Additionally, in the model conception, consistent units for the physical and geometric parameters are employed. The computational environment for this example, in terms of programming

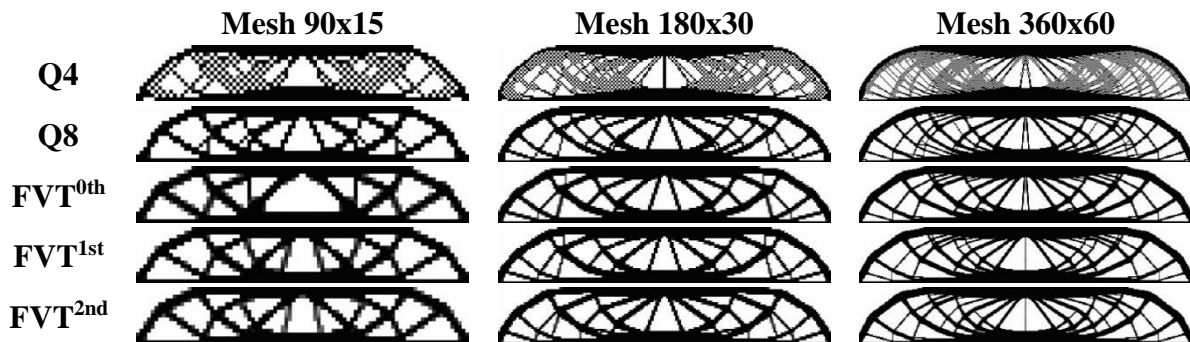
language and machine, can be described as MatLab R2018a (64-bits)/Intel® Core™ i7-8550U CPU @ 1.80 GHz 1.99 GHz/16.0 GB RAM/64-bits.

Figure 38 – Messerschmitt-Bölkow-Blom (MBB) beam



Font: Author (2022).

Figure 39 – Optimized topologies for the MBB beam analysis evaluating the compliance using the strain energy (No filtering)

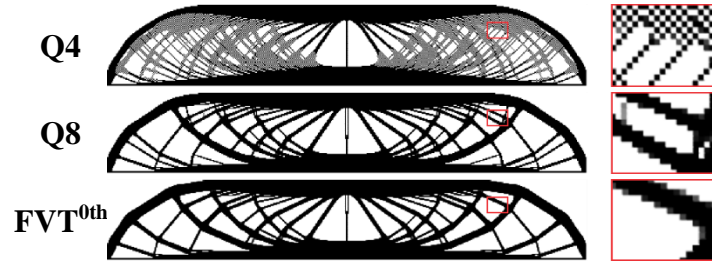


Font: Author (2022).

Figure 39 shows the optimized topologies for the approaches based on the finite-volume theory and Q4 and Q8 elements in the absence of filtering or image processing techniques, where the compliance function is evaluated as the strain energy. As presented in the previous example, the checkerboard pattern is an issue for the finite element-based approaches, mainly when the Q4 element is employed. Even for the finest mesh of the Q8 element, the checkerboard pattern appears locally, which is an undesired issue since the obtained optimized topologies are artificially rigid. Figure 40 presents the optimized topologies obtained for the approaches based on the zeroth-order finite-volume theory and finite-element strategies. Thus, these results evidence the presence of checkerboard regions for the finite-element analysis, especially for the Q4 element. Even for a mesh of 38400 Q8 elements, the checkerboard pattern continues to appear. Although Jog and Haber (1996) have proved the stability of the Q8 element for topology optimization problems, it is observed the occurrence of checkerboard regions for the performed analyzes. Additionally, Díaz and

Sigmund (1995) have explained that this stability is only guaranteed when the penalty factor is lower than 2.29.

Figure 40 – Optimized topologies for the MBB beam analysis and a mesh of 480x80 (No filtering)



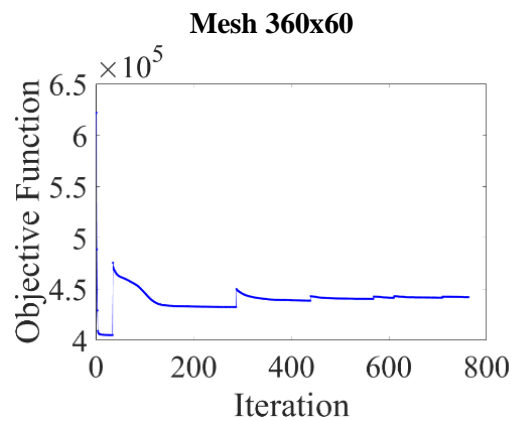
Font: Author (2022).

The checkerboard pattern numerical issue is directly related to the assumptions of the finite-element method once the modeling is based on nodal equilibrium and compatibilization, which allows nodal connections between neighboring elements. On the other hand, in the three versions of the generalized finite-volume theory, the presence of checkerboard regions is not verified, which ratifies the finite-volume theory feature of connections through edges. The optimized topologies presented in Figure 39 for the coarsest meshes and employing the finite-volume theory approaches present more gray regions, which come from the fact that these approaches avoid the formation of checkerboard regions, tending to generate intermediate values of density, allowing checkerboard-free optimized topologies, even when very coarse meshes are employed.

In topology optimization based on the finite-volume theory, the checkerboard is characterized by a set of disconnected regions once the satisfaction of equilibrium and continuity conditions ensures connections through the faces of adjacent subvolumes. On the other hand, in topology optimization algorithms based on the finite-element method, the physical anomaly caused by the checkerboard numerical issue is characterized by the formation of regions connected by nodes. As a result, this numerical problem emerges from the physical modeling promoted by the finite-element strategy, which designs the optimization problem by considering different regions connected by pins, so the checkerboard surges because of the physical assumptions of the employed method. The damping factor for each simulation was adjusted to avoid any divergence during the optimization process. The adopted damping factors are shown in Table 06. Figures 41 to 45 show the objective function evolution for the obtained optimized topologies in the absence of filtering techniques and consider the objective function as the structural strain energy in the finite-volume theory

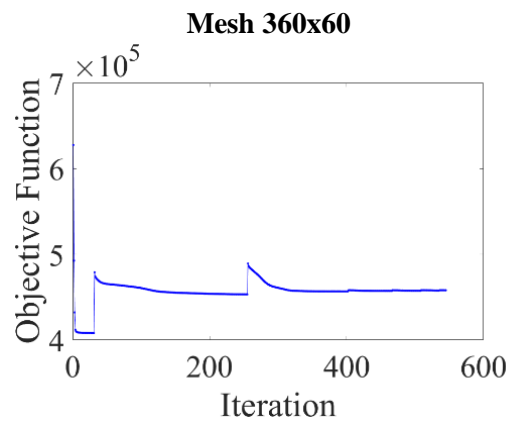
approaches. The presented curves show a monotonic convergence in different discretization levels, where the energy shows a convergence with mesh refinement and increasing the penalty factor, and it is not observed any kind of unusual behavior in those analyzes.

Figure 41 – Objective function history along the optimization process for the Q4 finite-element (No filtering)



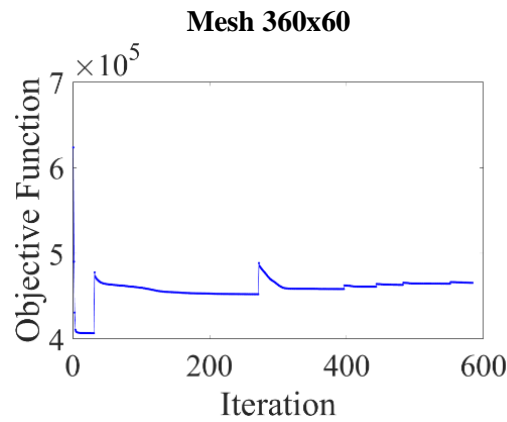
Font: Author (2022).

Figure 42 – Objective function history along the optimization process for the Q8 finite-element (No filtering)



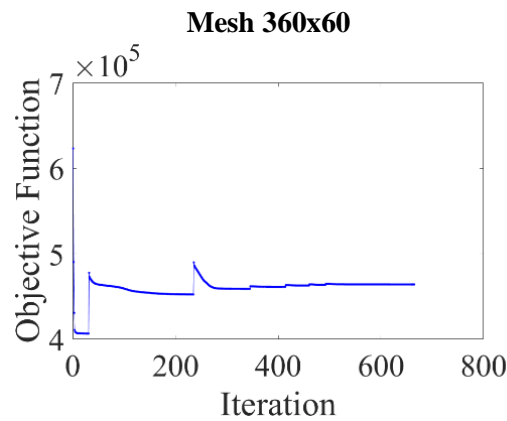
Font: Author (2022).

Figure 43 – Objective function history along the optimization process for the zeroth-order finite-volume theory (No filtering)



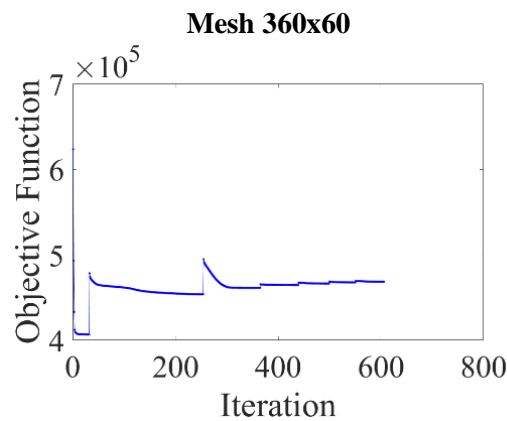
Font: Author (2022).

Figure 44 – Objective function history along the optimization process for the first-order finite-volume theory and compliance defined from the total strain energy (No filtering)



Font: Author (2022).

Figure 45 – Objective function history along the optimization process for the second-order finite-volume theory and compliance defined from the total strain energy (No filtering)



Font: Author (2022).

Table 06 presents the obtained results for the overall convergence analysis employing the three versions of the generalized finite-volume theory, and Q4 and Q8 elements of the finite element method, where the structural compliance is defined as the strain energy. The number of iterations has varied from one approach to another, mainly when the Q4 element is employed. The adopted damping factor explains the high number of iterations partially for the finite-volume theory approaches since it provides a slow convergence for the optimization process. In terms of computational cost, the second-order finite-volume theory has presented the highest processing time, while the Q4 approach has presented the lowest computational cost. As a result, the zeroth-order finite-volume theory is 1.15 slower than the Q4 approach and 2.93 times faster than the Q8 approach. The second-order finite-volume theory is 1.06 times slower than the Q8 approach and 3.56 slower than the Q4 approach. The first-order finite-volume theory is 2.65 times slower than Q4 approach and 1.27 times faster than the Q8 approach.

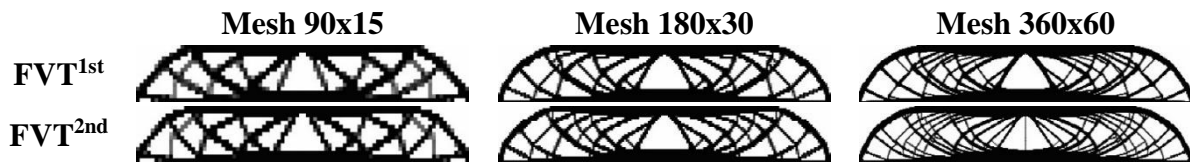
Table 06 – Convergence analysis for the MBB beam evaluating the compliance using the strain energy (No filtering)

Analysis	Mesh	NDOF	Number of Iterations	Processing Time	Damping factor	Relative Compliance
Q4	45x15	1472	248	10 s	1/2.5	1.08597
	90x30	5642	717	7 min 9 s	1/2.5	1.13654
	180x60	22082	763	3 h 25 min 6 s	1/2.6	1.12027
Q8	45x15	4292	322	43 s	1/2.5	1.00000
	90x30	16682	422	31 min 29 s	1/2.5	1.00000
	180x60	65762	545	11 h 28 min 33 s	1/2.5	1.00000
FVT ^{0th}	45x15	2820	253	13 s	1/2.6	1.07075
	90x30	11040	422	5 min 16 s	1/2.6	1.02507
	180x60	43680	584	3 h 55 min 11 s	1/2.6	1.00608
FVT ^{1st}	45x15	4230	401	48 s	1/3.2	1.04746
	90x30	16560	458	18 min 37 s	1/3.0	1.00459
	180x60	65520	665	9 h 2 min 31 s	1/2.7	0.99587
FVT ^{2nd}	45x15	5640	285	40 s	1/3.0	1.06244
	90x30	22080	362	20 min 20 s	1/3.0	1.01955
	180x60	87360	606	12 h 11 min	1/3.4	0.99845

Font: Author (2022).

The relative compliance values are obtained considering the Q8 element approach as the reference. From the values presented in Table 06, the higher-order versions of the generalized finite-volume theory have obtained the stiffest optimized topologies for the finest mesh. In contrast, the Q4 element approach has obtained more flexible optimized topologies compared to the other performed approaches.

Figure 46 – Optimized topologies for the MBB beam analysis evaluating the compliance using the work done by external loading (No filtering)



Font: Author (2022).

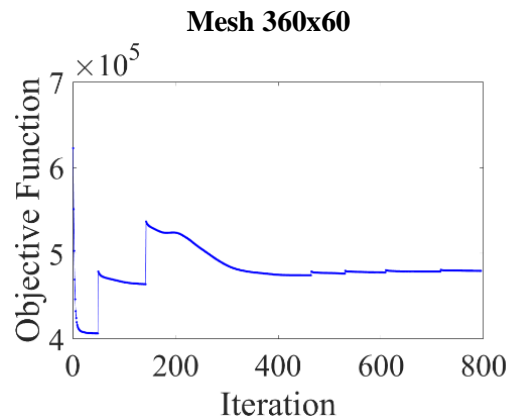
As mentioned before, the objective function can also be defined from the work done by external loading, since the external work is equivalent to the strain energy for a conservative mechanical system. However, for the first and second-order versions of the finite-volume theory, there is a residual difference when a not sufficiently refined mesh is employed. Figure 46 shows the optimized topologies obtained when the structural compliance function is defined from the work done by external loading. Table 07 presents the investigated numerical aspects during the optimization process, including the adopted damping factors for the performed analyzes. Figures 47 and 48 show the objective function evolution for the finest mesh with a monotonic convergence in different discretization levels along the optimization process, where it is observed an energy convergence along the iteration process and with the increasing in the penalty factor. Additionally, any unusual behavior is detected in the performed analyzes.

Table 07 – Convergence analysis for the MBB beam evaluating the compliance using the work done by external loading (No filtering)

Analysis	Mesh	NDOF	Number of Iterations	Processing Time	Damping factor	Relative Compliance
FVT ^{1st}	45x15	4230	368	54 s	1/9.8	1.16198
	90x30	16560	643	23 min 13 s	1/8.9	1.05287
	180x60	65520	795	11 h 36 min 8 s	1/11.8	1.03563
FVT ^{2nd}	45x15	5640	404	1 min 43 s	1/9.6	1.12843
	90x30	22080	571	45 min 47 s	1/9.8	1.05469
	180x60	87360	1077	24 h 24 min 54 s	1/10.9	1.04439

Font: Author (2022).

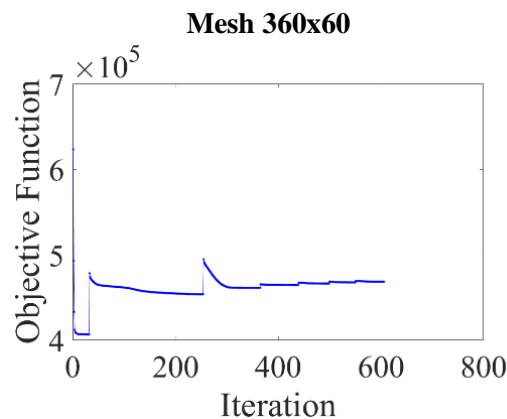
Figure 47 – Objective function history along the optimization process for the first-order finite-volume theory and compliance defined as twice the external work (No filtering)



Font: Author (2022).

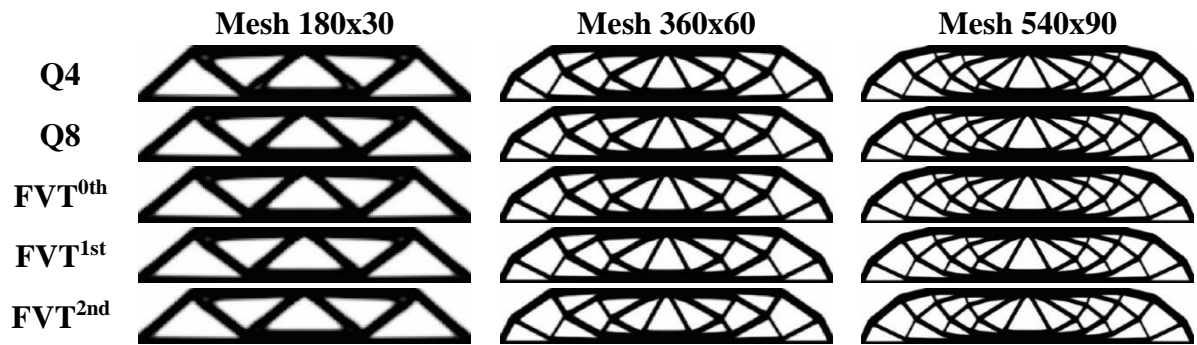
The obtained optimized topologies are similar from one approach to another, although the obtained numerical aspects are worst when the external work is employed, presenting an increase in the number of iterations occasioned by a reduction in the damping factor. Consequently, it is also registered an increase in the computational cost. In addition, the external work has provided more flexible optimized topologies, which is observed by the obtained relative compliance values in Table 07. Since the objective of the topology optimization problem is to provide less flexible or more rigid optimized structures, thus the objective function is better estimated when the structural compliance function is defined as the strain energy, which would also enhance the overall convergence of the optimization problem.

Figure 48 – Objective function history along the optimization process for the second-order finite-volume theory and compliance defined as twice the external work (No filtering)



Font: Author (2022).

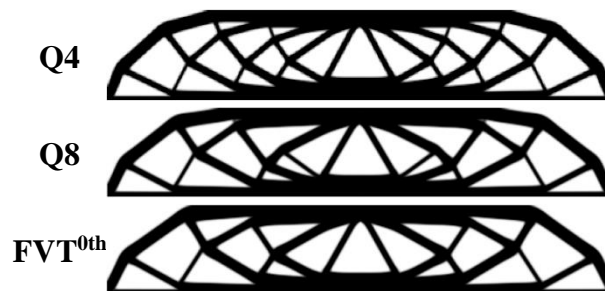
Figure 49 – Optimized topologies for the MBB beam analysis by evaluating the compliance using the strain energy (filtering)



Font: Author (2022).

The topology optimization algorithm is also performed, employing a sensitivity filter for mesh-independency. Figure 49 shows the obtained optimized topologies when the filtering technique is employed, which better controls the mesh dependence, in the case of the finite-volume theory approaches, and the checkerboard effect and mesh dependence, in the case of the finite element approaches. In addition, the optimized topologies presented in Figure 45 are practically the same for all different employed approaches. The employed filter generally guarantees only the absence of checkerboard regions in the optimized topologies. In this contribution, the filter radius is set as $R = 1.01\sqrt{(l_q)^2 + (h_q)^2}$ to verify which approaches present more sensibility with the mesh refinement. Thus, Figure 50 provides optimized topologies obtained by the zeroth-order finite-volume theory, Q4 and Q8 finite-elements considering a mesh size of 480x80, where the topology obtained by the approach based on the finite-volume theory has presented fewer bars and most with lower slenderness when compared with the topologies obtained by the approaches based on the Q4 and Q8 elements, showing less mesh sensitivity.

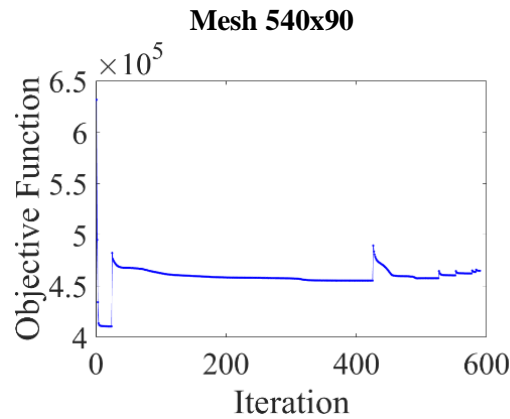
Figure 50 – Optimized topologies for the MBB beam analysis and a mesh of 480x80 (filtering)



Font: Author (2022).

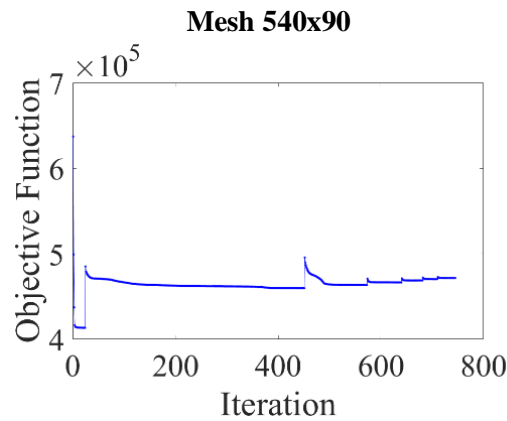
Figures 51 to 55 present the objective function evolution along the iteration process for the finest mesh, where it is observed convergence for each employed penalty factor and some increase in the compliance function for the final values of the penalty factor. In addition, the obtained curves are in line with the expected behavior for the performed analyzes.

Figure 51 – Objective function history along the optimization process for the Q4 finite-element (filtering)



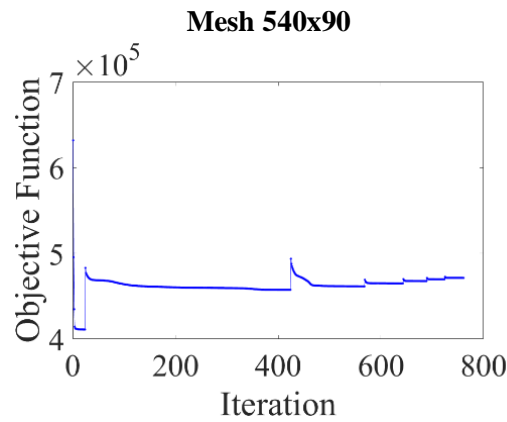
Font: Author (2022).

Figure 52 – Objective function history along the optimization process for the Q8 finite-element (filtering)



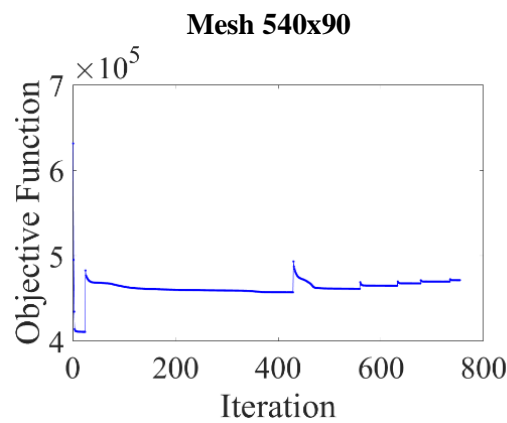
Font: Author (2022).

Figure 53 – Objective function history along the optimization process for the zeroth-order finite-volume theory (filtering)



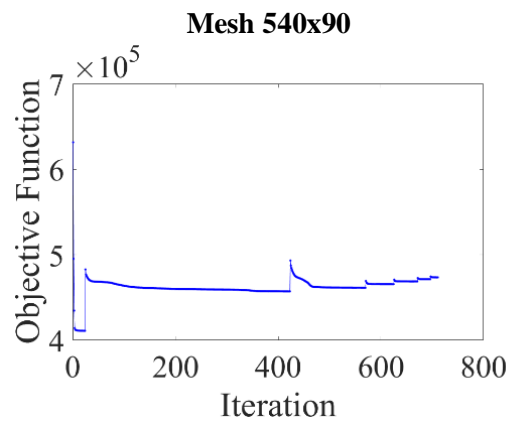
Font: Author (2022).

Figure 54 – Objective function history along the optimization process for the first-order finite-volume theory (filtering)



Font: Author (2022).

Figure 55 – Objective function history along the optimization process for the second-order finite-volume theory (filtering)



Font: Author (2022).

Table 08 – Convergence analysis for the MBB beam by evaluating the compliance using the strain energy (filtering)

Analysis	Mesh	NDOF	Number of Iterations	Processing Time	Relative compliance
Q4	90x30	5642	603	6 min 4 s	1.00082
	180x60	22082	367	1 h 25 min 9 s	1.00068
	270x90	49322	590	15 h 25 min 25 s	1.00057
Q8	90x30	16682	447	35 min 45 s	1.00000
	180x60	65762	650	14 h 26 min 13 s	1.00000
	270x90	147242	745	90 h 14 min 39 s	1.00000
FVT ^{0th}	90x30	11040	482	12 min 27 s	1.00333
	180x60	43680	664	5 h 30 min 48 s	1.00089
	270x90	97920	761	30 h 34 min 20 s	1.00063
FVT ^{1st}	90x30	16560	472	21 min 19 s	1.00252
	180x60	65520	684	8 h 38 min 1 s	1.00051
	270x90	146880	754	56 h 17 min 48 s	1.00033
FVT ^{2nd}	90x30	22080	428	41 min 4 s	1.00459
	180x60	87360	672	15 h 42 min 53 s	1.00262
	270x90	195840	711	79 h 38 min 34 s	1.00175

Font: Author (2022).

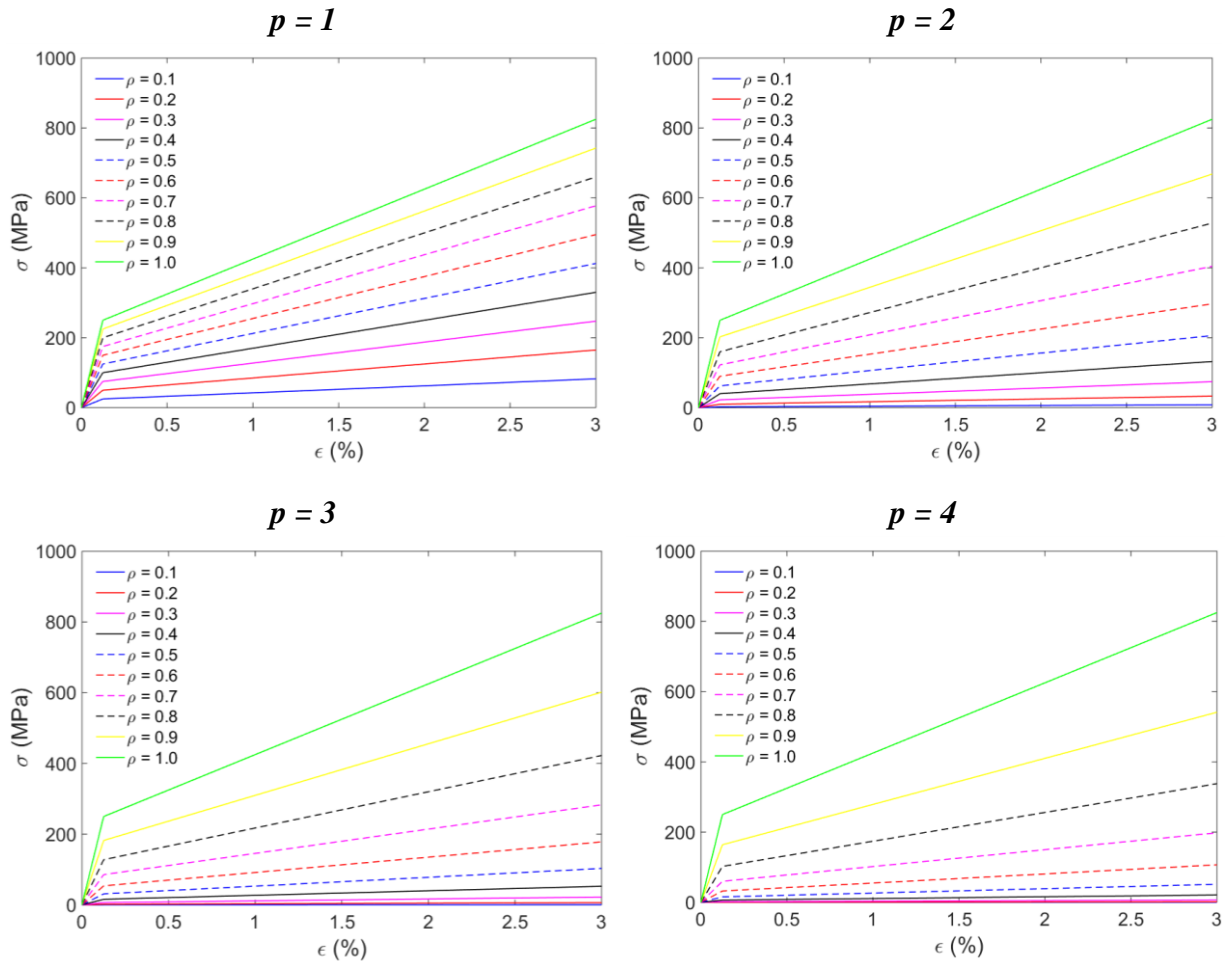
Table 08 presents the numerical results obtained for the convergence analysis of the different employed approaches, considering the application of the mesh-independency filter. In general, the numbers of iterations are similar for the different approaches, with the Q4 approach showing more substantial differences in comparison to the other ones. In terms of computational cost, the Q8 approach has presented the highest processing time, followed by the second-order finite-volume theory. The Q4 approach has presented the lowest computational cost, followed by the zeroth-order finite-volume theory. For the current example, the stiffest structure was obtained for the Q8 approach, presenting the smallest compliance, where the values shown in Table 06 are relative to the optimized topology obtained by the Q8 element approach. In the relative compliance calculation, the compliance is evaluated employing the Q8 finite element for the optimized topologies obtained by the different approaches, for a fair comparison.

6.3 Compliance Minimization Problem based on the Standard Finite-Volume Theory for Elastoplastic Analysis

In this section, the cantilever beam example shown in Figure 21 is analyzed for topology optimization of compliance minimization problem based on the standard finite-volume theory considering an elastoplastic material behavior. Additionally, some numerical

aspects are investigated during the analysis, such as the number of iterations, processing time and convergence. The continued penalization scheme is also adopted with gradual increments of 0.25 and the convergence criteria is set as 1% for the maximum relative material density variation between successive steps. The analysis is also performed employing a filter that modifies the subvolumes sensitivities as presented in Equation (3.6) for mesh-independency.

Figure 56 – Penalization effect at the equivalent uniaxial stress-strain diagram



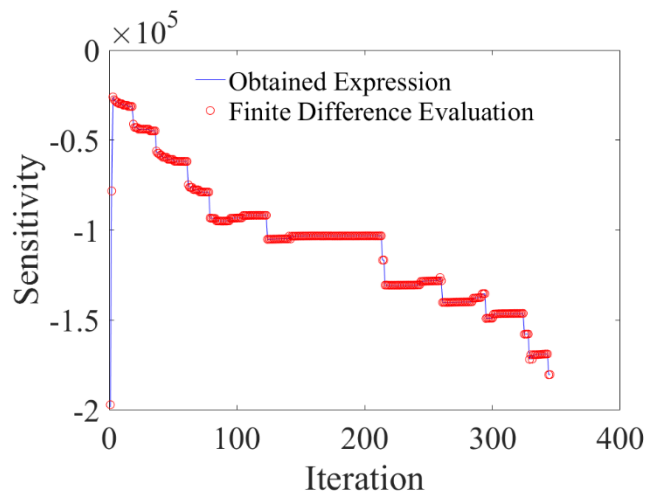
Font: Author (2022).

The proposed optimization problem consists of minimizing the structural compliance, considering elastoplastic material behavior employing an incremental formulation, with a volume constraint of 60% of the total volume, a mesh discretization of 42x21 subvolumes in the horizontal and vertical directions, respectively, and 200 increments. In the absence of filtering techniques, the damping factor is adjusted to 1/2.6 to avoid the oscillatory phenomena. The physical and geometrical parameters are set as: $L = 8$ m (length), $H = 4$ m (height), $P = 81,000$ kN (vertical applied force), $E = 200$ GPa (elastic moduli), $\nu = 0.32$ (Poisson's ratio), $\sigma_{y0} = 250$ MPa (initial yield stress), and $H_p = 20$ GPa (hardening

coefficient). The computational environment, in terms of programming language and machine, can be described as MatLab R2016a (64-bits)/Intel® Core™ i7 CPU 2.93 GHz/16.0 GB RAM/64-bits. Figure 56 shows the penalization effect at the equivalent uniaxial stress-strain diagram for the elastoplastic analysis. The subvolume relative density elevated to the penalization factor multiplies the elastic modulus, the hardening coefficient, and the initial yield stress, as shown in section 2.2.4.

The sensitivity expression for the elastoplastic formulation presented in section 4.4 is verified in Figure 57, employing the finite difference method for the first derivative numerical calculation. The graph shows the sensitivity along the iteration process for the subvolume where the vertical force is applied, which presents the most pronounced plastic strain. As a result, the numerical values for the objective function gradient are like the values obtained by using the expression Eq. (4.52) obtained in section 4.4.

Figure 57 – Sensitivity verification along the optimization process for the elastoplastic approach (No filtering)

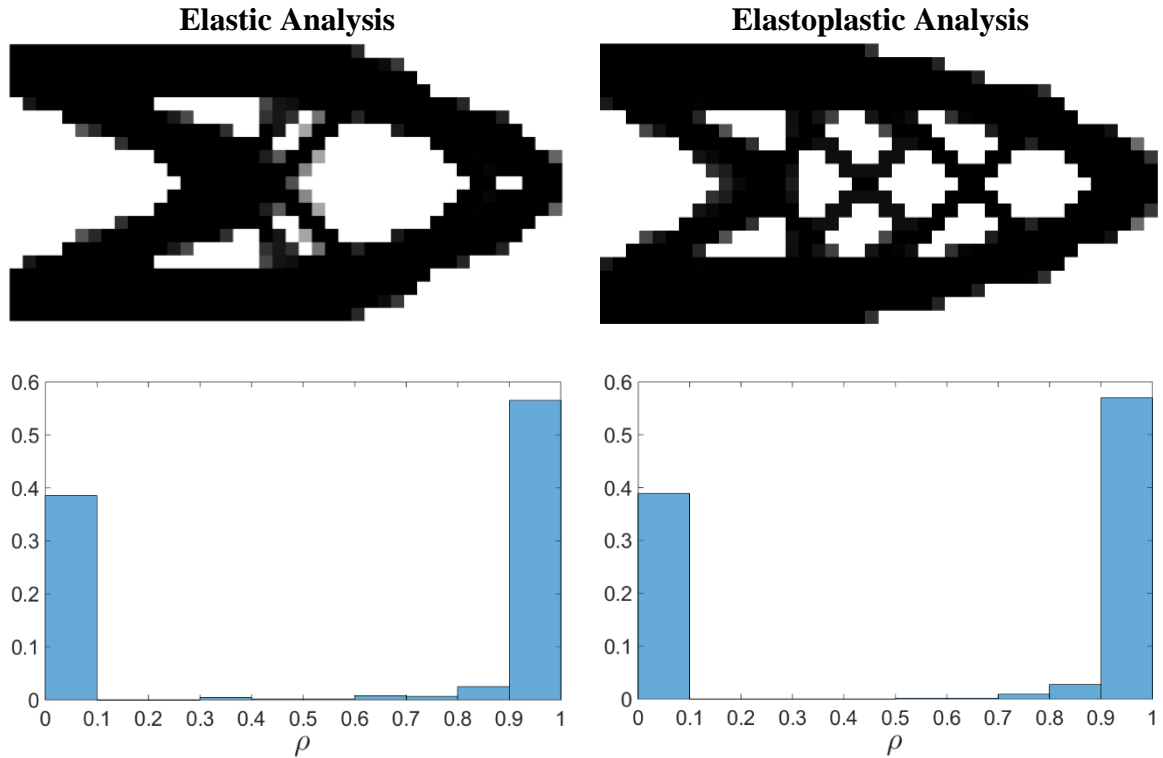


Font: Author (2022).

Figure 58 presents the optimized topologies and the relative density histograms for the elastoplastic approach in comparison with the elastic approach in the absence of filtering techniques, employing the standard finite-volume theory. The optimized topology obtained through the elastic analysis presents more subvolumes with intermediate values for the relative material density in comparison to the optimized topology obtained employing the elastoplastic approach. On the other hand, the optimized topology obtained through the elastoplastic analysis presents more bars. As expected, the obtained optimized topologies are checkerboard-free for both investigated approaches, once the finite-volume theory is free

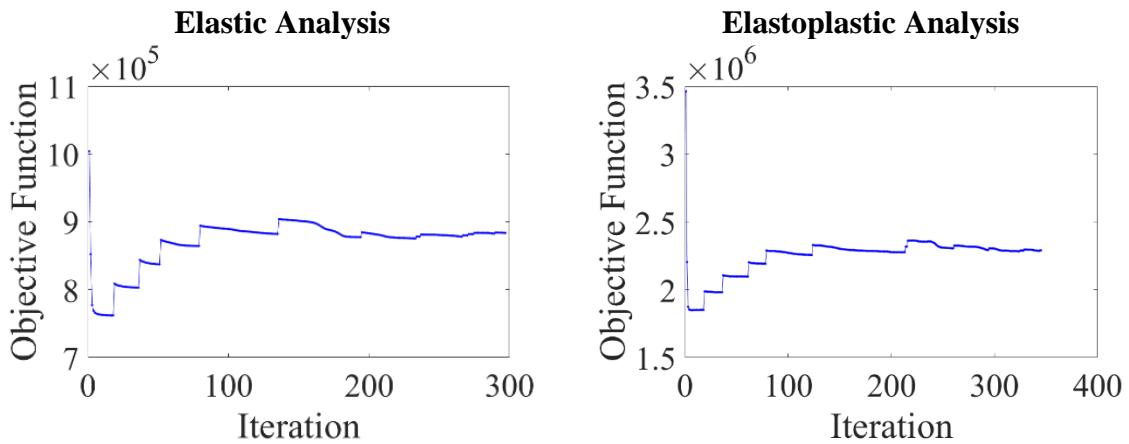
from the checkerboard numerical issue. The objective function evolution of the performed approaches can be seen in Figure 59, which show different stages as the penalty factor changes from 1 to 4, and the elastoplastic approach presents higher values for structural compliance once the applied load is higher in comparison with the elastic approach and it also computes the plastic strain in the strain energy estimation.

Figure 58 – Optimized topologies and relative density histograms (No filtering)



Font: Author (2022).

Figure 59 – Objective function history along the optimization process (No filtering)



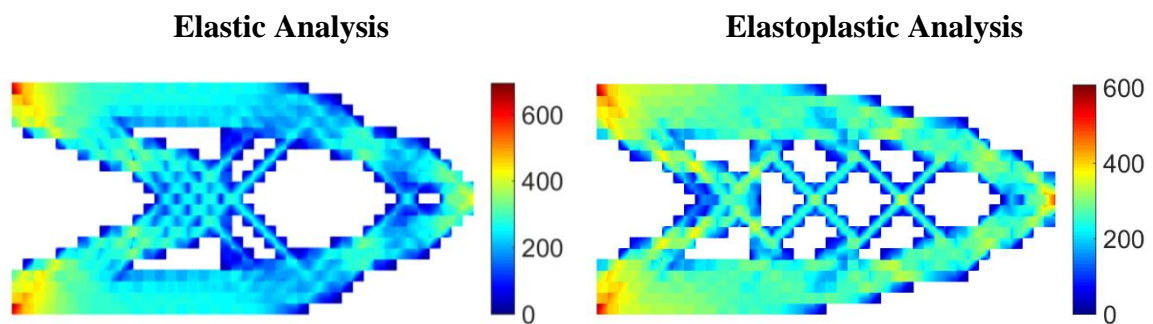
Font: Author (2022).

Table 09 – Performance analysis for the cantilever beam (No filtering)

Analysis	Mesh	NDOF	Number of Iterations	Processing Time	Damping factor
Elastoplastic	42x21	3654	345	7 hr 01 min 12 s	1/2.6
Elastic	42x21	3654	297	1 min 32 s	1/2.6

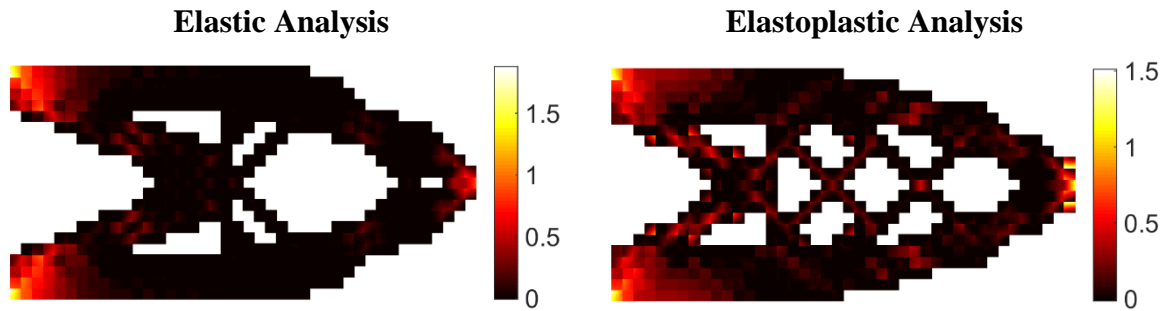
Font: Author (2022).

Table 09 presents the investigated numerical aspects, such as number of iterations and computational cost. The computational cost has highly increased when the elastoplastic approach is employed once an incremental formulation with 200 steps has been employed. The following elastoplastic analysis considered the obtained optimized topologies without a filter technique and the imposition of a prescribed vertical displacement at the free edge of 80 mm. Figure 60 shows the von Mises stress field for the optimized topologies, where it is observed a reduction in stress concentration for the optimized topology obtained from the elastoplastic formulation. Figure 61 presents the effective plastic strain for the optimized topologies, indicating how much the plastic strain has interfered in the optimized topology, especially for the elastoplastic approach. For the generation of these plastic strain and stress fields, it was adopted a *cut-off* of 0.85, where for relative density values lower than 0.85 their subvolumes stresses or strains are printed as white.

Figure 60 – Von Mises stress (MPa) field for the optimized topologies (No filtering)

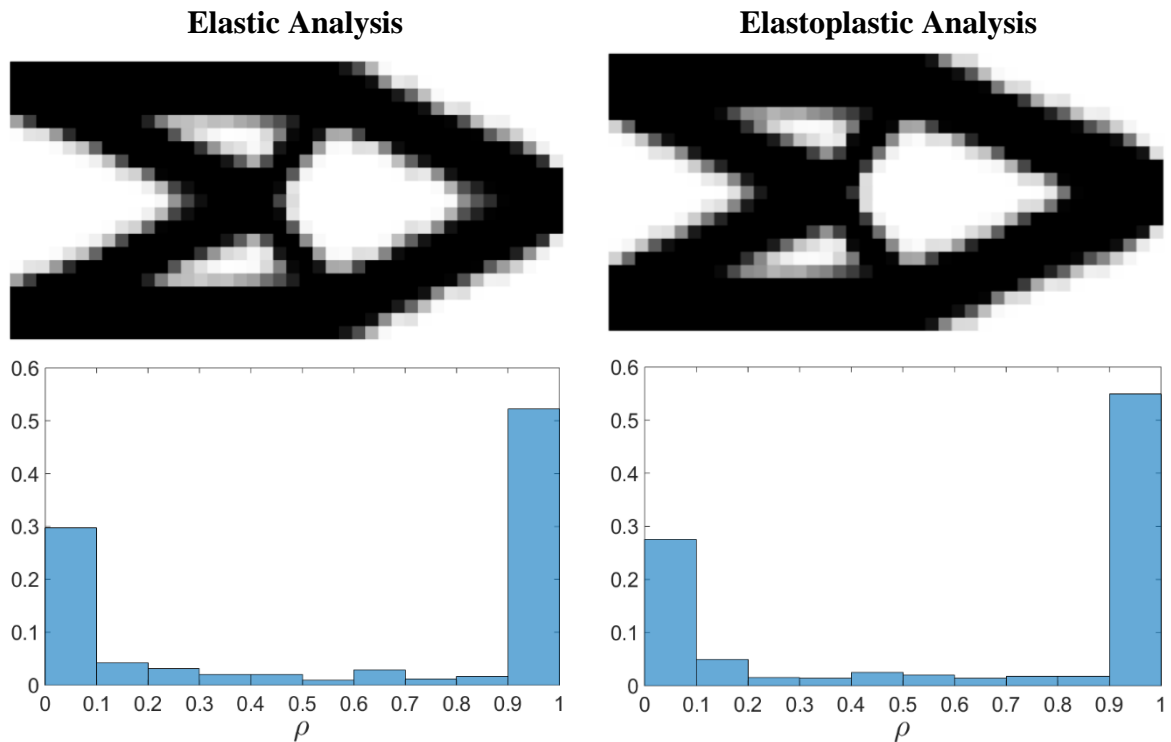
Font: Author (2022).

Figure 61 – Effective plastic strain for the optimized topologies (No filtering)



Font: Author (2022).

Figure 62 – Optimized topologies and relative density histograms (Filtering)

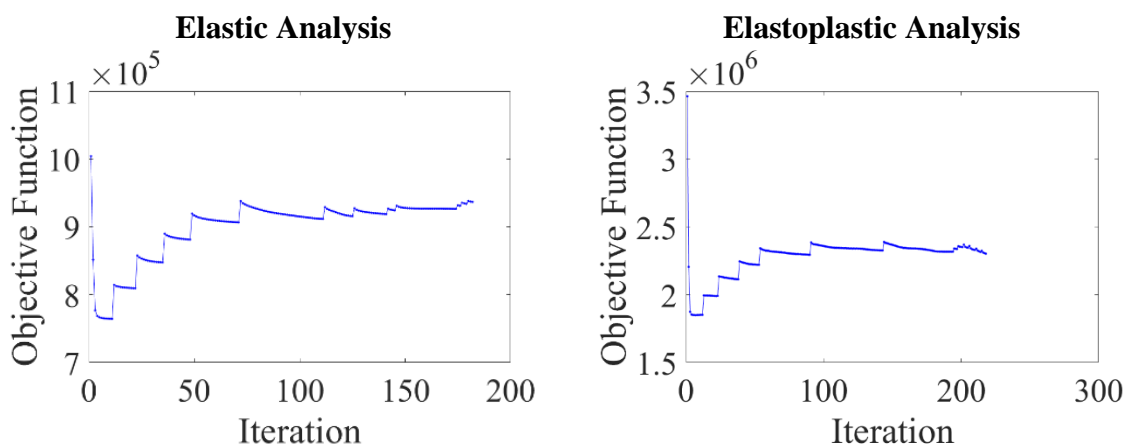


Font: Author (2022).

Similarly, the proposed optimization problem can also be solved by employing a filter that changes the subvolume sensitivity, as previously described. In this case, the damping factor is adjusted to $1/2$, as it provides a faster convergence during the optimization process. Therefore, Figure 62 shows the optimized topologies and the relative density histograms obtained by the approaches employing the mesh-independent filter, presenting similar topologies for the elastoplastic and elastic analyzes. Both optimized topologies present a larger number of subvolumes with intermediate relative density values in comparison with the optimized topologies obtained without a filter technique. Figure 63 shows the objective

function evolution for the elastoplastic and elastic approaches, which also demonstrates the gradual convergence during the optimization process provided by the continued penalization scheme. The difference in the values for the objective function between the elastoplastic and elastic approaches occurs due to the increments of plastic strain in the total strain energy computation.

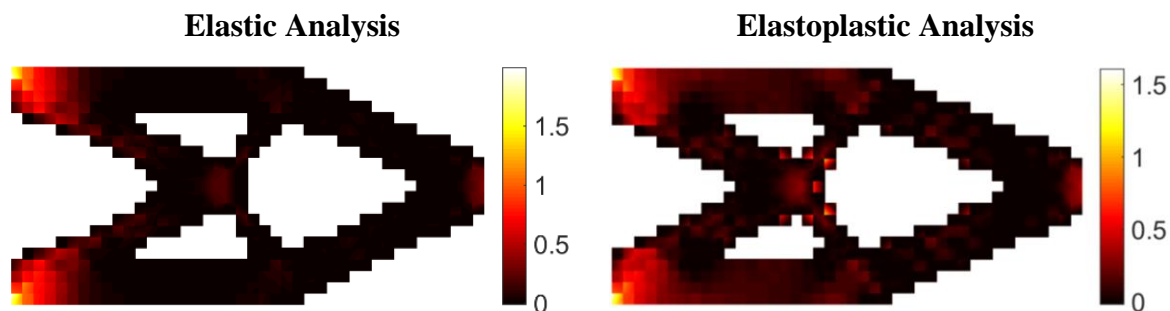
Figure 63 – Objective function history along the optimization process (Filtering)



Font: Author (2022).

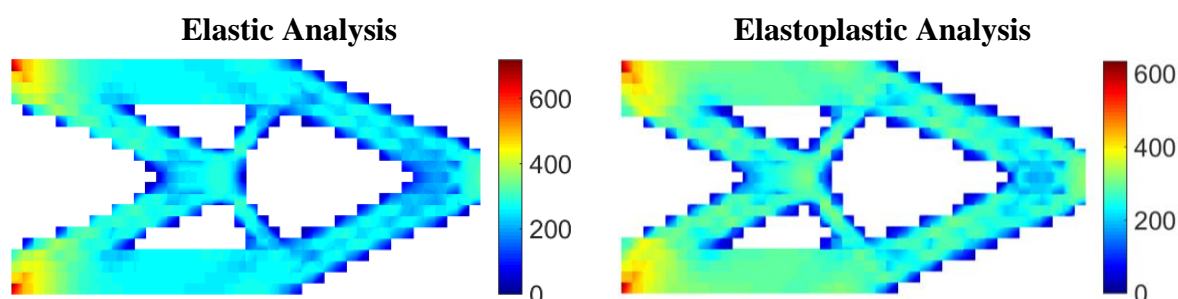
The following elastoplastic analysis considered the obtained optimized topologies employing a filter technique and the imposition of a prescribed vertical displacement at the free edge of 80 mm. Figure 64 shows the effective plastic strain for the optimized topologies, where it is observed a low level of plastic strain for the optimized topology obtained from the elastoplastic approach in comparison to that obtained from the elastic approach. Therefore, it is observed that the plastic strain is concentrated in some subvolumes in the elastic approach, while in the elastoplastic is more spread out in the obtained optimized topology, which is in accordance with the topology optimization objective to reduce the concentration in strain and stress by promoting the depletion of more subvolumes in the optimized structure. Figure 65 shows the von Mises stress fields for the obtained optimized topologies, observing a better stress distribution for the topologies obtained from the approach based on the elastoplastic formulation of the standard finite-volume theory. Additionally, for these graphs it was adopted a cut-off of 0.85 as previously discussed for Figures 60 and 61.

Figure 64 – Effective plastic strain for the optimized topologies (Filtering)



Font: Author (2022).

Figure 65 – Von Mises stress field (MPa) for the optimized topologies (Filtering)



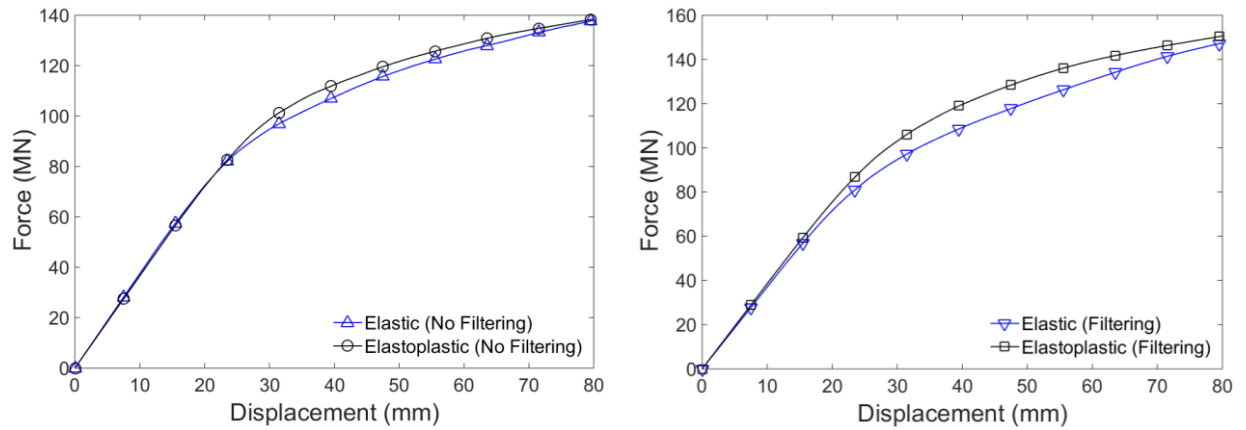
Font: Author (2022).

Table 10 presents the investigated numerical aspects for the cantilever beam example considering the elastoplastic and elastic analyzes and employing a mesh-independent filter. The total number of iterations have not varied so much from one approach to another, while the computational cost has highly increased for the elastoplastic formulation. However, it is observed a reduction in the number of iterations and processing time when the sensitivity filter is employed. For instance, the elastoplastic approach with filter is 1.56 times faster than the same approach in the absence of filtering techniques. This can be partially explained by the number of iterations reduction in the optimization process. Figure 66 presents the force versus displacement curves for the optimized topologies. It can be observed that the optimized topologies obtained from the elastoplastic approaches reduce the displacement for the same applied force. The optimized topologies obtained employing the sensitivity filter technique show a better load capacity due to the larger number of subvolumes with intermediate relative density values compared with the optimized topologies obtained without a filter technique.

Table 10 – Performance analysis for the cantilever beam (Filtering)

Analysis	Mesh	NDOF	Number of Iterations	Processing Time	Damping factor
Elastoplastic	42x21	3654	218	4 h 30 min 25 s	1/2
Elastic	42x21	3654	182	1 min 15 s	1/2

Font: Author (2022).

Figure 66 – Force versus displacement curves for the optimized topologies

Font: Author (2022).

CONCLUSIONS

This work's first contribution is to propose two different methods for structural compliance estimation based on the generalized finite-volume theory. Usually, the compliance function can be defined from the work done by external loading when the finite element method is employed, although the structural compliance can also be evaluated as the strain energy. As the finite element method, the zeroth-order finite-volume theory satisfies the energy balance, i.e., the equality between work done by external loading and total strain energy. However, for the higher-order versions of the generalized finite-volume theory, the work done by external loading tends to give a stiffer response compared to the results given by the total strain energy, based on the analyzed examples in section 5.1. In these cases, the energy balance is observed only when a sufficiently fine mesh is employed. The higher-order versions of the generalized finite-volume theory presented a stiffer response than the zeroth-order version for the analyzed examples.

In the finite-volume theory, the equilibrium of forces is imposed at the subvolume level, which distinguishes it from the finite element method, whose equilibrium of forces is not generally satisfied at the element level. However, the energy balance is not imposed for the finite-volume theory, which does not ensure the equality between work done by external loading and total strain energy, as observed in the finite element method, unless the pointwise differential equilibrium equations are satisfied, as occur in the zeroth-order version of the finite-volume theory.

For the analyzed examples in section 6.1, the simulations with the finite-volume theory have always presented a monotonic energy convergence to the analytical solution. The Q4 element approach has presented the fastest solution in terms of computational cost, followed by the zeroth-order finite-volume theory approaches. At the same time, the second-order finite volume theory and Q8 element approaches have presented the highest processing time, which can be partially explained by the number of degrees of freedom. However, when the processing time of the total strain energy approaches is compared with those obtained by the same approaches based on the work done by external loading, it is not observed any substantial difference.

The formulations proposed in section 4 can be employed in the mechanical energy estimation in solid mechanics, especially for compliance evaluation in structural optimization problems based on the generalized finite-volume theory and elastoplastic formulation of the

standard finite-volume theory. To explore the most different aspects of the finite-volume theory, it is justified the continuation of this investigation by employing the different formulations of the finite-volume theory, especially in the case of heterogeneous materials and structures, where the finite-volume theory has been successfully employed.

The topology optimization for compliance minimization algorithms based on the three versions of the generalized finite-volume theory has shown to be efficient, especially in the absence of filtering technique, where checkerboard-free property is demonstrated. This property has its origins in the satisfaction of continuity conditions in a surface-averaged sense between adjacent subvolumes, which provides interfacial connections among the subvolumes. In the case of the higher-order versions of the finite-volume theory, the evaluation of the compliance function using the strain energy shows to be more efficient than using the work done by external loading by enhancing the employed numerical parameters and minimizing the final compliance function. Although the efficiency of the proposed technique in avoiding the formation of checkerboard regions, this work does not support the substitution of finite-element strategies in topology optimization problems, since several topology optimization techniques based on the finite-element method provide checkerboard-free optimized topologies, such as Poulsen (2002), Jang et al. (2003), Bruggi (2008), Pereira et al. (2010), and Balogh and Lógó (2017). Here, the finite-element method is employed as a source of reference results that can validate the results obtained by the finite-volume theory approaches and allow a comparison analysis of computational performance within the same computational environment.

The continued penalization scheme is adopted during the optimization, guaranteeing a gradual convergence for the overall process. In the absence of filtering techniques, the OC method's damping factor is adjusted to avoid divergence during the optimization process, since a non-maximum number of iterations is established. The damping factor was set up to be as close as possible to the value of $1/2$ and avoid the oscillatory phenomenon during the optimization process. For the approaches that employ the mesh-independency filter, the damping factor was set up as $1/2$, providing a faster convergence.

The sensitivity filter is employed to solve the mesh dependence and length scale problems. In the case of the finite element method, this filtering technique is employed to avoid the formation of checkerboard regions additionally. The employed filter radius is usually applied for checkerboard-free design in finite element-based strategies. Therefore, this filter can solve the checkerboard pattern for the finite-element approaches, while for the

zeroth-order finite-volume theory, this filter could also reduce the observed mesh dependence instability. For the Q8 element, first and second-order finite-volume theories, the optimized topologies employing this filter radius are very similar. In terms of processing time, the approach based on the Q4 element is the fastest, while the approach based on the Q8 element is usually the slowest, with the finite-volume theory exhibiting the intermediates values, with higher processing times for the higher-order versions. The elastoplastic formulation of the standard finite-volume theory is employed to obtain optimized topologies with more realistic physical data. As a result, this approach can provide optimized topologies with a better stress field distribution and a bigger loading capacity.

It is adopted a unique expression to evaluate the filter radius for all analyzes, considering only the neighbor elements/subvolumes (with shared nodes). Different values for the filter radius can affect the obtained topologies, but this investigation can be conducted in future works.

Further Works

Based on the obtained results, the continuation of this investigation is justified by exploring the different aspects that evolve the finite-volume theory, especially in the case of heterogeneous materials with periodic microstructure, where the finite-volume theory has shown to be even more efficient. In addition, these aspects can be explored in problems of interaction between structures and fluids. Although the finite-volume methods encounter large applications in fluid mechanics analyzes, the finite-volume theory has its origin in the higher-order theory for functionally graded materials in solid mechanics analysis. Therefore, excellent compatibility between the finite-volume theory and interaction problems between structures and fluids is expected. This numerical technique carries the basic properties of the finite-volume techniques and was developed for stress analysis in solid structures.

The divulgation of educational codes implemented in MatLab language is suggested for topology optimization of linear elastic structures based on compliance minimization problems to popularize the finite-volume theory in topology optimization problems. This initiative is essential to promote the application of the finite-volume theory in solid mechanics, especially for research beginners, once this numerical technique is easy to follow and can be implemented by undergraduate students of engineering programs. In addition, the divulgation of these MatLab implementations can help disseminate this dissertation's achievements and maximize the impact of the proposed investigations.

Compliance evaluation has played an essential role in topology optimization algorithms in structural analysis. Since the pioneering work of Michell (1904), who derived the optimality criteria (OC) method, and the reconstruction proposed by Bendsøe and Kikuchi (1988), a significant part of the advances in topology optimization has been achieved by employing methodologies based on the structural compliance minimization problems. However, this is not the main objective of most high-performance structural problems. A more realistic option would be to optimize the stress distribution inside the design domain by reducing the local stress concentration in the optimized structure. Thus, stress-based topology optimization is proposed by applying the zeroth-order finite-volume theory to control the local stress concentration in the optimized topologies and avoid the formation of regions with thin bars in those topologies.

Once the energy balance is not satisfied for the higher-order versions of the generalized finite-volume theory for coarse meshes, another suggestion to further work would be to reconstruct these numerical techniques by imposing this energy balance for the first and second-order versions of the generalized finite-volume theory. The equivalence between external work done and total strain energy in a deforming structure for quasi-static analysis can be achieved for these theories by adding unknown coefficients to the displacement field approximation. This reconstruction can also help to obtain more efficient optimized topologies in compliance minimization problems. In addition, 3D and parametric formulations for the generalized version of the finite-volume theory can be developed for elastic stress analyzes in continuum mechanics.

REFERENCES

- ABE, K.; KORO, K. A topology optimization approach using VOF method. *Structural and Multidisciplinary Optimization*, v. 31, n. 6, p. 470-479, 2006.
- ABOUDI, J.; PINDERA, M. J. ARNOLD, S. M. Higher-order theory for functionally graded materials. *Composites Part B: Engineering*, v. 30, n. 8, p. 777-832, 1999.
- ARAUJO, M. V. O. *Teoria de Volumes Finitos Aplicada à Otimização Topológica de Estruturas Elásticas Contínuas*. 2018. 162 p. Thesis (Master in Civil Engineering) – Federal University of Alagoas, Maceió, 2018.
- BAILEY, C.; CROSS, M. A finite volume procedure to solve elastic solid mechanics problems in three dimensions on an unstructured mesh. *International Journal for Numerical Methods in Engineering*, v. 38, n. 10, p. 1757-1776, 1995.
- BALOGH, B.; LÓGÓ, J. The application of drilling degree of freedom to checkerboards in structural optimization. *Advances in Engineering Software*, v. 107, p. 7-12, 2017.
- BANSAL, Y.; PINDERA, M. -J. A second look at the higher-order theory for periodic multiphase materials. *Journal of Applied Mechanics*, v. 72, n. 2, p. 177-195, 2005.
- BANSAL, Y.; PINDERA, M. -J. Efficient Reformulation of the Thermoelastic Higher-Order Theory for Functionally Graded Materials. *Journal of Thermal Stress*, v. 26, n. 11-12, p. 1055-1092, 2003.
- BENDSØE, M. P.; KIKUCHI, N. Generating optimal topologies in structural design using a homogenization method. *Computer Methods in Applied Mechanics and Engineering*, North-Holland, v. 71, p. 197-224, 1988.
- BENDSØE, M. P.; SIGMUND, O. *Topology Optimization: Theory, Methods and Applications*. Berlin: Springer-Verlag, 2003. 393 p.
- BRUGGI, M. On an alternative approach to stress constraints relaxation in topology optimization. *Structural and Multidisciplinary Optimization*, v. 36, p. 125-141, 2008.
- CAVALCANTE, M. A. A. et al. The high-fidelity generalized method of cells with arbitrary cell geometry and its relationship to the parametric finite-volume micromechanics. *International Journal of Solids and Structures*, v. 49, n. 15-16, p. 2037-2050, 2012.
- CAVALCANTE, M. A. A.; MARQUES, S. P.; PINDERA, M. -J. Parametric formulation of the finite-volume theory for functionally graded materials – Part I: Analysis. *Journal of Applied Mechanics*, v. 74, n. 5, p. 946-957, 2007a.
- CAVALCANTE, M. A. A.; MARQUES, S. P.; PINDERA, M. -J. Parametric formulation of the finite-volume theory for functionally graded materials – Part II: numerical results. *Journal of Applied Mechanics*, v. 74, n. 5, p. 946-957, 2007b.
- CAVALCANTE, M. A. A.; MARQUES, S. P.; PINDERA, M. -J. Computational aspects of the parametric finite-volume theory for functionally graded materials. *Computational Materials Science*, v. 44, n. 2, p. 422-438, 2008.

- CAVALCANTE, M. A. A.; PINDERA, M. -J. Generalized finite-volume theory for elastic stress analysis in solid mechanics – Part I: framework. *Journal of Applied Mechanics*, v. 79, n. 5, p. 051006, 2012a.
- CAVALCANTE, M. A. A.; PINDERA, M. -J. Generalized finite-volume theory for elastic stress analysis in solid mechanics – Part I: results. *Journal of Applied Mechanics*, v. 79, n. 5, p. 051007, 2012b.
- CAVALCANTE, M. A. A.; PINDERA, M. -J. Generalized FVDAM theory for periodic materials undergoing finite deformations – Part I: framework. *Journal of Applied Mechanics*, v. 81, n. 2, p. 021005, 2014a.
- CAVALCANTE, M. A. A.; PINDERA, M. -J. Generalized FVDAM theory for periodic materials undergoing finite deformations – Part I: results. *Journal of Applied Mechanics*, v. 81, n. 2, p. 021006, 2014b.
- CARDIFF, P.; DEMIRDŽIĆ, I. Thirty years of the finite volume method for solid mechanics. *Archives of Computational Methods in Engineering*, 2021.
- CHEN, Q.; WANG, G.; CHEN, X. Three-dimensional parametric finite-volume homogenization of periodic materials with multi-scale structural applications. *International Journal of Applied Mechanics*, v. 10, n. 4, p. 1850045, 2018.
- CHRISTENSEN, P. W.; KLARBRING, A. *An Introduction to Structural Optimization*. Linköping: Springer Science & Business Media, 2009. 214 p.
- COLLET, M.; BRUGGI, M.; DUYSINX, P. Topology optimization for minimum weight with compliance and simplified nominal stress constraints for fatigue resistance. *Structural and Multidisciplinary Optimization*, v. 55, n. 3, p. 839-855, 2017.
- DEMIRDŽIĆ, I.; MARTINOVIĆ, D. Finite volume method for thermo-elasto-plastic stress analysis. *Computer Methods in Applied Mechanics and Engineering*, v. 109, n. 3-4, p. 331-349, 1993.
- DEMIRDŽIĆ, I.; MARTINOVIĆ, D.; IVANKOVIĆ, A. Numerical simulation of thermomechanical deformation processes in welded work-piece. *Zavarivanje*, v. 31, p. 209-219, 1988.
- DEMIRDŽIĆ, I.; MUZAFERIJA, S. Finite volume method for stress analysis in complex domains. *International Journal for Numerical Methods in Engineering*, v. 37, n. 21, p. 3751-3766, 1994.
- DÍAZ, A.; SIGMUND, O. Checkerboard patterns in layout optimization. *Structural and Multidisciplinary Optimization*, v. 10, n. 1, p. 40-45, 1995.
- ELELWI, M.; BOTEZ, R. M.; DAO, T. -M. Structural sizing and topology optimization based on weight minimization of a variable tapered span-morphing wing for aerodynamic performance improvements. *Biomimetics*, v. 6, n. 4, p. 55, 2021.
- FERRARI, F.; SIGMUND, O. A new generation 99 line Matlab code for compliance topology optimization and its extension to 3D. *Structural and Multidisciplinary Optimization*, v. 62, n. 4, p. 2211-2228, 2020.

FERRETTI, E. DECM: a discrete element for multiscale modeling of composite materials using the cell method. *Materials*, v. 13, n. 4, p. 880, 2020.

FRYER, Y. D. et al. A control volume procedure for solving the elastic stress-strain equations on an unstructured mesh. *Applied Mathematical Modelling*, v. 15, n. 11-12, p. 639-645, 1991.

FUJII, D.; KIKUCHI, N. Improvement of numerical instabilities in topology optimization using SLP method. *Structural and Multidisciplinary Optimization*, v. 19, n. 2, p. 113-121, 2000.

GATTU, M. et al. Parametric finite-volume micromechanics of uniaxial, continuously-reinforced periodic materials with elastic phases. *Journal of Engineering Materials and Technology*, v. 130, n. 3, p. 031015, 2008.

GUEST, J. K.; PREVOST, J. H.; BELYTSCHKO, T. Achieving minimum length scale in topology optimization using nodal design variables and projection functions. *International Journal for Numerical Methods in Engineering*, v. 61, n. 2, p. 238-254, 2004.

HABER, R. B.; BENDSØE, M. P.; JOG, C. S. A new approach to variable-topology shape design using a constraint on the perimeter. *Structural Optimization*, v. 11, n. 1-2, p. 1-12, 1996.

HAJ-ALI, R.; ABOUDI, J. Discussion paper: Has renaming the high fidelity generalized method of cells been justified? *International Journal of Solids and Structures*, v. 49, n. 15-16, p. 2051-2058, 2012.

HAJ-ALI, R.; ABOUDI, J. Formulation of the high fidelity generalized method of cells with arbitrary cell geometry for refined micromechanics and damage in composites. *International Journal of Solids and Structures*, v. 47, n. 25-26, p. 3447-3461, 2010.

JANG, G. W. et al. Checkerboard-free topology optimization using non-conforming finite elements. *International Journal for Numerical Methods in Engineering*, v. 57, n. 12, p. 1717-1735, 2003.

JOG, C. S.; HABER, R. B.; BENDSØE, M. P. A displacement-based topology design method with self-adaptive layered materials. In: BENDSØE, M. P.; SOARES, C. A. M. *Topology design of structures*. NATO ASI SERIES, vol. 227. Dordrecht: Springer, 1993.

JOG, C. S.; HABER, R. B.; BENDSØE, M. P. Topology design with optimized, self-adaptative materials. *International Journal for Numerical Methods in Engineering*, v. 37, n. 8, p. 1323-1350, 1994.

JOG, C. S.; HABER, R. B. Stability of finite element models for distributed-parameter optimization and topology design. *Computer Methods in Applied Mechanics and Engineering*, v. 130, n. 3-4, p. 203-226, 1996.

JOHNSEN, S. *Structural Topology Optimization: Basic Theory, Methods and Applications*. 2013. 199 p. Thesis (Master of Science in Mechanical Engineering) – Norwegian University of Science and Technology, Trondheim, 2013.

- KHATAM, H.; PINDERA, M. -J. Parametric finite-volume micromechanics of periodic materials with elastoplastic phases. *International Journal of Plasticity*, v. 25, n. 7, p. 1386-1411, 2009.
- KHATAM, H.; PINDERA, M. -J. Plasticity-triggered architectural effects in periodic multilayers with wavy microstructures. *International Journal of Plasticity*, v. 26, n. 2, p. 273-287, 2010.
- KIYONO, C. Y. et al. N. A new multi-p-norm formulation approach for stress-based topology optimization design. *Composite Structures*, v. 156, p. 10-19, 2016.
- LARSSON, R. *Methodology for Topology and Shape Optimization: Application to a Rear Lower Control Arm*. 2016. 53 p. Thesis (Master in Applied Mechanics) – Chalmers University of Technology, Göteborg, 2016.
- LE, C. et al. Stress-based topology optimization for continua. *Structural and Multidisciplinary Optimization*, v. 41, p. 605-620, 2010.
- LI, W.; SURYANARAYANA, P.; PAULINO, G. H. Accelerated fixed-point formulation of topology optimization: application to compliance minimization problems. *Mechanics Research Communications*, v. 103, p. 103469, 2020.
- LONDOÑO, O. G.; PAULINO, G. H. PolyStress: a Matlab implementation for local stress-constrained topology optimization using the augmented Lagrangian method. *Structural and Multidisciplinary Optimization*, v. 63, p. 2065-2097, 2021.
- MATLAB. Version R2016a: MathWorks, 2016.
- MA, Z.-D.; KIKUCHI, N.; HAGIWARA, I. Structural topology and shape optimization for frequency response problem. *Computational Mechanics*, v. 13, n. 3, p. 157-174, 1993.
- MICHELL, A. G. M. The limits of economy of material in frame structures. *The London, Edinburgh, and Dublin Philosophical Magazine and Journal of Science*, v. 8, n. 47, p. 589-597, 1904.
- MONTES, M. A O. *Topology Optimization Algorithms for the Solution of Compliance and Volume Problems in 2D*. 2016. 227 p. Thesis (Master of Computation Science and Industrial Mathematics) – Investigation Center in Mathematics, Guanajuato, 2016.
- PARÍS, J. et al. Topology optimization of continuum structures with local and global stress constraints. *Structural and Multidisciplinary Optimization*, v. 39, p. 419-437, 2009.
- PAULINO, G. H.; LE, C. H. A modified Q4/Q4 element for topology optimization. *Structural and Multidisciplinary Optimization*, v. 37, n. 3, p. 255-264, 2009.
- PEDERSEN, C. G. et al. Topology optimization – Improved checker-board filtering with sharp contours. In: 19th Nordic Seminar on Computational Mechanics, 2006, Lund. *Proceedings...* Lund, Denmark: Lund University, 2006.
- PEREIRA, A. et al. Checkerboard-free topology optimization using polygonal finite elements. *Mecánica Computacional*, v. 29, p. 1525-1534, 2010.

- POMEZANSKI, V.; QUERIN, O. M.; ROZVANY, G. I. N. CO-SIMP: extended SIMP algorithm with direct corner contact control. *Structural and Multidisciplinary Optimization*, v. 30, n. 2, p. 164-168, 2005.
- POULSEN, T. A. A simple scheme to prevent checkerboard patterns and one-node connected hinges in topology optimization. *Structural and Multidisciplinary Optimization*, v. 24, n. 5, p. 396-399, 2002.
- RAHMATALLA, S. F.; SWAN, C. C. A Q4/Q4 continuum structural topology optimization implementation. *Structural and Multidisciplinary Optimization*, v. 27, n. 1-2, p. 130-135, 2004.
- ROUHI, M.; ROHANI, M. R. Topology Optimization of Continuum Structures Using Element Exchange Method. In: Collection of Technical Papers – AIAA/ASME/ASCE/AHS/ASC Structures, Structural Dynamics and Material Conference, 2008.
- ROZVANY, G. I. N. et al. Weight-increasing effect of topology simplification. *Structural and Multidisciplinary Optimization*, v. 25, n. 5-6, p. 459-465, 2003.
- ROZVANY, G. I. N. A Critical Review of Established Methods of Structural Topology Optimization. *Structural and Multidisciplinary Optimization*, v. 37, n. 3, p. 217-237, 2009.
- RUITER, M. J.; KEULEN, F. V. Topology optimization using a topology description function. *Structural and Multidisciplinary Optimization*, v. 26, n. 6, p. 406-416, 2004.
- SHAMES, I. H.; DYM, C. L. *Energy and Finite Element Methods in Structural Mechanics*. New York: Taylor & Francis Books, 1986. 776 p.
- SHOBEIRI, V. Structural topology optimization based on the smoothed finite element method. *Latin American Journal of Solids and Structures*, v. 13, n. 2, p. 378-390, 2016.
- SIGMUND, O. A 99 line topology optimization code written in Matlab. *Structural and Multidisciplinary Optimization*, v. 21, n. 2, p. 120-127, 2001.
- SIGMUND, O. *Design of material structures using topology optimization*. 1994. 104 p. Thesis (Doctorate in Mechanical Engineering) – Technical University of Denmark, Lyngby, 1994.
- SIGMUND, O. Morphology-based black and white filters for topology optimization. *Structural and Multidisciplinary Optimization*, v. 33, n. 4-5, p. 401-424, 2007.
- SIGMUND, O. On the design of compliant mechanisms using topology optimization. *Mechanics of Structures and Mechanics*, v. 25, p. 495-526, 1997.
- SIGMUND, O.; PETERSSON, J. Numerical instabilities in topology optimization: A survey on procedures dealing with checkerboards, mesh-dependencies, and local minima. *Structural Optimization*, Springer-Verlag, v. 16, p. 68-75, 1998.
- SILVA, E. C. N. Técnicas de otimização aplicadas no projeto de peças mecânicas, 2003. Available at: <<https://silo.tips/download/esse-artigo-procura-dar-uma-visao-geral-sobre-as-tecnicas-de-otimizacao->

WANG, S.; WANG, M. Y. Radial basis functions and level set method for structural topology optimization. *International Journal for Numerical Methods in Engineering*, v. 65, n. 12, p. 2060-2090, 2006.

WHEEL, M. A. A finite-volume approach to the stress analysis of pressurized axisymmetric structures. *International Journal of Pressure Vessels and Piping*, v. 68, n. 3, p. 311-317, 1996.

YÜKSEL, O. An overview on topology optimization methods employed in structural engineering. *Kirklareli University Journal of Engineering and Science*, v. 5, n. 2, p. 159-175, 2019.

ZHAO, T. et al. Topology optimization considering the Drucker-Prager criterion with a surrogate nonlinear elastic constitutive model. *Structural and Multidisciplinary Optimization*, v. 62, p. 3205-3227, 2020.

ZHONG, Y.; BANSAL, Y.; PINDER, M. -J. Efficient reformulation of the thermal higher-order theory for FGMs with locally variable conductivity. *International Journal of Computational Science and Engineering*, v. 5, n. 4, p. 795-831, 2004.

APPENDIX A

Auxiliary matrices employed in the Finite-Volume Theory:

$$\mathbf{A}_{(8 \times 8)}^{(q)} = \begin{bmatrix} 0 & -\frac{1}{2}h_q & 0 & \frac{1}{4}h_q^2 & 0 & 0 & 0 & 0 \\ 0 & 0 & 0 & 0 & 0 & -\frac{1}{2}h_q & 0 & \frac{1}{4}h_q^2 \\ \frac{1}{2}l_q & 0 & \frac{1}{4}l_q^2 & 0 & 0 & 0 & 0 & 0 \\ 0 & 0 & 0 & 0 & \frac{1}{2}l_q & 0 & \frac{1}{4}l_q^2 & 0 \\ 0 & \frac{1}{2}h_q & 0 & \frac{1}{4}h_q^2 & 0 & 0 & 0 & 0 \\ 0 & 0 & 0 & 0 & 0 & \frac{1}{2}h_q & 0 & \frac{1}{4}h_q^2 \\ -\frac{1}{2}l_q & 0 & \frac{1}{4}l_q^2 & 0 & 0 & 0 & 0 & 0 \\ 0 & 0 & 0 & 0 & -\frac{1}{2}l_q & 0 & \frac{1}{4}l_q^2 & 0 \end{bmatrix} \quad (\text{A.1})$$

$$\mathbf{a}_{(8 \times 2)}^{(q)} = \begin{bmatrix} 1 & 0 \\ 0 & 1 \\ 1 & 0 \\ 0 & 1 \\ 1 & 0 \\ 0 & 1 \\ 1 & 0 \\ 0 & 1 \end{bmatrix} \quad (\text{A.2})$$

$$\mathbf{B}_{(8 \times 8)}^{(q)} = \begin{bmatrix} \mathbf{N}^{(1)} & \mathbf{0} & \mathbf{0} & \mathbf{0} \\ \mathbf{0} & \mathbf{N}^{(2)} & \mathbf{0} & \mathbf{0} \\ \mathbf{0} & \mathbf{0} & \mathbf{N}^{(3)} & \mathbf{0} \\ \mathbf{0} & \mathbf{0} & \mathbf{0} & \mathbf{N}^{(4)} \end{bmatrix} \begin{bmatrix} \mathbf{C}^{(q)} & \mathbf{0} & \mathbf{0} & \mathbf{0} \\ \mathbf{0} & \mathbf{C}^{(q)} & \mathbf{0} & \mathbf{0} \\ \mathbf{0} & \mathbf{0} & \mathbf{C}^{(q)} & \mathbf{0} \\ \mathbf{0} & \mathbf{0} & \mathbf{0} & \mathbf{C}^{(q)} \end{bmatrix} \begin{bmatrix} \mathbf{E}^{(1)} \\ \mathbf{E}^{(2)} \\ \mathbf{E}^{(3)} \\ \mathbf{E}^{(4)} \end{bmatrix} \quad (\text{A.3})$$

where:

$$\mathbf{N}^{(1)} = \begin{bmatrix} \mathbf{0} & \mathbf{0} & -\mathbf{1} \\ \mathbf{0} & -\mathbf{1} & \mathbf{0} \end{bmatrix}, \mathbf{N}^{(2)} = \begin{bmatrix} \mathbf{1} & \mathbf{0} & \mathbf{0} \\ \mathbf{0} & \mathbf{0} & \mathbf{1} \end{bmatrix}, \mathbf{N}^{(3)} = \begin{bmatrix} \mathbf{0} & \mathbf{0} & \mathbf{1} \\ \mathbf{0} & \mathbf{1} & \mathbf{0} \end{bmatrix}, \mathbf{N}^{(4)} = \begin{bmatrix} -\mathbf{1} & \mathbf{0} & \mathbf{0} \\ \mathbf{0} & \mathbf{0} & -\mathbf{1} \end{bmatrix},$$

$$\mathbf{E}^{(1)} = \begin{bmatrix} 1 & 0 & 0 & 0 & 0 & 0 & 0 & 0 \\ 0 & 0 & 0 & 0 & 0 & 1 & 0 & -\frac{3}{2}h_q \\ 0 & 1 & 0 & -\frac{3}{2}h_q & 1 & 0 & 0 & 0 \end{bmatrix}, \mathbf{E}^{(2)} = \begin{bmatrix} 1 & 0 & \frac{3}{2}l_q & 0 & 0 & 0 & 0 & 0 \\ 0 & 0 & 0 & 0 & 0 & 1 & 0 & 0 \\ 0 & 1 & 0 & 0 & 1 & 0 & \frac{3}{2}l_q & 0 \end{bmatrix},$$

$$\mathbf{E}^{(3)} = \begin{bmatrix} 1 & 0 & 0 & 0 & 0 & 0 & 0 & 0 \\ 0 & 0 & 0 & 0 & 0 & 1 & 0 & \frac{3}{2}h_q \\ 0 & 1 & 0 & \frac{3}{2}h_q & 1 & 0 & 0 & 0 \end{bmatrix}, \mathbf{E}^{(4)} = \begin{bmatrix} 1 & 0 & -\frac{3}{2}l_q & 0 & 0 & 0 & 0 & 0 \\ 0 & 0 & 0 & 0 & 0 & 1 & 0 & 0 \\ 0 & 1 & 0 & 0 & 1 & 0 & -\frac{3}{2}l_q & 0 \end{bmatrix},$$

and $\mathbf{C}^{(q)}$ is the tangent material stiffness matrix of the subvolume q .

APPENDIX B

The matrices $\mathbf{E}_m^{(q)}(x_1^{(q)}, x_2^{(q)})$ can be expressed as:

$$\mathbf{E}_0^{(q)}(x_1^{(q)}, x_2^{(q)}) = \begin{bmatrix} 1 & 0 & 3x_1^{(q)} & 0 & 0 & 0 & 0 & 0 \\ 0 & 0 & 0 & 0 & 0 & 1 & 0 & 3x_2^{(q)} \\ 0 & 1 & 0 & 3x_2^{(q)} & 1 & 0 & 3x_1^{(q)} & 0 \end{bmatrix}, \quad (\text{B.1})$$

$$\mathbf{E}_1^{(q)}(x_1^{(q)}, x_2^{(q)}) = \begin{bmatrix} x_2^{(q)} & 0 & 3x_1^{(q)}x_2^{(q)} & 0 \\ 0 & x_1^{(q)} & 0 & 3x_1^{(q)}x_2^{(q)} \\ x_1^{(q)} & x_2^{(q)} & \frac{3}{4}x_1^{(q)2} - \frac{l^2}{16} & \frac{3}{4}x_2^{(q)2} - \frac{h^2}{16} \end{bmatrix}, \quad (\text{B.2})$$

$$\mathbf{E}_2^{(q)}(x_1^{(q)}, x_2^{(q)}) = \begin{bmatrix} \frac{3}{2}x_2^{(q)2} - \frac{h^2}{8} & 0 & \frac{3}{2}x_1^{(q)}(3x_2^{(q)2} - \frac{h^2}{4}) & 0 \\ 0 & \frac{3}{2}x_1^{(q)2} - \frac{l^2}{8} & 0 & \frac{3}{2}x_2^{(q)}(3x_1^{(q)2} - \frac{l^2}{4}) \\ 3x_1^{(q)}x_2^{(q)} & 3x_1^{(q)}x_2^{(q)} & x_2^{(q)}(\frac{9}{4}x_1^{(q)2} - \frac{3}{16}l^2) & x_1^{(q)}(\frac{9}{4}x_2^{(q)2} - \frac{3}{16}h^2) \end{bmatrix}, \quad (\text{B.3})$$

The non-zero matrices $\mathbf{D}_{mn}^{(q)}$ were found to be as follows:

$$\mathbf{D}_{00}^{(q)} = \begin{bmatrix} C_{11}lh & 0 & 0 & 0 & 0 & C_{12}lh & 0 & 0 \\ 0 & C_{44}lh & 0 & 0 & C_{44}lh & 0 & 0 & 0 \\ 0 & 0 & \frac{3C_{11}l^3h}{4} & 0 & 0 & 0 & 0 & 0 \\ 0 & 0 & 0 & \frac{3C_{44}h^3l}{4} & 0 & 0 & 0 & 0 \\ 0 & C_{44}lh & 0 & 0 & C_{44}lh & 0 & 0 & 0 \\ C_{12}lh & 0 & 0 & 0 & 0 & C_{11}lh & 0 & 0 \\ 0 & 0 & 0 & 0 & 0 & 0 & \frac{3C_{44}h^3l}{4} & 0 \\ 0 & 0 & 0 & 0 & 0 & 0 & 0 & \frac{3C_{44}h^3l}{4} \end{bmatrix}, \quad (\text{B.4})$$

$$\mathbf{D}_{01}^{(q)} = \begin{bmatrix} 0 & 0 & 0 & 0 \\ 0 & 0 & 0 & 0 \\ 0 & \frac{C_{12}l^3h}{4} & 0 & 0 \\ 0 & \frac{C_{44}h^3l}{4} & 0 & 0 \\ 0 & 0 & 0 & 0 \\ 0 & 0 & 0 & 0 \\ \frac{C_{44}l^3h}{4} & 0 & 0 & 0 \\ \frac{C_{12}h^3l}{4} & 0 & 0 & 0 \end{bmatrix}, \quad (\text{B.5})$$

$$\mathbf{D}_{10}^{(q)} = \begin{bmatrix} 0 & 0 & 0 & 0 & 0 & 0 & \frac{C_{44}l^3h}{4} & \frac{C_{12}h^3l}{4} \\ 0 & 0 & \frac{C_{12}l^3h}{4} & \frac{C_{44}h^3l}{4} & 0 & 0 & 0 & 0 \\ 0 & 0 & 0 & 0 & 0 & 0 & 0 & 0 \\ 0 & 0 & 0 & 0 & 0 & 0 & 0 & 0 \end{bmatrix}, \quad (\text{B.6})$$

$$\mathbf{D}_{11}^{(q)} = \begin{bmatrix} \frac{C_{11}h^3l+C_{44}l^3h}{12} & 0 & 0 & 0 \\ 0 & \frac{C_{11}l^3h+C_{44}h^3l}{12} & 0 & 0 \\ 0 & 0 & \frac{C_{44}l^5h+5C_{11}l^3h^3}{80} & \frac{C_{12}h^3l^3}{16} \\ 0 & 0 & \frac{C_{12}h^3l^3}{16} & \frac{C_{44}lh^5+5C_{11}l^3h^3}{80} \end{bmatrix}, \quad (\text{B.7})$$

$$\mathbf{D}_{22}^{(q)} = \begin{bmatrix} \frac{C_{11}lh^5+5C_{44}l^3h^3}{80} & \frac{C_{44}h^3l^3}{16} & 0 & 0 \\ \frac{C_{44}h^3l^3}{16} & \frac{C_{11}l^5h+5C_{44}h^3l^3}{80} & 0 & 0 \\ 0 & 0 & \frac{6C_{11}l^3h^5+11C_{44}l^5h^3}{640} & 0 \\ 0 & 0 & 0 & \frac{3C_{44}l^3h^5+3C_{11}h^3l^5}{320} \end{bmatrix}, \quad (\text{B.8})$$

where C_{ij} are the elements of the stiffness tensor, considering the plane stress state.